Synchrotron-based characterization of mechanobiological effects on the nanoscale in musculoskeletal tissues

Silva Barreto, Isabella

2023

Document Version:
Publisher's PDF, also known as Version of record

Synchrotron-based characterization of mechanobiological effects on the nanoscale in musculoskeletal tissues

Isabella Silva Barreto

LUND
UNIVERSITY

DOCTORAL DISSERTATION

by due permission of the Faculty of Engineering, Lund University, Sweden.
To be defended in lecture hall *E:1406, E-building, Ole Römers väg 3, Lund, Sweden*

Friday October 20th, 2023 at 9.00

Faculty opponent
Professor Himadri Gupta

Queen Mary University of London

Cover artwork by Isabella Silva Barreto, depicting the collagen fibril distribution within the longitudinal plane of a healing tendon.

Department of Biomedical Engineering
Lund University
P.O. Box 118, SE-221 00 Lund
Sweden

ISBN: 978-91-8039-813-8 (print)

ISBN: 978-91-8039-814-5 (pdf)

ISRN-nr: LUTEDX/TEEM-1136-SE

Report No. 4/23

Printed in September 2023 by Tryckeriet i E-huset, Lund, Sweden

Public defence

October 20th, 2023, 9.00 in E:1406

E-building, Lund University, Ole Römers väg 3, 223 63, Lund, Sweden

Supervisors

Prof. Hanna Isaksson

Department of Biomedical Engineering, Lund University, Lund, Sweden

Assistant Prof. Marianne Liebi

Institute of Materials, Ecolé Polytechnique fédérale de Lausanne, Lausanne, Switzerland & Photon Science Division, Paul Scherrer Institute, Villigen, Switzerland

Associate Prof. Pernilla Eliasson

Department of Orthopaedics, Sahlgrenska University Hospital, Gothenburg, Sweden

Faculty opponent

Prof. Himadri Gupta

School of Engineering and Materials Science, Centre for Bioengineering, Queen Mary University of London, London, UK

Board of examination

Prof. Cecilia Persson

Department of Materials Science & Engineering, Uppsala University, Sweden

Prof. Toni Arndt

Department of Physiology, Nutrition & Biomechanics, Swedish School of Sport and Health Sciences, Sweden

Associate Prof. Oxana Klementieva

Department of Experimental Medical Science, Lund University, Sweden

Deputy member: Associate Prof. Cedric Dicko

Department of Chemistry, Lund University, Sweden

Organization LUND UNIVERSITY Department of Biomedical Engineering Box 118, 211 00 Lund, Sweden Author: Isabella Silva Barreto	**Document name** DOCTORAL DISSERTATION **Date of issue** October 20th, 2023 Sponsoring organization

Title: Synchrotron-based characterization of mechanobiological effects on the nanoscale in musculoskeletal tissues

Abstract

Collagen is the main organic building block of musculoskeletal tissues. Despite collagen being their smallest load bearing unit, these tissues differ significantly in mechanical function and properties. A major factor behind these differences is their hierarchical organization, from the collagen molecule up to the organ scale. It is thus of high importance to understand the characteristics of each level, as well as how they interact and relate to each other. With such knowledge, improved prevention and rehabilitation of musculoskeletal pathologies may be achieved.

Both mineralized and soft collagenous tissues respond to their mechanical loading environment according to specific mechanobiological principles. During prenatal development, immobilization can cause dramatic effects on the developing skeleton, causing the newly formed bones to be smaller, deformed and more prone to fracture. But how immobilization affects the deposition, structure and composition of the developing bones is still unclear. In tendons, both insufficient and excessive mechanical loading increases the risk of injury. After rupture, reduced mechanical loading results in altered collagen structure and cell activity, thus influencing the mechanical properties of the healing tendon. How the loading environment affects the structure of intact and ruptured tendons is still debated.

The work presented in this thesis aims to thoroughly characterize the mechanobiological effects on the mineralization process in developing bones as well as the collagen structure and multiscale mechanical response of intact and healing tendons. This is achieved through a multimodal approach including a range of high-resolution synchrotron- and lab-based techniques, in combination with mechanical testing.

In the first part of the thesis, humeri from "muscle-less" embryonic mice and their healthy littermates at development stages from start of mineralization to shortly before birth were investigated. The multimodal approach revealed a highly localized spatial pattern of Zinc during normal development to sites of ongoing mineralization, accompanied by larger mineral particles. Healthy bones also showed signs of remodeling at later time points. In the absence of skeletal muscle, it was revealed that the developing bones exhibited a delayed but increased mineral deposition and growth, with no signs of remodeling.

In the second part of the thesis, intact Achilles tendons from rats subjected to either full *in vivo* loading through free cage activity or unloading by Botox injections combined with cast immobilization were investigated. It was shown that the nanoscale fibrils in the Achilles tendon respond to the applied tissue loads and exhibit viscoelastic responses. It was revealed that *in vivo* unloading results in a more disorganized microstructure and an impaired viscoelastic response. Unloading also altered the nanoscale fibril mechanical response, possibly through alterations in the strain partitioning between hierarchical levels.

In the third part of the thesis, Achilles tendons were transected and allowed to heal while subjected to either full *in vivo* loading, reduced loading through Botox injections or unloading. *In vivo* unloading during the early healing process resulted in a delayed and more disorganized collagen structure and a larger presence of adipose tissue. Unloading also delayed the remodeling of the stumps as well as callus maturation. Additionally, the nanoscale fibril mechanical response was altered, with unloaded tendons exhibiting a low degree of fibril recruitment as well as a decreased ability for fibril extension.

The work in this thesis further illustrates the important role of the mechanical environment on the nanostructure of musculoskeletal tissues. It also highlights the power of combining high-resolution tissue characterization techniques into a multimodal and multiscale approach, allowing us to study the effects on several hierarchical length scales simultaneously and as a result be able to elucidate the intricate connection between hierarchical scales.

Key words: nanoscale, microscale, mechanical properties, synchrotron, x-ray imaging, collagen, hydroxyapatite

Classification system and/or index terms (if any)

Supplementary bibliographical information ISRN: LUTEDX/TEEM-1136-SE Report No.: 4/23	**Language:** English ISBN: 978-91-8039-813-8 (print) ISBN: 978-91-8039-814-5 (pdf)

Recipient's notes	**Number of pages 255**	Price
	Security classification	

Signature: 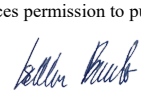 Date: 2023-09-21

Populärvetenskaplig sammanfattning

Rörelseorganens vävnader påverkas och anpassas över tid av den belastning och miljö de utsätts för. Detta kallas mekanobiologi. Vävnader som inte utsätts för belastning får sämre egenskaper. Studier på musembryon visar att ben som inte belastas normalt får en annorlunda form och sämre mekaniska egenskaper. Det är fortfarande oklart hur belastning under denna utvecklingsprocess påverkar skelettets sammansättning och byggstenarnas struktur. Studier på hälsenor har visat att både för låg och hög belastning ökar risken för skada. Trots att det finns många olika rehabiliteringsprotokoll som kan tillämpas efter en hälseneruptur är det fortfarande oklart vad som ger bäst resultat och minskar risken för ytterligare skada. En bidragande faktor till detta är att vi saknar en djupare kunskap kring hur belastning påverkar strukturen hos både intakta och läkande hälsenor.

Den minsta byggstenen i rörelseorganens vävnader, så som skelettet och senor, är proteinet kollagen. Trots att de olika vävnaderna alla är uppbyggda av kollagen så skiljer sig deras mekaniska funktion och egenskaper avsevärt; senor är elastiska och har energibevarande samt dämpande egenskaper, medan skelettet är hårt, styvt och kan utstå hög belastning. Skelettets styvhet kommer från dess oorganiska mineralfas, hydroxyapatit, som är inbäddat i kollagennätverket. Övriga skillnader i funktion mellan rörelseorganens vävnader beror på hur kollagenet är organiserat över flera längdskalor. Deras hierarkiska organisation tillåter optimering på flertalet längdskalor, vilket medför att vävnaden kan anpassa sig till sin mekaniska miljö. Det är därför viktigt att förstå organisationen på varje strukturell nivå, samt hur olika nivåer samspelar. Ökad kunskap kring detta kan bidra till bättre förebyggande insatser och rehabilitering av rörelseorganens olika skador och sjukdomar. Målet med den här avhandlingen var att undersöka hur mekanisk belastning påverkar mineraliseringsprocessen i ben under embryonal utveckling,

samt på kollagenets organisation och funktion hos intakta och läkande hälsenor. För att uppnå detta undersöktes vävnader med en kombination av olika synkrotronbaserade röntgentekniker så som låg- och vidvinkelspridning, spektroskopi och tomografi, samt dragprov. En synkrotron är en partikelaccelerator som kan producera mycket kraftfullare röntgenstrålning än labbkällor, vilket möjliggör mer detaljerade undersökningar.

I den första delen av avhandlingen studerades mineraliseringsprocessen i ben från musembryon med och utan normal muskelbildning. Röntgentekniker tillämpades för att avbilda mineralfasen i ben, så som dess sammansättning och mineralplattornas storlek och riktning. Vid normal utveckling mineraliseras musbenen på enbart 4 dagar och uppnår liknande sammansättning och koncentration av calcium som vuxna ben. Det visade sig även att zink är en viktig faktor för mineraliseringsprocessen, då det återfinns i områden där mineralisering pågår. När muskler däremot saknas så blir processen försenad och oorganiserad. Det visar sig bland annat genom en mer utbredd förekomst av zink samt en kontinuerlig ökning i storlek av mineralplattorna. Detta skulle kunna förklara varför muskellösa ben mot slutet av utvecklingen kommer i kapp storleksmässigt.

I den andra delen av avhandlingen studerades hälsenor från råttor som kunde röra sig normalt samt de som inte kunde belasta sina senor. Röntgentekniker i kombination med dragprov tillämpades för att avbilda kollagenstrukturen och dess mekaniska egenskaper. Resultaten visade att kollagenfibrillerna på nanoskalan reagerar på belastning samtidigt som senan, samt att senans dämpande egenskaper återfinns hela vägen ner på nanoskalan. Avlastning av senan ledde till en mindre välorganiserad mikrostruktur samt förändrade mekaniska egenskaper som sträckte sig hela vägen från organnivå ner till fibrillerna på nanoskalan.

I den tredje delen av avhandlingen studerades läkande hälsenor från råttor som kunde röra sig normalt samt de som inte kunde belasta sina senor. Röntgentekniker i kombination med dragprov tillämpades för att avbilda den nybildade kollagenstrukturen och dess mekaniska egenskaper. 3D avbildning visade att avlastning under läkningsprocessen leder till en försenad och mindre organiserad återbildning av kollagennätverket. Minskad belastning ledde också till en större andel fettvävnad, en försenad omorganisering av den tidigare senan, samt en försenad mognad av den läkande vävnaden. Detta skulle kunna förklara den ökade risken för ytterligare skada vid minskad belastning under läkningsprocessen.

Sammanfattningsvis visar resultaten i avhandlingen vikten av den mekaniska miljön för nanostrukturen hos rörelseorganens vävnader. Den visar även på hur flertalet synkrotronbaserade röntgentekniker kan kombineras för att undersöka vävnadens sammansättning, struktur och mekaniska funktion för att studera flera strukturella nivåer samtidigt, vilket i sin tur möjliggör bättre förståelse av hur den komplexa uppbyggnaden ger vävnaderna deras unika funktion.

Abstract

Collagen is the main organic building block of musculoskeletal tissues. Despite collagen being their smallest load bearing unit, these tissues differ significantly in mechanical function and properties. A major factor behind these differences is their hierarchical organization, from the collagen molecule up to the organ scale. It is thus of high importance to understand the characteristics of each level, as well as how they interact and relate to each other. With such knowledge, improved prevention and rehabilitation of musculoskeletal pathologies may be achieved.

Both mineralized and soft collagenous tissues respond to their mechanical loading environment according to specific mechanobiological principles. During prenatal development, immobilization can cause dramatic effects on the developing skeleton, causing the newly formed bones to be smaller, deformed and more prone to fracture. But how immobilization affects the structure and composition of the developing bones is still unclear. In tendons, both insufficient and excessive mechanical loading increases the risk of injury. After rupture, reduced mechanical loading results in altered collagen structure and cell activity, influencing the mechanical properties of the healing tendon. How the loading environment affects the structure of intact and ruptured tendons is still debated, and there is currently no consensus on optimal rehabilitation protocols.

The work presented in this thesis aims to thoroughly characterize the mechanobiological effects on the mineralization process in developing bones as well as the collagen structure and multiscale mechanical response of intact and healing tendons. This is achieved through a multimodal approach including a range of high-resolution synchrotron- and lab-based techniques, in combination with mechanical testing.

In the first part of the thesis, humeri from "muscle-less" embryonic mice and their healthy littermates at development stages from start of mineralization to shortly before birth were investigated. The multimodal approach revealed a highly localized spatial pattern of Zinc during normal development to sites of ongoing mineralization, accompanied by larger mineral particles. Healthy bones also showed signs of remodeling at later time points, where both Iron and Zinc were found to precede Calcium. In the absence of muscle-induced loading, it was revealed that the developing bones exhibited a delayed but increased mineral deposition and growth, with no signs of remodeling. This was observed as a more widespread distribution of Zinc at later time points, accompanied by a more rapid increase in Calcium content as well as growth of mineral platelets.

In the second part of the thesis, intact Achilles tendons from rats subjected to either full *in vivo* loading through free cage activity or unloading by Botox injections combined with cast immobilization were investigated. It was shown that the nanoscale fibrils in the Achilles tendon respond to the applied tissue loads. The fibrils also showed viscoelastic responses such as strain relaxation and an increased stretchability and recovery with increasing number of load cycles. Tissue level findings revealed that reduced *in vivo* loading results in a more disorganized microstructure and an impaired viscoelastic response. Unloading also altered the nanoscale fibril mechanical response, possibly through alterations in the strain partitioning between hierarchical levels.

In the third part of the thesis, Achilles tendons were transected and allowed to heal while subjected to either full *in vivo* loading, reduced loading through Botox injections or unloading. *In vivo* unloading during the early healing process resulted in a delayed and more disorganized collagen structure and a larger presence of adipose tissue. Unloading also delayed the remodeling of the stumps as well as callus maturation, postponing the merge between callus tissue and stumps. Additionally, the nanoscale fibril mechanical response was altered, with unloaded tendons exhibiting a low degree of fibril recruitment as well as a decreased ability for fibril extension.

In conclusion, the work in this thesis further illustrates the important role of the mechanical environment on the nanostructure of musculoskeletal tissues. It also highlights the power of combining high-resolution tissue characterization techniques into a multimodal and multiscale approach, allowing us to study the effects on several hierarchical length scales simultaneously and as a result be able to elucidate the intricate connection and relationship between hierarchical scales.

List of appended papers

This thesis consists of a review of the author's work in the field of biomedical engineering. The following selection of the author's publications is referred to in the text by their Roman numerals. Papers I-VI are appended at the end of the thesis and have been reproduced with the permission of the copyright holders.

I. **I. Silva Barreto,** S. Le Cann, S. Ahmed, V. Sotiriou, M.J. Turunen, U. Johansson, A. Rodriguez-Fernandez, T.A. Grünewald, N.C. Nowlan, H. Isaksson, Multi-scale characterization of embryonic long bone mineralization in mice. *Advanced Science*, 2020, 7:21:2002524

The author of this thesis was responsible for preparing specimens, carrying out experiments, conducting data analysis and interpretation for all experiments except for microcomputed tomography. The author of this thesis was responsible for writing the manuscript. The study was designed by the supervisors. All animal experiments were performed by other co-authors.

II. **I. Silva Barreto,** M. Liebi, S. Le Cann, S. Ahmed, T.A. Grünewald, H. Dejea, V. Lutz-Bueno, N.C. Nowlan, H. Isaksson, Lack of embryonic skeletal muscle in mice leads to abnormal mineral deposition and growth. *Manuscript under preparation (to be submitted October 2023)*

The author of this thesis was responsible for preparing samples and carrying out experiments for all except SAXS tensor tomography. The author of this thesis was responsible for data analysis and interpretation of data from all experiments, and for writing the

manuscript. The study was designed by the supervisors. All animal experiments were performed by other co-authors.

III. **I. Silva Barreto,** M. Pierantoni, M. Hammerman, E. Törnquist, S. Le Cann, A. Diaz, J. Engqvist, M. Liebi, P. Eliasson, H. Isaksson, Nanoscale characterization of collagen structural response to *in situ* loading in the rat Achilles tendon. *Matrix Biology*, 2022, 115:32-47

The author of this thesis was involved in the study design together with supervisors. The author of this thesis was responsible for preparing specimens, conducting experiments, data analysis and interpretation. The author of this thesis was responsible for writing the manuscript. All animal experiments were performed by other co-authors.

IV. M. Pierantoni * & **I. Silva Barreto** *, M. Hammerman, V. Novak, A. Diaz, J. Engqvist, P. Eliasson, H. Isaksson, Multimodal and multiscale characterization reveals how tendon structure and mechanical response are altered by reduced loading. * *Joint first authors. Acta Biomaterialia,* 2023, 168:264-276

The author of this thesis was involved in the study design together with supervisors and M. Pierantoni. The study was composed of five main parts; 1) animal experiments, 2) microcomputed tomography, 3) SAXS in combination with *in situ* mechanical testing, 4) *ex situ* mechanical testing and 5) histology. The author of this thesis was responsible for SAXS and mechanical experiments including preparing samples, conducting experiments as well as data analysis and interpretation. M. Pierantoni was responsible for the microcomputed tomography experiment, including preparing samples, conducting experiments as well as data analysis and interpretation. The author of this thesis assisted during microcomputed tomography experiments. M. Pierantoni was responsible for writing the manuscript. All animal experiments and histology were performed by other co-authors.

V. **I. Silva Barreto** * & M. Pierantoni *, L. Nielsen, M. Hammerman, A. Diaz, V. Novak, P. Eliasson, M. Liebi, H. Isaksson, Micro- and nanostructure specific X-ray tomography reveals less matrix formation and altered collagen organization following reduced loading during tendon healing. * *Joint first authors. Under review*

The author of this thesis was largely responsible for the design of this study. The author of this thesis was responsible for preparing the specimens, conducting SASTT and SAXS experiments, data analysis and interpretation. The author of this thesis was responsible for writing the manuscript. M. Pierantoni was responsible for the microcomputed tomography experiments, data analysis and interpretation. All animal experiments were performed by other co-authors.

VI. I. Silva Barreto, K. Sharma, M. Hammerman, A. Diaz, P. Eliasson, H. Isaksson, *In situ* characterization reveals an impaired fibril response to loading following unloading during early Achilles tendon healing, *Data analysis ongoing, preliminary draft (to be submitted fall 2023)*

The author of this thesis was largely responsible for the study design together with supervisors. The author of this thesis was responsible for preparing specimens, conducting experiments, data analysis and interpretation. All animal experiments were performed by other co-authors. The author of this thesis was responsible for writing the manuscript.

Acknowledgements

Feels like it was only yesterday I started, without a clue of how I would manage something as big and scary as this. But here we are, four and a half years later, with this heavy book in front of me. And oh, what a ride it has been! Throughout this immense experience, I have had the privilege and pleasure to meet so many wonderful people along the way.

First of all, I would like to thank my main supervisor, Hanna Isaksson. You have inspired me with your passion, drive and standards for high-quality research. I am eternally grateful for all your time spent helping and guiding me throughout this time, as well as your patience, trust and encouragement. You were always there when I needed it, while still providing me space to grow and develop as an independent researcher. I would also like to thank my co-supervisor, Marianne Liebi. For your support and patience, for sharing your knowledge and teaching me the ways of SASTT. You have always provided different perspectives and valuable insights, and for that I am very grateful. I would also like to thank you for creating such a welcoming environment both at and outside of work, I truly enjoyed it. I would also like to thank my co-supervisor Pernilla Eliasson. Your knowledge and different angle to our projects has been invaluable for bringing this work forward, and I really appreciate the depth it provided to the work of this thesis.

I want to thank my opponent, Prof. Himadri Gupta, and the members of the examination committee, Prof. Cecilia Persson, Prof. Toni Arndt, Associate Prof. Oxana Klementieva and Associate Prof. Cedric Dicko for carefully reading and critically assessing my thesis to ensure the quality of my work.

To all my current and former colleagues of the Lund Biomechanics group – thank you for making these years fun, inspiring and crazy! I am truly lucky to have worked and spent time together with all of you. Elin, Thomas and Joeri, thank you for making my first years in this group completely amazing. For all the fun

AWs, evenings at Bishops, bbqs and board game nights. You finished two years ago, but I still miss you both in and outside of the office. Maria, thank you for always being there for me, for all our crazy beamtimes, for your amazing company and all of our fun times, talks, laughs, dinners, beers, concerts, piercings, (the list goes on!) spent together. You have been my rock throughout this time and truly made this time wonderful. I cannot thank you enough and I will miss you. Kunal, Hector and Gustavo, thank you for all the serious talks, laughs and completely outrageous times. There will be more, I'm sure. Not to mention the sauna-Fridays! Anna, Lorenzo and Tobias, thank you for all the good times both at and outside of work, for interesting talks and fun fikas. Rebecca and Viktor, thank you for all the fika, putting up with my craziness, and of course for all our drag queen bingos together! I would also like to thank Hannicka for still sticking around after all these years and putting up with my weird sh*t (*But why choose?*).

To my other colleagues at BMC and E-house, thank you for the AWs, dinners and innebandy. To my friends and collaborators at Chalmers, Adrian, Leonard, Linnea and Martina, thank you for welcoming me into your fold and for making my stays at Chalmers fun and rewarding. To my friends at PSI, Irene, Christian and Arthur, thank you for all the talks, goofiness and wonderful times spent together climbing, hiking and dancing. I had a great time at PSI and I am very happy that I got to know all of you. And we will soon meet again for sure!

Thank you to all my collaborators who have helped me throughout this PhD. Ana Diaz, Deepak Raina, Mikael Turunen, Sophie Le Cann, Malin Hammerman, Jonas Engqvist, Niamh C. Nowlan, Leonard Nielsen, Ulf Johansson, Tilman A. Grünewald, Saima Ahmed, Vivien Sotiriou, Vladimir Novak, Angel Rodriguez-Fernandez, Michiel Op de Beeck. Without you, this thesis would be empty.

To Korpen Ishockey and Folkets puck, thank you for helping me learn ice hockey and for all the happy company both inside and outside of the rink. The time on the ice allowed me to recharge, let loose and have insanely fun, which was a life saver during the final sprint of the PhD. Tack till Sebbe, för svordomarna på isen, den knasiga energin och sällskapet som gav mig den extra energin som behövdes.

To Ami. Du är min klippa genom allt. Tack för att du är den bästa vän jag någonsin kunde tänkas ha. Din kärlek, stöd, uppmuntran, vishet och perspektiv har varit ovärderliga för mig och min utveckling som person. Utan dig hade inget av det här varit möjligt.

To my family. Farsan och Mamma, tack för att ni alltid funnits där, trott på mig och stöttat mig. Farsan, jag är oerhört stolt och tacksam över att få möjligheten att visa upp det här för dig. Viktor, tack för alla intressanta diskussioner och för att du alltid utmanar mig. Lucas och Filip, tack för att ni stått ut med storasyrrans knasigheter alla dessa år. Simba och Alice, för er ovillkorliga kärlek och sällskap.

List of abbreviations

1D	one-dimensional
2D	two-dimensional
3D	three-dimensional
ANOVA	analysis of variance
ALP	alkaline phosphatase
Botox	Botulinum toxin
Ca	calcium
CI	confidence interval
CT	computed tomography
ECM	extracellular matrix
ESRF	European Synchrotron Radiation Facility
DLS	Diamond Light Source
Fe	iron
FL	full loading
FOV	field of view
FWHM	full width at half-maximum
FTIR	Fourier transform infrared
HA	hydroxyapatite

IR	infrared
LG	lateral gastrocnemius
MG	medial gastrocnemius
MAX IV	MAX IV laboratory
MMP	matrixmetalloprotease
MRI	magnetic resonance imaging
µCT	microcomputed tomography
µm	micrometre (10^{-6} m)
nm	nanometre (10^{-9} m)
P	phosphate
PBS	phosphate-buffered saline
PC- µCT	phase contrast microcomputed tomography
PLM	polarized light microscopy
RL	reduced loading
SAXS	small-angle X-ray scattering
SASTT	small-angle X-ray scattering tensor tomography
Scx	Scleraxis
SD	standard deviation
SIGTT	spherical integral geometric tensor tomography
SOL	soleus
TS	Theiler stage
UL	unloading
WAXS	wide-angle X-ray scattering
XRF	X-ray fluorescence
ZHTT	zonal spherical harmonics tensor tomography
Zn	zinc
Å	Ångström (10^{-10} m)

Table of Contents

1 Introduction

Collagen is the main organic building block of musculoskeletal tissues and fulfils many biological functions. Despite collagen being the smallest load bearing unit, the mechanical functions differ significantly between tissue types [1], with e.g. tendons being highly elastic and energy-storing and bone being very stiff and strong. In bone, the high stiffness originates from the additional inorganic mineral phase, hydroxyapatite, which is interwoven within and between the collagen fibrils. Additionally, a major factor behind the differences in mechanical function and properties between these collagen-based tissues is modifications in their hierarchical organization, from the collagen molecule up to organ scale. The hierarchical structure allows for mechanical optimization at each structural level and as a result, the overall tissue properties are dependent on all of these [2]. It is thus of high importance to understand the characteristics of each level, as well as how they interact and relate to each other.

Both mineralized and non-mineralized collagenous tissues respond to their mechanical loading environment according to specific mechanobiological principles. For example, bone tissue is remodelled continuously such that regions which are less loaded are resorbed and regions which are exposed to high loads are re-enforced through an increased bone formation [3]. Further, when exposed to highly directional loads, both collagen and mineral structures align their main load bearing axes in the loading direction to support the increased load [1].

During human development, it has been shown that prenatal immobilization can cause dramatic effects [4,5]. For instance, multiple neuromuscular diseases which cause reduced or complete lack of movement in utero, have been shown to result in infant and child bones becoming more prone to fracture [6–8]. Bone formation is influenced by the forces from contracting muscles, optimizing the bones to their respective mechanical loading environments. At the embryonic stage, long bones are formed through the process of endochondral ossification, where a cartilage

template is gradually undergoing mineralization [9,10]. Immobilization during this process can result in smaller and deformed bones [5,11–13] with impaired mechanical properties [6,8]. Further, immobilization results in changes of the organization, size and shape of the chondrocytes at the growth plates [12,14,15]. But how immobilization affects the deposition, structure and composition of the developing bones is still unclear.

Both human studies and animal models have shown that mechanical forces are fundamental to maintain tendon health, where both insufficient and excessive mechanical loading can result in injury [16–18]. For instance, reduced mechanical stimuli can cause a reduction of the tendon size, changes in the structural organization and impaired tendon biomechanical properties [18,19]. Within the Achilles tendon, the soleus, lateral and medial gastrocnemius muscles are connected to and exert mechanical stimuli on three sub-tendons, which subsequently are characterized with distinct mechanical properties [20,21]. Further, mechanical stimuli has been shown to influence collagen production, alignment, cell activity and mechanical properties [16,22,23]. However, the effect of reduced loading on the smaller length scales is still unknown.

The Achilles tendon is the most frequently injured tendon in humans and the rupture incidence is increasing not only in athletes, but also within the general population [24–26]. The healed tendon rarely regains its pre-rupture structural or mechanical properties [27,28]. Following this, re-rupture risk of both the previously injured as well as the contralateral Achilles tendon is high [29]. Reduced mechanical loading during the healing process has shown to result in altered mechanical properties and cell activity [30–32], while excessive loading often prolongs the inflammation phase [32,33] and elongates the tendon [34]. Despite this knowledge, there is currently no consensus on optimal treatment after Achilles tendon rupture [28,35,36]. One reason behind this is the limited knowledge on how the local mechanical environment affects the regeneration of the collagen structure.

Histology, immunohistochemistry, tomography and mechanical testing are state of the art techniques to study collagen based hierarchical tissues such as bone and tendon. When it comes to characterizing the structural and compositional changes down at the nanoscale, a range of high-resolution scattering- and spectroscopy-based techniques can be applied. Many of these utilize X-rays which interact with the electron clouds of atoms by either being scattered or absorbed [37]. The scattered X-rays can provide information about the size and organization of both collagen and mineral particles. The absorption of X-rays can cause the emission of characteristic secondary X-rays, which can provide compositional information of atomic elements. These techniques can thus be used to address the current knowledge gaps regarding mechanobiological effects during bone development, as well as during both normal function of Achilles tendons and their healing process.

2 Aim and design of the thesis

The overall aim of the thesis was to characterize the mechanobiological effects on the mineralization process in developing long bones as well as the collagen structure and mechanical response of intact and healing Achilles tendons, by developing a multimodal approach including a range of high-resolution synchrotron-based techniques.

The specific objectives of the individual studies were addressed in three parts:

1) To evaluate the effect of lack of muscles on the mineralization process in developing long bones from embryonic mice, by characterizing changes in structure and composition at the nanoscale (Paper I and II).

2) To elucidate how *in vivo* loading environment affects the structure and mechanics of the intact rat Achilles tendon, by characterizing the collagen structure at micro- and nanoscale in relation to the fibril and tissue mechanical response (Paper III and IV).

3) To explore the impact of *in vivo* loading environment on the regenerating collagen structure in the healing rat Achilles tendon, by characterizing the three-dimensional collagen organization at the micro- and nanoscale, as well as the fibril and tissue mechanical response (Paper V and VI).

Figure 2.1 illustrates the specific aims of the individual studies within the design of the thesis project.

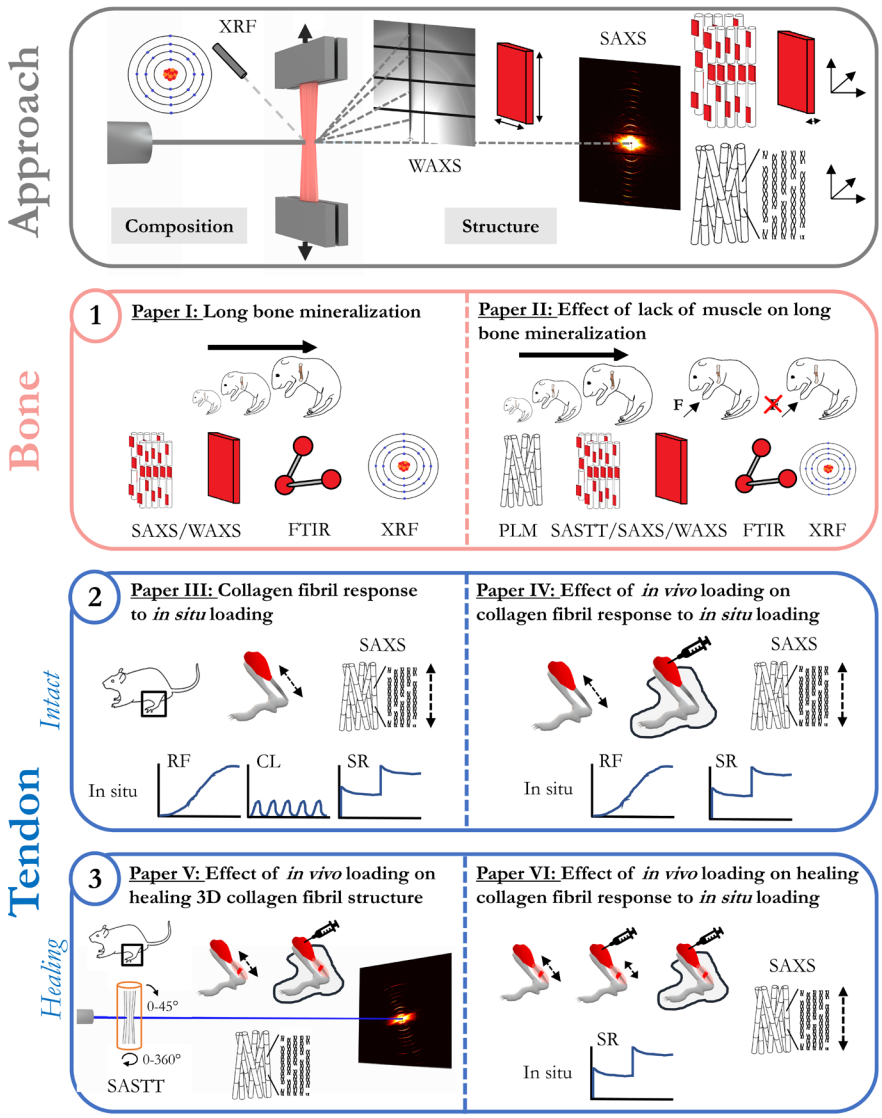

Figure 2.1. Overview of the design of the studies. The roman numerals (I-VI) refer to papers appended in the thesis and are linked to the aforementioned objectives. XRF, WAXS, SAXS, SASTT, FTIR and PLM refers to the techniques used in each study. Ramp to failure (RF), cyclic loading (CL) and stress relaxation (SR) refers to the mechanical tests used.

3 Background

3.1 Bone

Bone primarily consists of approximately 30% of an organic matrix, composed of mostly collagen type I, 60% of a stiff inorganic mineral phase, composed of hydroxyapatite (HA, $Ca_{10}[PO_4]_6[OH]_2$) crystals, and 10% water [38]. These building blocks are arranged into a highly complex hierarchical structure. At the nanoscale, curved platelet-shaped HA crystals are embedded within as well as in-between collagen fibrils (Figure 3.1) [2,39,40]. The collagen fibrils consist of collagen molecules assembled into triple helical structures called tropocollagen (1.5 nm diameter and 300 nm length). The tropocollagen arranges inside the fibrils in an axial quarter staggered manner, creating periodic gaps and overlap regions, which together make up the repetitive sub-unit of the fibrils, d-spacing (~67 nm). The mineral platelets are generally oriented along the main axis of the fibrils. The mineralized fibrils organize into microscale fibers. At the mesoscale, these fibers organize into 3-7 µm lamellae which form two types of bone tissue; trabecular and cortical bone. Trabecular bone is highly porous (~80%) with a sponge-like structure and cortical bone is highly compact, with only ~6% porosity to enable the infiltration of blood vessels and nerves. At the organ scale, cortical bone forms the hard outer shell, such as the shaft in long bones, and trabecular bone forms most of the internal structure.

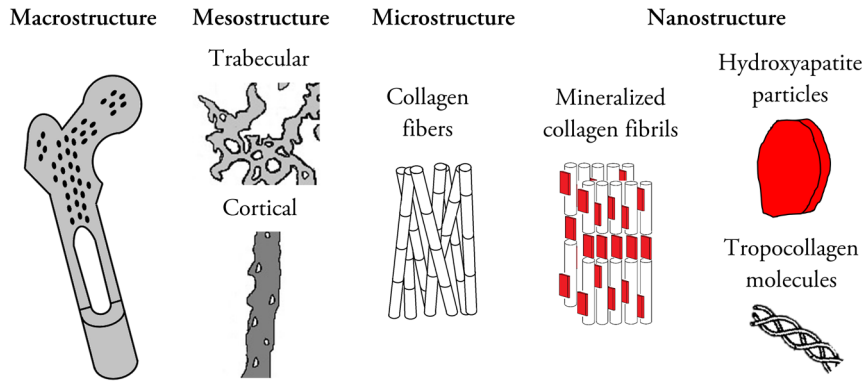

Figure 3.1. Hiearchical strucutre of bone. At the organ scale, long bones consists of trabecular bone forming most of the interal structures and a cortical bone forming a shell arond the midshaft. Mineralized collagen fibers make up the microscale structure, which at the nanoscale are composed of mineralized particles of HA embedded within and inbetween collagen fibrils. The collagen fibrils are made up of quarter staggered tropocollagen molecules.

3.1.1 Bone development

Long bones form through a process called endochondral ossification (Figure 3.2-A) [11,41,42]. In this process, a cartilage template is laid down and then gradually mineralized. The process starts with chondrocytes in the middle of the rudiment becoming hypertrophic (i.e. enlarged). The hypertrophic chondrocytes primarily synthesize collagen type X, attract blood vessels, chondroclasts (which digest cartilage matrix) and osteoblasts, which replace the degraded cartilage tissue with trabecular-like bone. Additionally, the hypertrophic chondrocytes direct perichondral cells to differentiate into osteoblasts which form an initial bone collar. This initial mineralized region at the middle of the cartilage template is called the primary ossification center. More blood vessels invade, and the primary ossification center is then divided into two zones of ossification, termed growth plates (Figure 3.2-B). Closest to the mineralized tissue, the hypertrophic chondrocytes undergo apoptosis, and their surrounding cartilage matrix serves as scaffold on which the osteoblasts can continue to lay day down mineralized tissue. This zone is called the mineralization zone. In front of the mineralization zone is the hypertrophic zone in which the hypertrophic chondrocytes reside. In front of the hypertrophic chondrocytes is the proliferation zone, in which chondrocytes proliferate and synthesize cartilaginous extracellular matrix (mainly collagen type II) to enlarge the cartilage template. These chondrocytes have a discoid shape and form oriented columns to direct the elongation of the rudiment in the longitudinal direction. Above the proliferating chondrocytes rests more spherical inactive

chondrocytes and is thus called the resting zone. As the growth plates go through these sequential processes of chondrocyte proliferation, extracellular matrix synthesis, hypertrophy, matrix mineralization and apoptosis, they gradually progress longitudinally in opposite directions, along the diaphysis of the long bone, to eventually replace the cartilage template entirely with mineralized bone-like tissue. Growth of long bones in humans continues until adolescence, upon which the growth plates disappear. Growth plate closure is also commonly occurring upon sexual maturation in most other mammals, with the exception of mice and rats, in which the longitudinal bone growth continues throughout most of their life span [43].

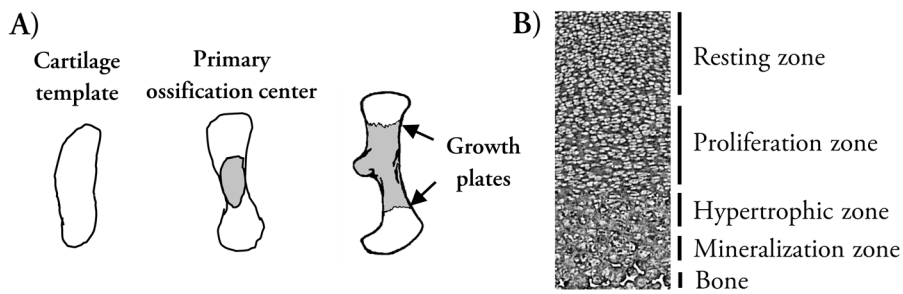

Figure 3.2. Long bone development. A) Long bones form through endochondral ossification, where a primary ossification center is formed in the center of the cartilage template. As mineralization progresses, the primary ossification center is split into two secondary ossification centers, i.e. growth plates. B) The different zones of the growth plate.

Amorphous calcium phosphate (CaP) precursors have been found in osteoblasts as well as hypertrophic chondrocytes, enclosed in intracellular vesicles [44–49]. Within these vesicles, Ca and P ions crystallize into apatite minerals. The tissue is hypothesized to be mineralized upon the release of these vesicles into the extracellular matrix (ECM). However, other studies have found that the Ca concentrations within hypertrophic chondrocytes at the growth plate is low and deemed it unlikely that growth plate mineralization depends solely on the release of intracellular vesicles [50–53]. Thus, an additional pathway has been suggested, of which vesicles containing precursor CaP are delivered to the site of mineralization directly from blood vessels [45,52,54]. Despite the numerous studies being conducted on endochondral ossification, the pathway of mineralization during this process is still not clear.

3.1.2 Mechanobiology of bone development

There is a range of neuromuscular diseases which cause reduced or a complete lack of muscle contractions, such as cerebral palsy, congenital myotonic dystrophy or spinal muscle atrophy. It has been shown that the abnormal mechanical environment during fetal development due to these diseases has a dramatic effect on the developing skeleton [6,7,55–57]. Human infants and children with these neuromuscular diseases have bones which are thinner, less mineralized and sometimes more elongated [6,7]. These bones have been shown to have impaired mechanical properties and to be more prone to fracture, with studies on newborns showing that some bones already fractures *in utero* [6]. In addition to this, an abnormal mechanical environment *in utero* can lead to deformed joints [42,58], resulting in e.g. developmental dysplasia of the hip, which occurs in 1 out of 100 newborns [59]. Postnatal pathologies such as temporary brittle bone disease are also believed to be attributed to decreased fetal movement [60] and 10% of pre-term infants have an increased susceptibility to fracture, potentially due to early removal of important loading such as the kicks against the uterine wall [61].

While some of the early studies on the effects of an abnormal mechanical environment were performed on newborns, infants and children, currently chick and mouse models have been developed to enable detailed characterization of the mechanisms involved. Chick models have been extensively used due to their external development in the egg, which easily allows for alterations and manipulations during this process [42], and their long bone development being similar to mammals. For example, neuromuscular blocking agents, such as decamethonium bromide or botulinum toxin (Botox), can be used to alter muscular activities. A multitude of studies have found that immobilization during avian bone development results in abnormal bone curvatures [62], thinner and shorter bones, bone fusion, decreased growth rates and chondrocyte proliferation [62–64]. Additionally, immobilization has been shown to alter the expression patterns of the genes encoding collagen type X and Indian hedgehog [65], which are two highly involved proteins in bone formation.

However, chicks do not develop a primary ossification center nor vascularization of the cartilage template before mineralization. Additionally, despite the majority of mineralization in chick long bones takes place at the extremities of the shaft, they seldom have growth plates [66–68]. To better mimic human long bone development, mouse models are widely used as they provide a more similar development process, while still allowing for gene modifications and a controlled environment. A multitude of studies on fetal immobilization in mice have found that immobilized bones are shorter, rounder, has a less tapered geometry and decreased mineralization [12,69–71]. Additionally, alterations of the growth plate, such as chondrocyte density, size and elongation, have been found [12,14,72]. A wide range

of genetically modified mouse models are commonly applied to study alterations in mechanical environment on skeletogenesis and differences have been observed between both immobilization models as well as different bones [70]. To study the complete lack of skeletal muscles, there are two common mouse models. In $Pax3^{Spd-/-}$ mice, the transcription factor Pax3 is lacking and as a result muscle progenitor cells cannot migrate into the limb buds and form skeletal muscle [73]. In double knockout $Myf5^{nlacZ-/-}$:$MyoD^{-/-}$ mice, the progenitor cells can migrate to the limb buds, but instead cannot differentiate into myoblasts which forms muscle fibers [74]. To study only reduced muscle function, littermates from the double knockouts, which have one functional copy of Myf5, i.e. $Myf5^{nlacZ-/+}$:$MyoD^{-/-}$, are typically used as they can still form muscle fibers, but with a reduction of 35-55% [69]. Lastly, a model of muscular dysgenesis, mdg/mdg, which disrupts the coupling between muscle excitation and contraction, can be used to study the presence of non-contractile muscle [75].

3.2 Tendon

Tendons connects muscles to bones in order to provide movement. Tendons consists of approximately 70% water and 30% organic matrix, mainly composed of collagen type I [1,76]. The collagen network is arranged into a highly complex hierarchical structure, from molecules up to organ scale. At the nanoscale, tropocollagen molecules (1.5 nm diameter and 300 nm length) are organized in a quarter-staggered manner into fibrils at a periodic distance, d-spacing, of ~67 nm (Figure 3.3). The fibrils are interconnected and stabilized by both inter- and intrafibrillar crosslinks [77,78]. At the microscale, fibrils bundle into fibers which at rest exhibit a waviness called crimp [79,80]. Fibers organize into fascicles and/or sub-tendons, which then together make up the full tendon. The Achilles tendon consists of three sub-tendons which connect the tendon to the calf-muscles; medial gastrocnemius (MG), lateral gastrocnemius (LG) and soleus (SOL). In-between all collagen structures are compartments of different proteins and cells, such as e.g. elastin, proteoglycans and tenocytes [76]. Surrounding the tendon is a compartment called the paratenon, which contains fibroblasts and progenitor cell populations, as well as blood vessels and nerves.

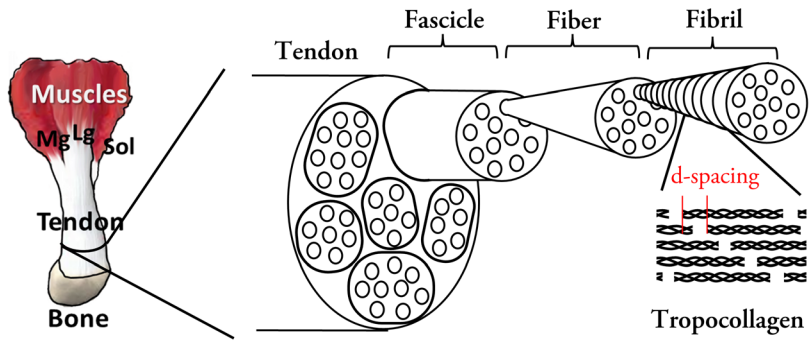

Figure 3.3. Hierarchical structure of tendons. At the organ scale, the Achilles tendon connects the heel bone to the calf muscles Mg, Lg and Sol. At the mesoscale, tendons consists of sub-tendons and/or fascicles, which in turn are made up of collagen fibers at the microscale. At the nanoscale, these fibers consists of collagen fibrils, which are made up of quarter staggered tropocollagen molecules at a period distance called d-spacing.

3.2.1 Tendon mechanobiology

Mechanical stimulation is fundamental to maintain tendon health [16,17]. Tendon cells are mechanosensitive, adapting their activity to altered levels of physical load and as a result altering the tissue properties [81–83]. Short-term exercise has been shown to increase the turnover of collagen type I in human Achilles tendons as well as level of collagen cross-linking, whereas long-term exercise results in an increase in cross-sectional areas as well as stiffness [16,84]. Prolonged inactivity on the other hand decreases both collagen type I synthesis and cross-sectional area, as well as tendon stiffness [85–88]. Returning too quickly to intense training after a period of inactivity, or intermittently engaging in sports whilst otherwise living a sedentary lifestyle, results in a high risk of tendon rupture [89,90]. The resulting changes in tendon properties due to inactivity most likely directly affects the risk for rupture once the tendon is loaded again.

Despite exercise often being beneficial to maintain tendon homeostasis, both insufficient and excessive loading can have severe consequences [17,91]. Overuse of the tendon often results in tendinopathy, which is characterized by pain, swelling and long-term impaired performance [17,91]. The prevalence of tendinopathy is increasing and affects 23.9% of athletes and 5.9% of the general population [92,93]. The prevalence of tendinopathy increases with age and is more common in women than men [94]. Tendinopathy is believed to be caused by microinjuries and subsequent inflammation due to repetitive overload strains [91]. Collagen degradation during tendinopathy seems to be higher than the collagen synthesis [95]. This results in loss of structural collagen organization. Additionally,

accumulation of more disorganized, mechanically inferior collagen type III within the tendon occurs in an attempt to repair the microdamage [91].

Similarly as in humans, both immobilization and overuse studies in animal models have found detrimental effects on the mechanical properties of the Achilles tendon. In these models, inactivity is represented by a reduced loading achieved through paralysis of the calf muscles by Botox injections [22,31], tail suspension [96,97] or cast immobilization [98,99]. Free cage activity represents normal loading whereas excessive loading or overuse often is induced by subjecting the animals to extended treadmill running [100–102]. Tail suspension for 3 weeks has shown to result in decreased maximal stress, elastic modulus as well as capacity for energy absorption of the rat Achilles tendon [96], and after 5 weeks also a decrease in thickness of collagen fibers [97]. 4 weeks of cast immobilization of rabbits hindlimbs has been found to decrease maximal stress and stiffness [99], as well as reduce viscoelasticity and result in a more disorganized fiber network [98]. Calf muscle paralysis induced by Botox in rats for 5 to 6 weeks has shown a reduction in viscoelastic properties such as creep and hysteresis, as well as an increased elastic modulus [31,103]. Additionally, calf muscle paralysis resulted in a more disorganized fiber network and an increased collagen content [22]. None of these studies on Achilles tendon immobilization found any significant changes in cross-sectional area. A study subjecting rats to 12 weeks of uphill treadmill running found that the increased activity resulted in a more disorganized fiber network and increased cell numbers [101]. Another study revealed that 8 weeks of downhill running results in cell proliferation and fiber disorganization, as well as decreased stiffness and maximum stress [102]. However, another 12 week uphill running study instead found that their rats adapted to the increased loading environment, showing no signs of tendinopathy but instead tissue improvements [100]. In this study, the increased activity resulted in a higher elastic modulus and maximum stress, as well as an increased expression of collagen type III, but no changes in collagen type I. Additionally, a decrease in non-collagen matrix components, matrix degrading enzymes and growth factors was observed.

3.2.2 Mechanobiology of tendon healing

During Achilles tendon healing, the tissue is restored through three overlapping phases; 1) inflammatory, 2) reparative and 3) remodeling phase [18,28] (Figure 3.4). Most studies characterizing the healing process of Achilles tendons have been conducted on animals. In rodents, the initial inflammatory phase last for 24h to few days and is characterized by an influx of blood and immune cells, such as erythrocytes, neutrophils, monocytes, macrophages, as well as vascularization. These cells digest the necrotic tissue and release chemotactic agents which attracts blood vessels and direct fibroblasts to start collagen synthesis. After a few days, the

healing enters the reparative phase, which is characterized by intense matrix production, resulting in the formation of a so-called callus in-between the previously intact stumps. Initially, a disorganized collagen type III network is laid down to restore the structural integrity of the healing tissue [104]. The production of collagen type III then shifts to more aligned type I within the first few weeks of healing [28]. After approximately 6 weeks of healing, the cell presence as well as matrix synthesis decreases as the healing enters the remodeling phase [18]. During this phase, the matrix is remodelled into more fibrous and ultimately scar-like tissue, and bonding between collagen fibers is increased. The majority of the collagen alignment takes place during these first few weeks [105,106], but an alignment similar to that of uninjured tendons has still not been reached after 16 weeks in rats [107,108]. Additionally, neither fibril nor material mechanical properties return to pre-rupture values during this period [28]. In humans, the remodeling phase can last more than a year and the tendon never completely regains its pre-rupture properties [109].

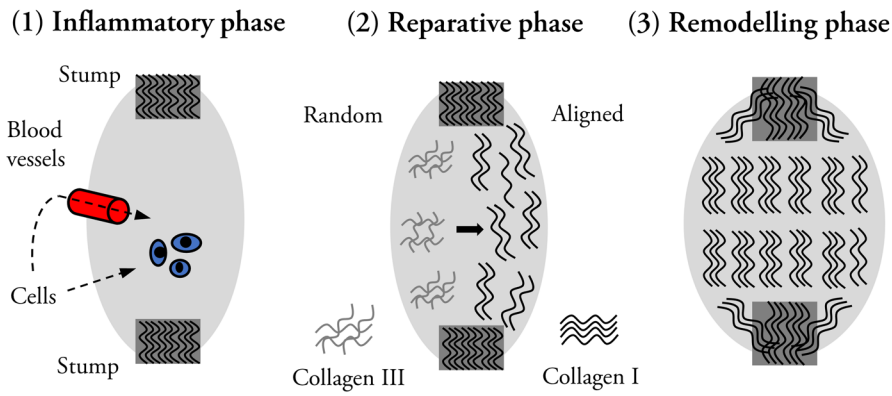

Figure 3.4. The three stages of tendon healing. In the inflammatory phase, the callus is populated by immune cells and blood vessels. In the reparative phase, a disorganized network of collagen type III is laid down and replaced by a more well-aligned matrix of collagen type I. In the remodeling phase, the tissue is remodelled into a more fibrous matrix and bonding between fibers is increased.

Studies have shown that the healing process of tendons is highly heterogeneous. Scleraxis-lineage cells have been shown to egress from the stumps and into the callus core during early healing [110,111]. Scleraxis-lineage cells are the main governing cells during tendon healing, critical for tissue formation to bridge the gap between stumps. The spatial distribution of these cells overlap with collagen formation [111], which also seem to start from the sides of the stumps [105]. In the central region between the stumps, both evidence showing initial collagen formation primarily at the core [105] as well as in the periphery has been found [30].

Post-injury rehabilitation protocols of tendons are still highly debated [35]. Immobilization in the form of casts or slings is often utilized to avoid re-ruptures [35,112]. Additionally, Botox injections to indue short term muscle paralysis has also shown clinically favourable results [35], such as increased range of motion as well as no re-ruptures [113]. However, prolonged immobilization increases the risk for joint stiffness as well as muscle atrophy [114], thus reducing the ability of the patient to return to normal activities. Early mobilization prevents this, and has been shown to improve the healing process [114], as well as decrease pain and increase overall function [115,116].

Numerous animal studies have been conducted to further elucidate the outcomes of different loading environments during tendon healing. The results from these studies are however highly inconsistent and most studies only evaluate the first few weeks of tendon healing, rendering the details of long-term effects and complete healing unknown. One study investigating healing rat Achilles tendons subjected to 2 weeks of unloading through cast immobilization showed that unloading led to ~83% decreased collagen type III content [117]. In line with this, gene expression of both collagen type I and III has been found to decrease with unloading [32]. However, another study instead showed an increase in both collagen type I and III expression during the first week of unloading by Botox injections, to then also become lower than free cage activity after 2 and 3 weeks [118]. Studies have found the ratio between collagen type I and III to remain similar independent of unloading period by cast immobilization, as well as with or without surgical repair [119–121]. Unloading also seems to affect collagen cross-linking, but studies show contradictory results; both decreased [32] and increased [118] expression following unloading has been found. Additionally, unloading seems to decrease collagen alignment [122] as well as increase adipocyte differentiation [122]. In unloaded tendons, adipocytes also surround the healing tissue instead of being interspersed within it [30]. Loading on the other hand, seems to alter the cell distribution within the healing tendon, by e.g. an increased presence of inflammatory as well as bone-like cells [122,123]. Loading also increases the gap distance between stumps, elongating the tendon [34], as well as increasing the cross-sectional area [34,119]. These structural differences could be why unloading has been shown to slow down the recovery of both structural and material mechanical properties during early healing [28].

3.3 Tissue characterization

In this section, the characterization techniques used in this thesis are introduced.

3.3.1 Synchrotron-based X-ray imaging

X-rays are radiation with wavelengths on the scale of 1 ångström (Å) and they interact with electrons of atoms [37]. X-rays are either transmitted through matter unchanged (i.e. no change in energy or direction) or interact with matter in predominantly two ways: either through absorption or scattering. When X-rays are absorbed, their energy will be transferred to an electron which is expelled from their atom. As a result, the atom becomes ionized and energetically unstable. The atom will relax back into its ground state through either fluorescence emission or Auger electron emission. When X-rays are scattered, they will change their direction and either retain (elastic) or change (inelastic) their wavelengths, i.e. energy. When X-rays are elastically scattered, they will cause the electrons to oscillate at the same frequency as them and emit photons of the same wavelength. Interference between these emitted photons will either be constructive or destructive, depending on if they are in or out of phase with each other. The interference will result in a detectable pattern at specific distances, which contains information about the structure of the probed material.

The intensity I of X-rays which pass through matter will exponentially attenuate according to:

$$I = I_0 e^{-\mu x} \tag{3.1}$$

where I_0 is the incoming X-ray intensity, μ the linear attenuation coefficient and x the distance travelled [124]. The attenuation depends on the composition and density of the probed material, as well as the energy of the X-rays. The attenuation decreases with increasing X-ray energy as well as atomic number and increases with increasing density of the material.

At synchrotron facilities, X-ray beams with high brilliance are produced [37], i.e. highly coherent X-ray beams with high-intensity and low divergence. Brilliance is defined as number of X-rays emitted per unit time through a unit area, per unit of solid angle of the beam cone, within a 0.1% range centred around a specific wavelength (photons s^{-1} mm^{-2} $mrad^{-2}$ $0.1\%BW^{-1}$). The high brilliance of synchrotron radiation is achieved by accelerating electrons to approximately 2-8 GeV using a linear accelerator and often a circular booster. The accelerated electrons are then inserted into the storage ring, where they are guided around the ring using magnetic devices. So called bending magnets force the electrons to deviate from their straight paths, causing energy release in the form of X-rays. In

addition to the bending magnets, wigglers and undulators are placed within the straight sections of the ring to produce brighter X-ray beams. Wigglers and undulators are series of dipole magnets, which force the electrons to oscillate in one plane and release X-rays at each oscillation along the device, increasing the resulting X-ray beam intensity or coherence depending on the device. The produced X-rays are guided tangentially out of the storage ring by different so-called beamlines. Along the beamline optical elements are placed to select and tune the desired characteristics of the X-ray beam. At the end of the beamline there is an experimental station, where the X-rays are utilized for a wide range of applications, including material characterization.

3.3.2 X-ray micro-computed tomography

The contrast in X-ray attenuation between different materials can be exploited to visualize the architecture and composition of objects. By recording the transmitted X-rays through an object, a shadow image, referred to as a projection, containing intensity variations dependent on the attenuation of the materials in the path of the beam can be obtained (Figure 3.5-A). By acquiring these projections at rotational angles in-between 0-180° around the object, the 3D intensity distribution of the object can be computed from these using algorithms [125], such as filtered back projection or iterative reconstruction. In this way, computed tomography (CT) provides a 3D image of the object and enables full visualization of its internal structures and composition.

In bone, the main attenuating feature is the HA component [126]. HA is significantly more attenuating than both air and the surrounding soft tissue, which creates high contrast and allows for characterization of features such as bone volume, porosity, density and the microstructural architecture [127–130].

In soft tissues such as tendons, however, the contrast between the different components as well as in relation to air is very low [126]. This makes imaging of these tissues very challenging. However, as X-rays pass through a material, they will change phase, depending on the refractive index of the material. As a result, X-rays passing through materials with different refractive indices within an object will have different phases and the wavefront of the transmitted X-rays will change shape due to their interference [131]. The X-ray intensity thus becomes:

$$I = I_0 e^{i(1-\delta)x} e^{-\mu x} \tag{3.2}$$

where δ is the refractive index decrement. Thus, by placing the detector at a longer distance from the object the distorted wave front will generate a structural pattern from which the phase changes can be retrieved (Figure 3.5-B) [132,133]. In this manner, edges between materials can be enhanced and generate tissue contrast

despite the similarity in attenuation coefficients. Phase contrast μCT has thus recently been applied to study a range of soft tissues, such as muscles, heart, brain, lungs, ligaments, vessels, cartilage [12], intervertebral discs, nerves, menisci [134] and tendons [135,136].

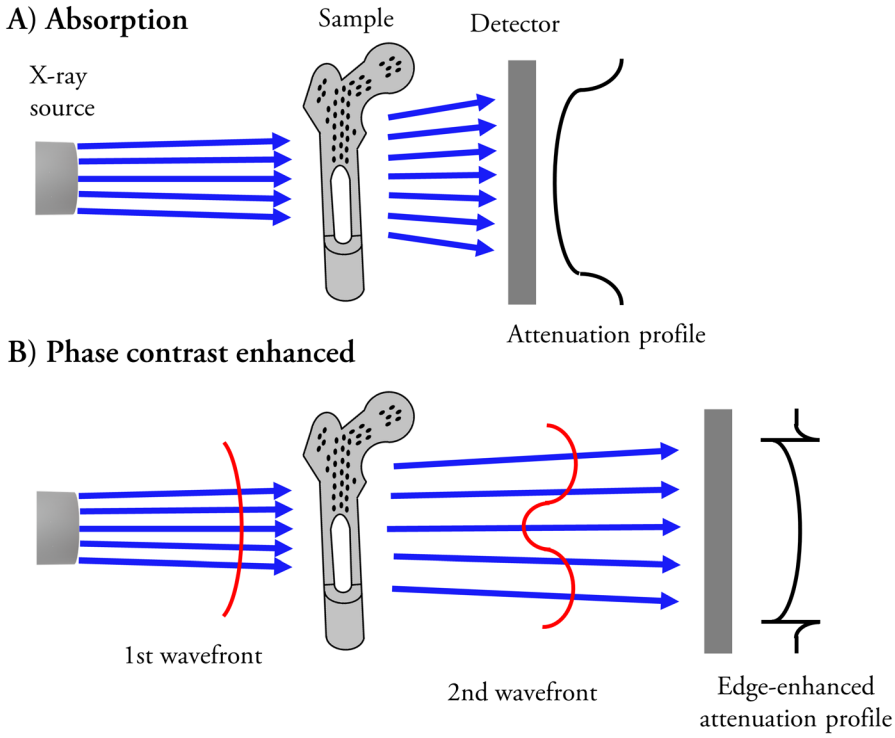

Figure 3.5. Different types of X-ray tomography. A) In absorption-based tomography a shadow image of the object is recorded, where the attenuation profile follows the difference in electron density within the sample. B) In phase contrast enhanced tomography the detector is placed further away from the sample and the wavefront is distorted and interfaces between materials become enhanced.

3.3.3 X-ray scattering

X-ray scattering can be used to evaluate the nanostructure and -orientation of materials. When an incoming X-ray beam (defined by vector $\overrightarrow{k_i} = 2\pi/\lambda$) with wavelength λ interacts with the electron cloud of a sample, part of the beam will be scattered ($\overrightarrow{k_s}$) at an angle θ (Figure 3.6-A). Analysis of the scattering data is done in the reciprocal space, by defining the scattering vector q as the difference between incident and scattered beam $\vec{q} = \overrightarrow{k_i} - \overrightarrow{k_s}$. As the energy is preserved in elastic scattering, the scattered beam will have the same magnitude as the incident

beam and thus fulfils Bragg's law and relates to the size of the scattering structure d in real space through:

$$q = |\vec{q}| = \frac{4\pi}{\lambda} sin\left(\frac{\theta}{2}\right) = \frac{2\pi}{d} \quad (3.3)$$

The scattered beam is recorded by a detector positioned behind the sample and the 2D scattering data can be analyzed as a function of q, by integrating the scattering intensity radially. This yields a 1D curve $I(q)$ which provides information such as size and periodicity of the nanoscale structures in the sample. The 2D scattering data can also be analyzed as a function of angle φ by instead integrating azimuthally, which yields a 1D curve $I(\varphi)$ with information about the orientation and alignment of the structures at the nanoscale. The probed length scale is determined by the wavelength of the incident X-rays and the detector distance. As the q vector is inversely proportional to the real space distances, large structures (such as collagen fibrils, mineral particles) will scatter at small angles and small structures (crystallites, molecules) will scatter at wide angles.

In bone, the main scattering features at the nanoscale is the HA mineral particles and the collagen fibrils (Figure 3.6-B). At small angles (0.1-10°), i.e. small-angle X-ray scattering (SAXS), the intensity of the scattered beam $I(q)$ can be defined in terms of the form factor $P(q)$, describing the shape and polydispersity of the probed particles, and the structure factor $S(q)$, which relates to the interaction between neighbouring particles. Several models have been developed to evaluate the thickness of the mineral particles in bone. A model to estimate mineral thickness was developed by Fratzl et al. [137,138], utilizing that the scattering intensity $I(q)$ decays with Pq^{-4} at high q-values, according to Porods law. From this so called Porod region, the Porod constant P can be retrieved, as well as the Porod invariant Q. This model assumes bone to be a mixture between mineral particles and collagen and takes into account the scattering length density difference between them as well as their volume fractions (Φ). In another model developed by Bünger et al. [139] the mineral particles are assumed to be platelets with a finite thickness, T, and with infinite sizes in the other two dimensions. Additionally, the model takes into account that multiple particles cannot occupy the same volume and accommodates for inhomogeneities in electron density due to e.g. closely positioned particles, through an effective structure factor to describe fractal

$$S_{frac}(q) = 1 + Aq^{-\alpha} \quad (3.4)$$

fluctuations at low q:

where α is the fractal dimension of the fluctuations.

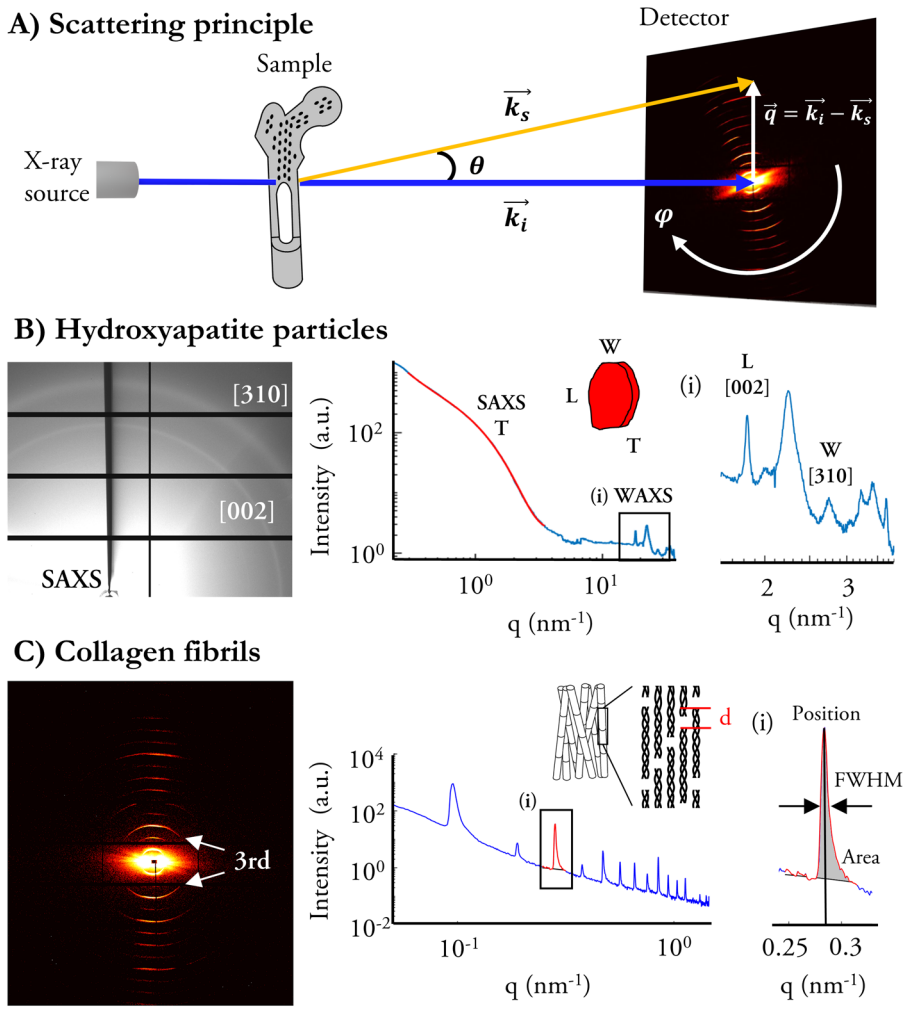

Figure 3.6. Principles of X-ray scattering. A) Schematic representation of X-ray scattering, where the incoming beam interacts with the sample and scatters at specific angles. The difference between the incoming and the scattered beam defines the scattering vector q. B) Representative scattering pattern and I(q) curve from bone, indicating the SAXS scattering related to the platelet thickness (T), length (L) and width (W) of coherent blocks in the [002]- and [310]-direction. C) Characteristic scattering pattern and I(q) curve from tendon, showing the collagen scattering peaks and their relation to fibril structural parameters.

The final expression for the total intensity in the Porod-region which can be fitted to estimate the thickness of the mineral particles thus becomes:

$$I(q) = P_{eff}(q)S_{frac}(q) \tag{3.5}$$

At wide angles (>10°), i.e. wide-angle X-ray scattering (WAXS), the beam will scatter at specific angles related to the crystal planes and their corresponding dimensions D can be determined from the full width at half-maximum (FWHM) of their corresponding scattering peaks according to the Scherrer equation:

$$D = \frac{K\lambda}{FWHM\ cos\ \theta} \tag{3.6}$$

where K is a constant related to the crystal shape and θ the scattering angle. From the [002] and [310] reflections the length and width of coherent blocks in the [002], i.e. along the *c*-axis, and [310], i.e. along the *ab*-plane, directions respectively of the HA crystal can be estimated.

Both SAXS and WAXS are frequently used to assess the nanostructure of bone and has been fundamental in providing our current knowledge on bone maturation and growth, fracture healing, aging and pathologies. HA mineral particles in healthy bone have been found to be aligned with the collagen fibers and have a size of 2-5 nm in thickness, 30-100 nm in length and 10-30 nm in width [140–144]. Newly formed bone however, e.g. following fracture or around implants, instead has smaller and less aligned HA particles [145–149].

The main scattering structure of tendons at the nanoscale is the collagen fibril (Figure 3.6-C). The collagen reflections related to the fibril d-spacing scatters at periodic intervals of 0.094 nm^{-1}. The 3rd collagen peak (positioned at 0.028 nm^{-1}) is typically characterized due to it being the first uneven reflection outside of the low q region where interactions from larger scale structures are more prominent, such as the fibril diameter. From the peak position d-spacing can be retrieved and fibril delamination or strain heterogeneity can be estimated from the peak FWHM. From the ratio in peak area of two consecutive peaks, e.g. I_3/I_2, changes in overlap O due to e.g. sliding of adjacent collagen molecules within the fibrils can be estimated. The relationship between two peaks can be described by:

$$\frac{I_m}{I_n} = \left(\frac{n}{m}\right)^2 \left[\frac{\sin(m\pi O/d)}{\sin(n\pi O/d)}\right]^2 \tag{3.7}$$

where m and n are peak orders and I_m and I_n their peak areas. When a degree of intrafibrillar disordering is present, higher order peaks will experience a larger reduction in intensity compared to lower order peaks and from the ratio between two uneven peaks, e.g. I_5/I_7, changes in intrafibrillar disorder can be estimated.

To describe this relationship, a Debye-Waller type factor ($-\kappa q^2$) can be applied, where κ is proportional to the disordering and $q_n = 2\pi n/d$:

$$\frac{I_m}{I_n} = \left(\frac{n}{m}\right)^2 \left[\frac{\sin(m\pi O/d)}{\sin(n\pi O/d)}\right]^2 exp\left(-\kappa(m^2 - n^2)\left(\frac{2\pi}{d}\right)^2\right) \quad (3.8)$$

SAXS is commonly applied to study the nanostructure of tendons and has been crucial in determining the current concepts of collagen fibril deformation. By combining SAXS with mechanical testing, collagen fibrils have been found to elongate through molecule extension, elongation of gap regions as well as sliding between adjacent collagen molecules within the fibrils [150–158]. The fibril d-spacing has also been shown to be dependent on hydration state, with dry fibrils being significantly shorter than wet ones [103,159–161], and to be reduced by extended immobilization [22]. Newly formed collagen fibrils, of e.g. healing tendons, has also been shown to have shorter d-spacing than those of intact, uninjured tendons [30].

3.3.4 SAXS tensor tomography

Through recent method developments combining SAXS with tensor tomography (SASTT), the 3D structural organization of the nanoscale can be probed [162–165]. In conventional X-ray tomography, each voxel is related to a scalar intensity value. Therefore, the property of each voxel is rotationally invariant, and their values can be reconstructed by acquiring projections at a range of rotational angles, as described above. However, in an anisotropic material, the nanoscale structures have an anisotropic electron density distribution and thus gives rise to a non-uniform scattering around the rotation axis, containing both orientational and structural information. Therefore, the properties of a voxel probed by SAXS cannot be described solely by a scalar value. In practice, this results in the scattering contribution from one voxel not being independent of the rotation. Thus, in order to reconstruct the scattering information in 3D, an additional axis of rotation perpendicular to the conventional tomographic axis is needed (Figure 3.7) [162,166]. This additional axis of rotation is referred to as the tilt axis.

Several methods utilizing tensors to model the 3D reciprocal space map of a voxel has been proposed [162–165]. In the Zonal spherical Harmonics Tensor Tomography (ZHTT) method developed by Liebi et al. [162], the sample is scanned in two dimensions, producing 2D projections containing scattering patterns in each pixel, at equally spaced rotation angles around equally spaced tilt angles in-between 0-45°. At 0° tilt the projections are acquired in-between 0-180° and at other tilt angles in-between 0-360°. The 3D reciprocal space map in each voxel is then reconstructed from these projections as a tensor by band-limited functions on the unit sphere in a representation of even order (ℓ) spherical harmonic basis functions Y_ℓ^m with cylindrical symmetry (m = 0) and two Euler angles describing the unit

vector of the main scattering orientation to which the spherical harmonic coordinate system is rotated in each voxel. The reconstruction is based on a four-step iterative parameter optimization which minimizes the error between the measured and modeled scattering. The optimization is performed in four steps: 1) optimization of the isotropic component ($\ell, m = 0$), 2) optimization of the preferential angular direction with fixed coefficients ($\ell \leq \ell_{max}$), 3) optimization of coefficients ($\ell \leq \ell_{max}$) with fixed angles and 4) simultaneous optimization of both angles and coefficients.

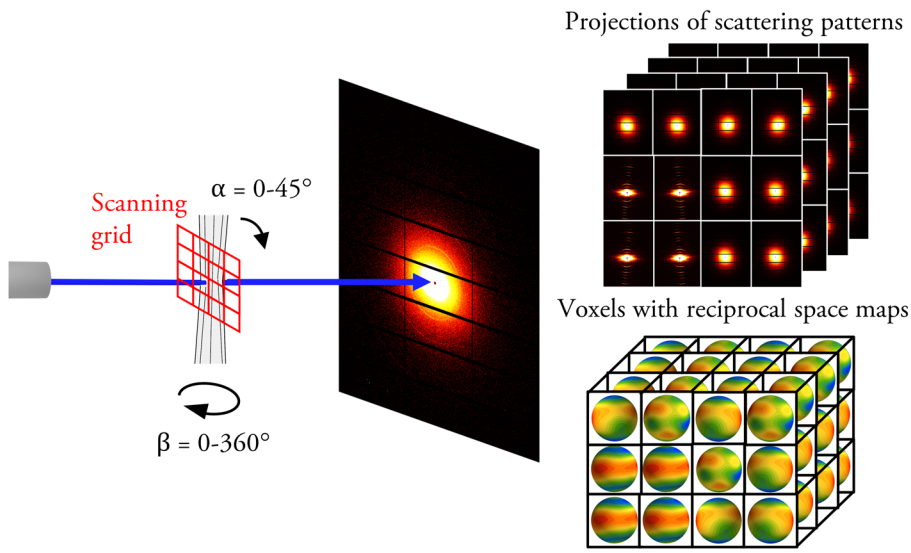

Figure 3.7. Schematic illustration of SAXS tensor tomography. The sample is scanned at equally spaced rotational angles at several tilt angles. Each scan results in a projection of scattering patterns across the scanned area. The 3D reciprocal space map in each voxel is reconstructed from these projections by tensors, using a set of spherical harmonic basis functions.

Due to its cylindrical symmetry (i.e. m = 0), the ZHTT method provides fibre-symmetric orientations. The recently developed Spherical Integral Geometric Tensor Tomography (SIGTT) method by Nielsen et al. [167] expands the optimization algorithm by also introducing even degrees of $m \leq |\ell|$, thus allowing a less restricted symmetry of the spherical harmonic basis functions as well as more robust reconstructions.

SASTT has been applied to study the nanostructure of mineralized tissues such as bone, soft polymers and myelinated axons in neural tissue [168–173]. It has been used to evaluate the orientation and structure of the HA particles in healthy bone [168,171] as well as fracture healing and implant integration [169,170].

3.3.5 X-ray fluorescence

X-ray fluorescence (XRF) can be used to evaluate the elemental composition of materials. When an incoming X-ray beam interacts with the electron cloud of a sample, photons will excite an electron from one of the inner shells (lowest energy) of the atom. For the excitation to happen, the energy of the incoming X-rays needs to be higher than the energy between inner and external electron shells. The excited electron will be ejected, leaving a hole in a low energy shell and thus making the atom energetically unstable (Figure 3.8-A). To get back into a stable state, an electron from a higher energy shell will drop down to fill the hole, which relaxes the atom and results in a release of energy. The excess energy is released either through fluorescence emission of a photon, called secondary X-ray, or by the ejection of another electron from one of the higher energy shells, called an Auger electron. Fluorescence emission is the most probable process in heavier elements, whereas in lighter elements Auger electron emission is most probable. The released energy corresponds to the energy difference between these lower and higher energy shells and is thus characteristic of the excited atomic element. The emitted secondary X-ray will always be lower than the energy of the incident X-rays and is typically referred to as a combination of the lower energy shell from which the first electron was ejected (K, L, M, etc) and how many levels the second electron has dropped ($L \rightarrow K = \alpha, M \rightarrow K = \beta, \ M \rightarrow L = \alpha$) [174].

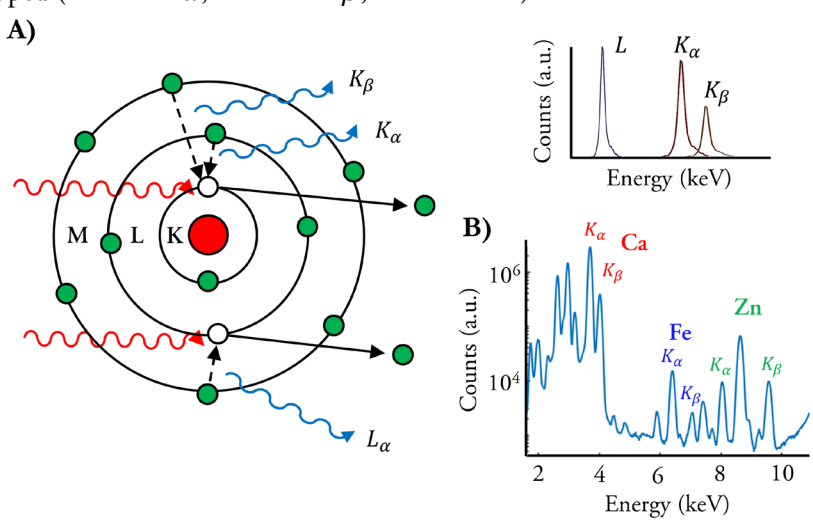

Figure 3.8. Principles of X-ray fluorescence. A) A high energy incident X-ray beam can eject inner shell electrons. Electrons from higher energy shells will drop down to fill the vacancy and energy will be released as secondary X-rays, which energies depend on the difference between the ejected and relaxing electron shells. C) Characteristic XRF spectrum from embryonic bone, highlighting K-emission from Ca as well as the common trace elements Fe and Zn.

In a composite material such as bone, the incident X-ray beam will excite several elements simultaneously, resulting in an X-ray fluorescence spectrum. The spectrum can be recorded using a detector sensitive to a wide range of energies. The recorded XRF spectrum will not only contain peaks characteristic to the elements within the sample but will also be influenced by the Bremsstrahlung radiation, which gives rise to a broad continuous background, as well as Compton scattering, which gives rise to a big peak close to the energy of the incident X-ray beam. Additionally, the spectrum can also be influenced by artefacts such as escape peaks, which are due to the secondary X-rays inducing fluorescence in the detector elements, and pile-up, which is when several secondary X-rays hit the same detector element at the same time. Additionally, other materials irradiated by the incident beam such as beam stops, instrumentation, detector collimators, filters, and air will also produce non-sample related peaks in the spectrum. The lowest element which can be detected highly depends on the setup, e.g. if it is in air, helium or vacuum, as well as the distance to the detector.

As the main constituent of HA, Ca is the most abundant element of bone which can be evaluated by XRF (Figure 3.8-B). Other elements are however also present in small quantities in bone, called trace elements. Common trace elements fundamental to bone health are zinc (Zn), iron (Fe), magnesium, strontium, copper, manganese, fluoride, boron and silicon [175,176]. Zn has been found in increased levels at the tidemark of articular cartilage [177,178], as well as at sites of ossification in postnatal cochlea [179].

3.3.6 Fourier transform infrared spectroscopy

Infrared radiation (IR) has wavelengths within the range of 700 nm to 1 mm. When IR radiation interacts with biological tissues, they are typically absorbed by molecular bonds. The absorbed incoming IR radiation changes the vibrational and rotational levels of the bonds (Figure 3.9-A). Vibration of molecular bonds are defined as either stretching or bending, in which the bond either changes length or angle. Stretching vibrations can be either symmetric or asymmetrical. In order for the molecular bonds to absorb IR radiation, the energy of the incoming radiation needs to be equal to the difference between the excited and the ground state of the molecule, and the incoming radiation needs to change the electric dipole moment of the molecule [180].

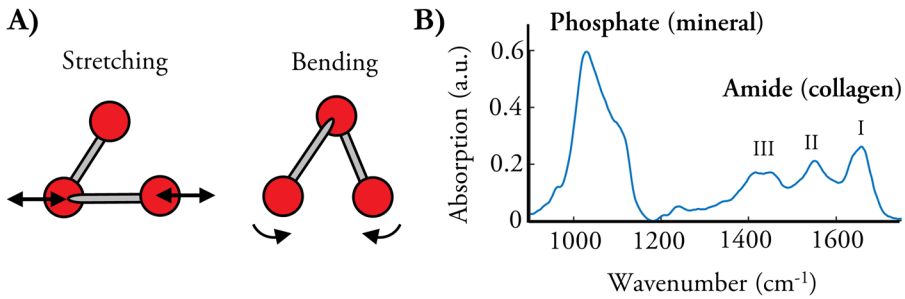

Figure 3.9. Principles of Fourier-transform infrared spectroscopy. A) When infrared radiation is absorbed by molecular bonds they will vibrate either by stretching or bending of the bonds. B) Characteristic FTIR spectrum of embryonic bone, showing the phosphate and amide I peaks.

IR measurements are typically performed in transmission mode, in which a thin slice of the sample is illuminated by a broad spectrum of IR wavelengths and the levels of the transmitted IR radiation at each wavelength is recorded. Fourier transform of this spectrum can be conducted to obtain the absorption spectrum, referred to as Fourier-transform infrared spectroscopy (FTIR). Usually, the wavelengths are converted into wavenumber $\bar{\nu}$, defined as:

$$\bar{\nu} = \frac{1}{\lambda} = \frac{\nu}{c} \tag{3.9}$$

where ν is the frequency and c the speed of light in vacuum. The recorded transmittance $T(\bar{\nu})$ is defined as the ratio between the transmitted $I(\bar{\nu})$ and incoming $I_0(\bar{\nu})$ IR intensity:

$$T(\bar{\nu}) = \frac{I(\bar{\nu})}{I_0(\bar{\nu})} = e^{-\sigma(\bar{\nu})cl} \tag{3.10}$$

where σ is the molecular absorption coefficient, c the concentration of the absorbing molecule and l the thickness of the material (length of the optical path). The absorbance $A(\bar{\nu})$ of the molecule is related to the transmittance through Beer-Lambert's law:

$$A(\bar{\nu}) = \ln\left(\frac{1}{T(\bar{\nu})}\right) = \sigma(\bar{\nu})cl \tag{3.11}$$

In bone, the main molecular bonds which can be probed with IR are the phosphate and amide I bonds, which gives rise to absorbance peaks at 1200-900 and 120-1585 cm^{-1} [181], respectively (Figure 3.9-B). The phosphate bonds are present

within the HA crystals and thus indicate the mineral content of the tissue, and the amide I bonds are present within the collagen molecules, thus indicating the amount of collagen present. The compositional levels of these molecules are evaluated from the areas under their corresponding peaks. Sub-peaks are often also fitted, or their intensity extracted, to gain more descriptive information about these molecules, such as the ratio of collagen cross-links (1660:1690 cm^{-1}), which is related to collagen maturity, or acid-phosphate substitution into the HA crystal (1127:1096 cm^{1}), which is an indication of new bone formation [181]. The collagen content, maturity and ratio of mineral to matrix has been shown to change with development and aging as well as vary depending on anatomic location [182–185].

3.3.7 Polarized light microscopy

Polarized light microscopy (PLM) can be used to evaluate the microscale orientation of materials. Birefringence is an optical property of materials which are characterized by a difference in refractive indices in orthogonal directions. When polarized light propagates orthogonal to the plane of those directions, the transmitted light will be split into two rays with different refraction angles (Figure 3.10). These two rays are referred to as the *ordinary* and *extraordinary* ray, respectively. The extraordinary ray depends on the propagation direction and will take a longer path and thus travel slower than the ordinary ray. When the polarization state of the incoming light is parallel to the main optical direction of the anisotropic structures, the ordinary ray will reach its highest velocity.

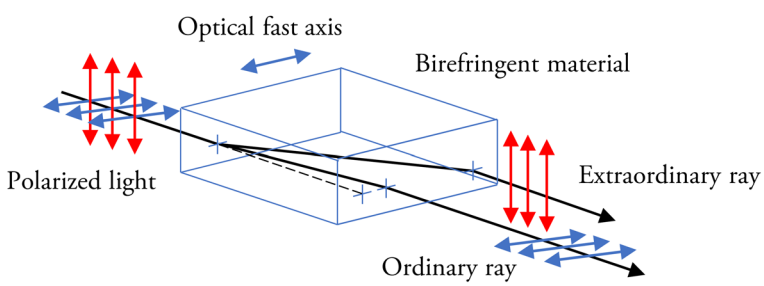

Figure 3.10. Principle of PLM. When polarized light enters an optically anisotropic material it will be split into two rays. The polarization state of the ordinary ray is paralell to the optical fast axis of the material and will propagate faster through the material than the extraordinary ray, which has an orthogonal polarization state to to the optical fast axis.

The birefringence B of a material, is described as the difference between the extraordinary (n_e) and ordinary (n_o) refractive indices:

$$B = |n_e - n_o| \tag{3.12}$$

The retardation Γ of the extraordinary ray in comparison to the ordinary ray as a result of the anisotropy of the material can be estimated by also considering the thickness t of the sample:

$$\Gamma = t \cdot |n_e - n_o| \tag{3.13}$$

The retardance (related to structural alignment) and angle of the optical fast axis (related to structural orientation), can be obtained from the changes in polarization state as the light passes through the sample. The Stokes $\vec{S}$ vector describes the polarization state of the light through four parameters; S_0 describes the total intensity of the light, S_1 describes degree of light being horizontally/vertically polarized, S_2 describes the degree of polarization in ±45°, and S_3 describes the degree of right/left-handed circular polarization [186]. As the polarized light propagates through a birefringent material, the Stokes vector $\vec{S}$ will change. Thus, as the light passes through a series of optical elements the outcoming polarization state $\overrightarrow{S'}$ can be related to the initial polarization state $\vec{S}$ with the Mueller matrix [186,187] of each element $M_1, M_2, \dots, M_n$ through:

$$\overrightarrow{S'} = M_n\left(\dots\left(M_2\left(M_1\vec{S}\right)\right)\dots\right) = M_n \dots M_2 M_1 \vec{S} \tag{3.14}$$

By combining different polarizers and photoelastic modulators, the four Stokes parameters can be estimated from the Mueller matrices to retrieve the change in polarization angle and phase difference between the ordinary and extraordinary rays. The appropriate Mueller matrices for the optical elements can in turn be used to estimate the retardance Γ and angle of the optical fast axis (θ):

$$\Gamma = \tan^{-1}\sqrt{(M_{24}/M_{44})^2 + (M_{34}/M_{44})^2} \tag{3.15}$$

$$\theta = \frac{1}{2}\tan^{-1}(M_{24}/M_{44}) \tag{3.16}$$

In bone, the main anisotropic structures exhibiting birefringence are the mineralized collagen fibers [188]. PLM has been widely used to investigate the orientation of collagen fibers in bone, to for example evaluate the effects of growth, maturation and loading patterns [189–191].

3.3.8 Mechanical testing

Mechanical testing can be applied to characterize the mechanical properties of materials. During mechanical testing, the material is subjected to a load or displacement and the force-displacement response of the material is recorded over time. Force (F) and displacement (d) are extrinsic parameters which depend on the shape and size of the material. By normalizing the force and displacement into stress (σ) and strain (ε) by the shape and size of the material, intrinsic material parameters can also be obtained [192–194]. If one assumes a homogenous stress and strain distribution across the material, their conversion from force and displacement can be obtained by:

$$\sigma = \frac{F}{A} \tag{3.17}$$

$$\varepsilon = \frac{\Delta l}{L_0} \tag{3.18}$$

where A is the cross-sectional area of the material, Δl the deformation change and L_0 is the initial length. Typical mechanical properties which can be estimated from the resulting force-displacement or stress-strain curves are:

- Stiffness (N/mm) or Young's modulus (MPa): slope of the linear region
- Yield force (N) or stress (MPa): transition between elastic (recoverable) and plastic (permanent) deformation
- Maximum force (N) or stress (MPa): at failure

Both bones and tendons are viscoelastic; their mechanical behaviour is time dependent, and it depend on the rate of which the load is applied, as well as their hydration state. As a result, both tissues exhibit non-linear stress-strain behaviours due to their complex internal organization (Figure 3.11) [1]. Their viscoelastic behaviour is characterized by creep, stress relaxation and an increased stiffness with increased strain rate [1,18]. The viscoelasticity of tendons is more pronounced than for bone, and tendons for example display a more notable hysteresis, i.e. remaining deformation and energy loss following load removal.

As the mechanical response of the full tissue is highly dependent on the characteristics of all length scales as well as how they relate to each other, mechanical testing is often performed on several length scales [151–154,156,158,195–200]. Simultaneous characterization of mechanical behaviour on several length scales can be achieved by combining mechanical testing with the above-mentioned imaging techniques. Performing mechanical testing while imaging is referred to as an *in situ* experiment.

Due to the complex combination of different loading of bones *in vivo*, mechanical testing of bone is commonly conducted through three-point bending, compression or shear tests [193]. Tendons on the other hand, are primarily exposed to tensile loads and thus mostly tensile testing is applied [201].

Tendon deformation mechanisms

Due to their crimped collagen fibers at rest, the initial deformation of tendons involves the straightening of fibers. Thus, the tendon will initially deform without carrying much load. But eventually, as more and more fibers straighten, they will contribute to carrying the load and the force will increase exponentially. This region is referred to as the toe region (Figure 3.11) [1,18]. As all fibers are straightened and aligned, the tendon enters a linear (elastic) region in which all structural units stretch. Within this region the tendon can still return to its initial length if the load is removed. The accumulated stretching of collagen molecules, fibrils, fibers, fascicles and sub-tendons contribute to the total elongation of the tendon. Additionally, these sub-units can slide relative each-other, further contributing to macroscopic elongation. If the tendon continues to stretch, irreversible microscopic tearing of the collagen fibers will eventually occur (plastic region) and ultimately result in macroscopic failure.

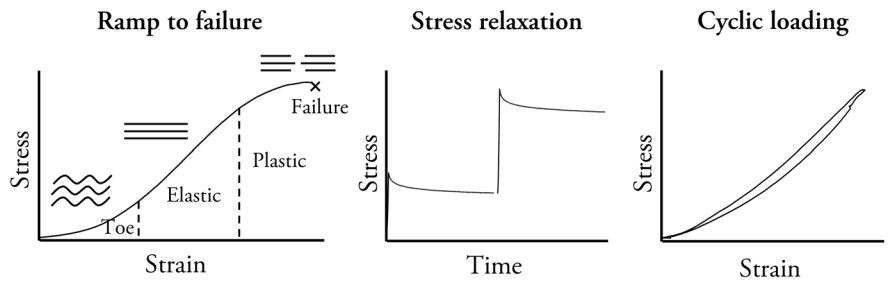

Figure 3.11. Mechanical behavior of tendons. Uncrimping of fibers at low loads results in an exponentially increasing toe region, then the straightened fibers stretch linearly resulting in a linear region. At higher loads the fibers will start to break, resulting in an exponentially decaying region, which ultimately accumulates to tissue failure. Other viscoelastic characteristics of tendons are their ability to exhibit stress relaxation and hysteresis during cyclic loading.

The strain transfer from the tissue scale down to the molecular level is highly complex and evidence points towards strain being partitioned not only between structural sub-units, but within the matrix in-between them as well [202,203]. The interfascicular matrix has been shown to be able to carry 40% of fascicle failure loads [204] and to facilitate the high strain characteristics of tendons, through an increased sliding capacity [203–207].

4 Methods

This chapter outlines the material and methods used in each study of this thesis. First, the animal model used in the specific section is described. This is followed by the details of each tissue characterization technique together with the study-specific details and their corresponding data analysis.

4.1 Mechanobiology of long bone mineralization (Objective 1)

4.1.1 Embryonic mouse model

To characterize the mechanobiology of long bone development in Papers I-II, embryonic mice (C57BL/6) with (C) and without (M) skeletal muscle ($Pax3^{Spd-/-}$, Splotch-delayed) were used (Table 4.1-2). Forelimbs were harvested from five development stages (Theiler Stages, TS) based on the Theiler morphological criteria [208]. Stages from first sign of mineralization (TS23, approximately embryonic day 14.5) to shortly before birth (TS27, approximately embryonic day 18.5) were included.

The animal experiments were conducted by co-authors at Imperial college of London, UK. The experimental protocol adhered to the ARRIVE guidelines and was conducted in accordance with European legislation (Directive 2010/63/EU) under project license number P39D18B9C. The dissected forelimbs were fixed and transported to Lund, Sweden, where they were embedded in either hard plastic or paraffin depending on the characterization technique (Figure 4.1). The experimental details for each individual synchrotron technique are provided in Table 4.3.

Table 4.1. Overview of samples assessed in Paper I with each experimental technique. Only control embryonic mice with skeletal muscle were used (C).

Experimental technique	TS23	TS24	TS25	TS26	TS27	Adult
Group	C	C	C	C	C	C
µCT	4	6	3	-	4	-
µSAXS/WAXS/XRF	-	1	-	-	1	-
nXRF	1	1	1	1	-	1
FTIR	4	4	4	5	4	1

Table 4.2. Overview of samples assessed in Paper II with each experimental technique. Both embryonic mice with (C) and without (M) skeletal muscle were used.

Experimental technique	TS23		TS24		TS26		TS27	
Group	C	M	C	M	C	M	C	M
SASTT	1	1	1	1	1	1	1	1
µSAXS/WAXS/XRF	-	-	1	1	-	-	1	1
nXRF	-	-	-	-	-	-	1	1
FTIR/PLM	4	4	4	4	5	4	4	4

Table 4.3. Overview of synchrotron experimental details for Papers I-II. Phase contrast µCT (PC- µCT) provided visualization of the bone microstructure, SAXS/WAXS and SASTT information of nanostructural organization of the mineral particles in 2D and 3D respectively, and XRF elemental information.

Experiment	PC-µCT	µSAXS/WAXS	SASTT	µXRF	nXRF	
Synchrotron facility	DLS	ESRF	PSI	ESRF	MAX IV	
Beamline	I13-2	ID13	cSAXS	ID13	NanoMAX	
Paper	I	I-II	II	I-II	I	II
Beam energy (keV)	25	13	11.2	13	14	12
Exposure time (ms)	70	50	30	50	120	80
Sample-detector distance (mm)	190	93	2e3	20	12	25
Beam size (µm)	2100x1800 / 4200x3500	2x2	25x12	2x2	80x80	
Spatial resolution (µm)	0.81 / 1.625	2	25	2	0.2	0.1

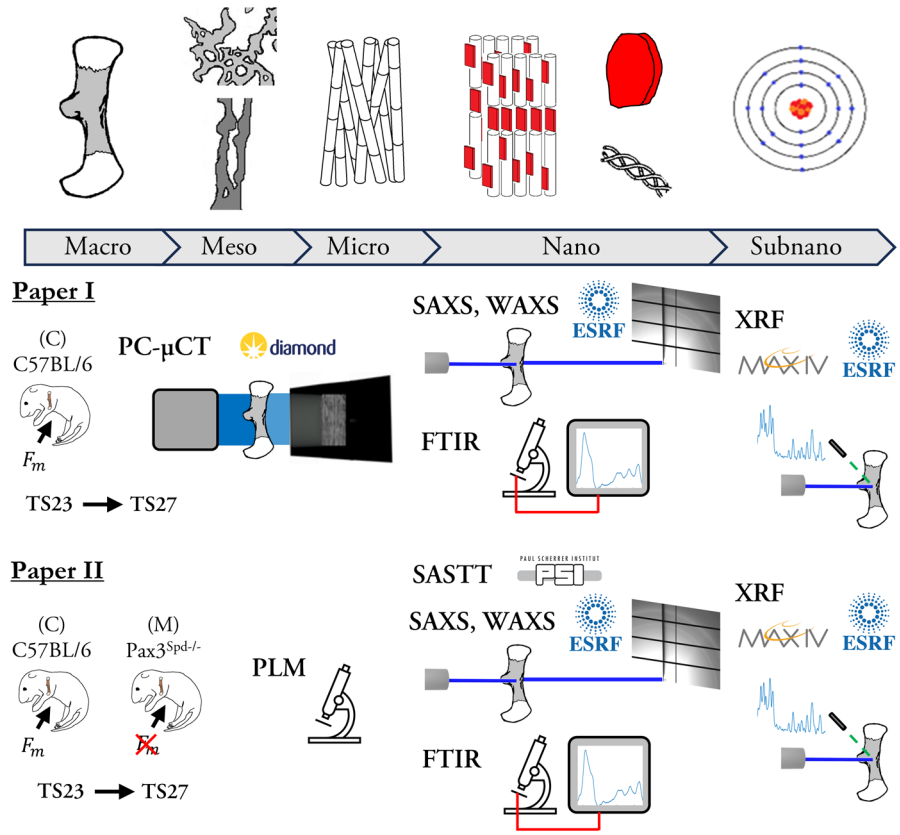

Figure 4.1. Overview of embryonic bone studies (Paper I and II). The structure and composition of the mineral and collagen components of embryonic bones with (C) and without (M) muscle (F_m) were assessed across several length scales using a range of synchrotron and lab-based characterization techniques.

4.1.2 Phase-contrast microtomography

To characterize the geometry and microscale organization of the mineralized region of developing embryonic bones in Papers I, phase-contrast µCT was performed on forelimbs from development stages at start of mineralization to shortly before birth (Table 4.1). Measurements were carried out at the I13-2 beamline at the Diamond Light Source (DLS, United Kingdom) (Table 4.3). Projections were acquired using a PCO.edge 5.5 camera link (PCO AG, Germany) detector (sCMOS sensor) at equally spaced angles over 180° continuous rotation. 4x and 2x objectives were chosen, resulting in field of views (FOVs) of 2.1x1.8 mm^2 for TS23-TS25 and 4.2x3.5 mm^2 for TS27.

The acquired 2D projections were flat-field corrected, ring artefacts were removed [209], and volumes reconstructed using standard Paganin filtered back projection [133]. The mineralized regions of the reconstructed tomograms were segmented by contrast threshold [12]. The size, shape, cross-sections and distribution of the mineralized rudiments were evaluated qualitatively.

4.1.3 X-ray scattering

To characterize the mineral particles of developing embryonic bones in Papers I and II, simultaneous micrometre (μm) resolved SAXS and WAXS experiments were conducted on 3 μm sections of forelimbs from one early and one late development stage (Table 4.1). Measurements were carried out at the ID13 beamline at the European Synchrotron Radiation Facility (ESRF, France) (Table 4.3). The humeri were scanned in 2D to obtain FOVs of approximately 1x0.5 mm^2. The scattering patterns per scanned point were acquired using an Eiger 4M detector (Dectris, Switzerland). From the per point recorded 2D scattering patterns, the predominant orientation and degree of orientation of the mineral particles were estimated [210], as well as their thickness, length and width of coherent blocks in the [002] and [310] directions, respectively [140,141,146].

To further characterize the mineral particles of developing embryonic bones in 3D in Paper II, SASTT measurements were conducted on forelimbs from development stages at start of mineralization to shortly before birth (Table 4.2). Measurements were carried out at the cSAXS beamline, Swiss Light Source (SLS) at the Paul Scherrer Institute (PSI, Switzerland) (Table 4.3). The samples were aligned to their center of rotation and mapped in 2D repeatedly at equally spaced rotation and tilt angles between 0 and 360° and 0 and 45°, respectively. The 2D maps were obtained to include the entire humerus when possible, but at least one growth plate and the most mineralized region, resulting in FOVs of approximately 1x1 mm^2. The scattering patterns per scanned point were acquired using a Pilatus 2M detector [211]. The acquired 2D maps were transmission corrected, aligned and the reciprocal space map in each voxel reconstructed using the SIGTT method [167] to estimate the predominant orientation of the mineral particles and their relative anisotropy. The isotropic part of the ZHTT method [162,212,213] was applied to estimate the average mineral particle thickness [139–141,146].

4.1.4 X-ray fluorescence

To characterize the elemental composition of developing embryonic bones in Papers I and II, micrometre resolved XRF experiments were conducted simultaneously as the combined SAXS and WAXS experiments described in Section 4.1.3. An XRF spectrum was recorded at each scanned point using a single

element Vortex EM detector (Hitachi High-Technologies Corp, US) at an angle of approximately 30° to the sample.

Additionally, nanometre (nm) resolved XRF measurements were conducted at the NanoMAX beamline at MAX IV Laboratory (Sweden) (Table 4.1-3). In Paper I, 3 µm sections were scanned in 2D and XRF spectra were recorded at each scanned point using a XR-100SDD detector (Amptek Inc., US) at an angle of approximately 20° with respect to the sample. The scans were conducted to obtain FOVs including the active mineralization front, approximately the size of 40x150 μm^2, as well as more mineralized regions in e.g. the bone collar. In Paper II, 1 µm sections of the same forelimbs as imaged with micrometre resolved XRF from development stage TS27 were mapped in 2D. XRF spectra were recorded at each scanned point using a single-element silicon drift detector (RaySpec, UK) coupled to an Xpress 3 pulse processor (Quantum Detectors, UK) at an angle of approximately 15° with respect to the sample. The scans were conducted to obtain FOVs including the active mineralization front, approximately the size of 40x200 μm^2, as well as a more mineralized regions such as the bone collar and remodeling regions deeper into the mineralized region.

The spectra acquired per point from both micro- and nanometre resolved measurements were fitted [214] and elemental spatial distribution maps were further analyzed. Specifically, Ca and Zn were further evaluated in Paper I-II, as well Fe in Paper II. In the nanometre resolved XRF, the elemental distributions were calibrated using a thin film standard (SRM 613, NIST, US in Paper I and RF-C0, AXO Dresden, Germany in Paper II).

4.1.5 Fourier transform infrared spectroscopy

To characterize the molecular composition of developing embryonic bones in Papers I and II, FTIR measurements were conducted. 3 µm sections of forelimbs from development stages at start of mineralization to shortly before birth (Table 4.1-2) were mapped in transmission mode using a Bruker Hyperion 3000 IR microscope (Bruker Corp, US) with a 64 x 64 focal plane array detector. Areas across the growth plates and in the most mineralized regions were scanned with 64 repeated scans, a spatial resolution of 2.3 µm and spectral resolution of 4 cm^{-1}. The acquired spectra spanned wavelengths between 2000 cm^{-1} to 900 cm^{-1}.

After background and baseline correction, mineral content was estimated from the area under the phosphate band (1200-900 cm^{-1}) and collagen content from the amide I band (1725-1575 cm^{-1}) [215,216]. Mineral to matrix ratio was estimated as the ratio between the mineral and collagen content. In Paper I, the collagen maturity and the acid phosphate substitution were estimated from the ratio of the sub-bands 1660:1690 cm^{-1} and1127:1096 cm^{-1}, respectively.

4.1.6 Polarized light microscopy

To characterize the collagen orientaton of developing embryonic bones in Paper II, the same samples as prepared for FTIR were measured with PLM. Measurements were conducted using the imaging system Exicor Birefringence MicroImager™ (Hinds Instruments Inc., US). The entire humeri were measured using a 10X objective, providing a FOV of 1x1 mm^2 and a spatial resolution of 0.5 µm. A stroboscopic light emitting diode of wavelength 475 nm (blue) was used to calculate the Mueller matrix components in order to quantify the retardance and angle of the optical fast axis [217,218].

4.1.7 Statistical analysis

In all studies, mean, standard deviations (SD) and 95% confidence intervals (CI) were computed.

In Paper I, linear mixed effects analysis was used to test for statistical significance in FTIR parameters with development stage, while considering the high number of measurement points per sample. The data from SAXS, WAXS and XRF were only evaluated qualitatively due to their low sample numbers.

In Paper II, two-way analysis of variance (ANOVA) was used to test the effect of *in vivo* loading scenario (muscle-less limb vs control) and development stage (TS23-TS27) on the FTIR and PLM parameters. Post-hoc analysis was conducted when appropriate by a multiple comparison test. The data from SASTT, SAXS, WAXS and XRF were only evaluated qualitatively due to their low sample numbers.

4.2 Mechanobiology of tendons (Objective 2 & 3)

4.2.1 Rat Achilles tendon model

To characterize the mechanobiology of both intact and healing Achilles tendons in Papers III-VI, female Sprague-Dawley rats (specific pathogen free, age 10-12 weeks from Janvier, Le Genest-Saint-Isle, France) were used (Table 4.4-7). In Paper III and IV, intact Achilles tendons were harvested after 4 weeks and in Paper VI, healing tendons were harvested after 1, 2 or 3 weeks after transection. Intact or healing Achilles tendons were harvested together with the calcaneal bone and the gastrocnemius soleus muscle complex in all studies. In Paper IV and V, the rats were randomly divided into two groups subjected to different *in vivo* loading scenarios: 1) full loading (FL) through free cage activity or 2) unloading (UL) through Botox injections in the calf muscles in combination with joint fixation

using a steel-orthosis [32]. In Paper VI, the rats were randomly divided into three groups: 1) FL, 2) reduced loading (RL) through Botox injections in the calf muscles or 3) UL.

The animal experiments were conducted by other co-authors at Linköping University, Sweden. All experimental protocols adhered to the ARRIVE and institutional guidelines for care and treatment of laboratory animals and were approved by the Regional Ethics Committee for animal experiments in Linköping, Sweden (Jordbruksverket, ID1424). The dissected tendons were wrapped in gauze soaked with phosphate buffered saline (PBS) solution, frozen (-20 °C) and transported to Lund, Sweden, where they were stored frozen until measurements or further sample preparation, depending on the characterization technique (Figure 4.2-3). The experimental details for each individual synchrotron technique are provided in Table 4.8.

Table 4.4. Overview of samples assessed in Paper III with each loading scheme in combination with SAXS. Only 4 weeks fully loaded intact Achilles tendons were used.

SAXS + *in situ* mechanical test	Number of samples
Ramp to failure	5
Cyclic loading	4
Stress relaxation	6

Table 4.5. Overview of samples assessed in Paper IV with each experimental technique. Both 4 weeks fully (FL) and unloaded (UL) intact Achilles tendons were used.

Experimental technique	Number of samples	
Group	FL	UL
Phase-contrast µCT	7	7
SAXS + *in situ* mechanical test	10	8
Ex-situ mechanical test	9	10
Histology	5	6

Table 4.6. Overview of samples assessed in Paper V with each experimental technique. Both fully (FL) and unloaded (UL) healing Achilles tendons were used, as well as intact tendons for reference and radiation damage test. Phase-contrast μCT and SASTT were performed on the same samples, as indicated by *.

Experimental technique	FL			UL			Intact
Weeks of healing	1w	2w	3w	1w	2w	3w	-
Phase-contrast μCT*	1	-	1	1	-	1	-
SASTT*	1	-	1	1	-	1	2
2D SAXS	4	4	4	4	4	4	-

Table 4.7. Overview of samples assessed in Paper VI with SAXS in combination with *in situ* stress relaxation followed by ramp to failure. 1, 2 and 3 weeks fully (FL), reduced (RL) and unloaded (UL) healing Achilles tendons were used. 1 week reduced loaded tendons were only tested mechanically in the lab, and not in combination with SAXS (*).

Group	FL	RL	UL
1, 2, 3 weeks	4	4*	4

Table 4.8. Overview of synchrotron experimental details for Papers III-VI. SAXS in combination with *in situ* loading provided evaluation of collagen fibril response to tissue loads, SASTT and SAXS information on the structural organization of collagen fibrils in 3D and 2D respectively, and phase contrast μCT (PC- μCT) visualization of the microscale organization of collagen fibers.

Experiment	*In situ* SAXS		SASTT	2D SAXS	PC-μCT
Synchrotron facility	PSI		PSI	PSI	PSI
Beamline	cSAXS		cSAXS	cSAXS	TOMCAT
Paper	III-IV	VI	V	V	IV-V
Beam energy (keV)	12.4		12.4	12.4	15
Exposure time (ms)	50	30	30	30	33
Sample-detector distance (mm)	7e3		7e3	7e3	150
Beam size (μm)	150x150		150x150	50x40	4200x3500
Spatial resolution (μm)	150		150	50	1.63

4.2.2 *In situ* SAXS to study collagen mechanics

To characterize the mechanical response of collagen fibrils in Papers III, IV and VI, SAXS measurements simultaneously as *in situ* loading were conducted (Table 4.4-5,7). Thawed intact or healing Achilles tendons were mounted in a custom-built uniaxial tensile device [195,219], which was placed in the beam at the cSAXS beamline, Swiss Light Source (SLS) at the Paul Scherrer Institute (PSI, Switzerland) (Table 4.8) (Figure 4.2-A). The scattering patterns were acquired using a Pilatus 2M detector [211]. In Papers III and IV, one spot was repeatedly scanned in the middle of the tendon as macroscopic tensile loads were applied. In Paper III, the tendons were loaded in either ramp to failure, cyclic loading, or stress relaxation configurations with a displacement rate of 5 mm/min. In Paper IV, ramp to failure and stress relaxation were performed. In Paper VI, a map of three horizontal lines across the tendon was acquired repeatedly during stress relaxation followed by one spot in the middle of the tendon during ramp to failure. The tensile loading was displacement controlled and all loading protocols were applied using a displacement rate of 5 mm/min. Force and displacement data were normalized by sample dimensions into stress and strain. From the retrieved tissue and fibril curves during ramp to failure, values at tissue yield, maximum d-spacing and maximum stress were extracted. Additionally, tissue stiffness was calculated. From cyclic loading curves, hysteresis, stiffness and values at maximum and end of each cycle were retrieved. From the stress relaxation curves, stiffness, maximum stress, relaxation ratios and fast relaxation times were estimated.

From the per point recorded 2D scattering patterns, d-spacing or fibril strain, and fibril strain heterogeneity were estimated in all Papers III, IV and VI [22,103]. In Paper III, changes in the overlap length were estimated [103,152,154,220]. In Papers III and IV, intrafibrillar disorder [221] and predominant orientation were also estimated, and in Paper VI, the collagen amount was also estimated.

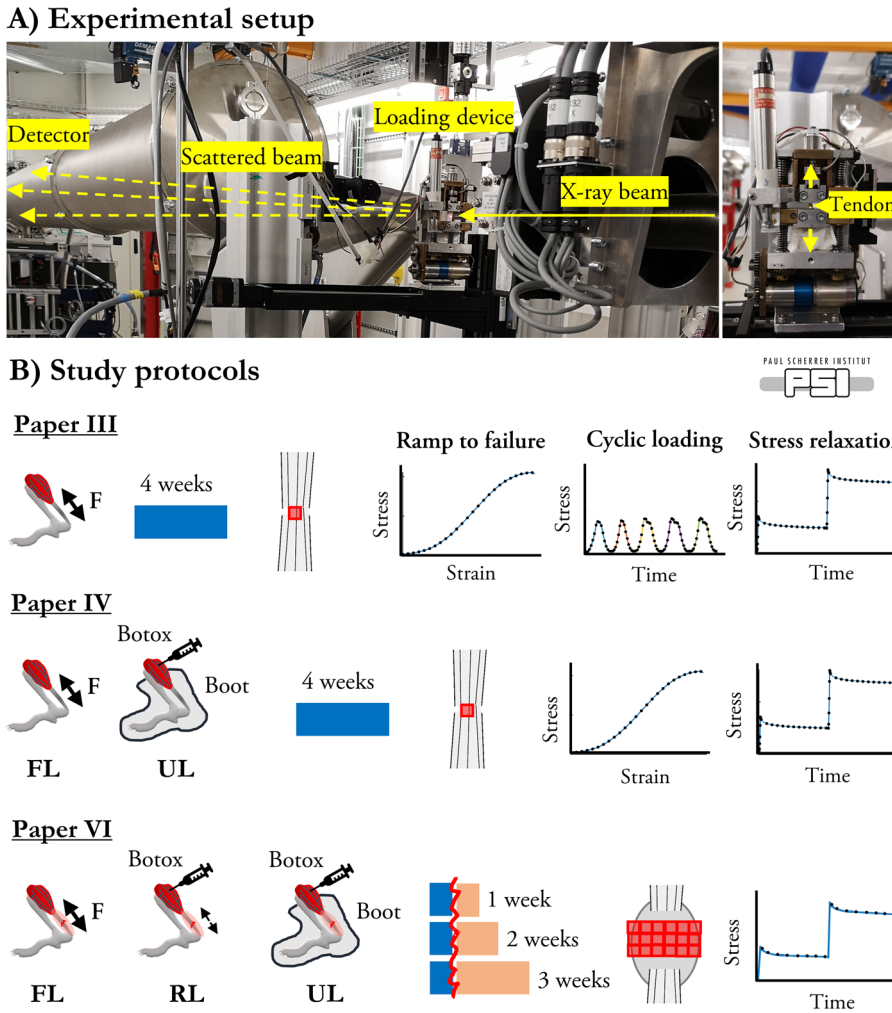

Figure 4.2. Overview of *in situ* studies on intact and healing tendons (Paper III, IV and VI). A) SAXS measurements were acquired simultaenously as mechanical testing of fully loaded (FL), reduced loaded (RL) or unloaded (UL) tendons. B) Different *in vivo* environments, scan areas and mechanical tests were evaluated in the different papers.

4.2.3 SASTT and scanning SAXS to study tendon healing

To characterize the structure of collagen fibrils in 3D in Paper V, SASTT measurements were conducted on fixed healing tendons (Table 4.6). Measurements were carried out at the cSAXS beamline (SLS, PSI, Switzerland) (Table 4.8) (Figure 4.3). The samples were aligned to their center of rotation and mapped in 2D repeatedly at equally spaced rotation and tilt angles between 0 and 360° and 0 and 45°, respectively. Scans with FOVs of approximately 6x7.5 mm^2 were acquired. The scattering patterns per scanned point were acquired using a Pilatus 2M detector [211]. To provide an intact reference as well as to evaluate the effect of radiation damage during the SASTT measurements, two intact Achilles tendons from contralateral hind limbs were prepared and measured in the same manner. The acquired 2D maps were corrected by simulated transmission, aligned and the reciprocal space map in each voxel reconstructed using the SIGTT method [167] to estimate the predominant orientation of the collagen fibrils and their relative anisotropy. The ZHTT method [162,212,213] was applied to estimate the average fibril d-spacing, amount and delamination [139–141,146].

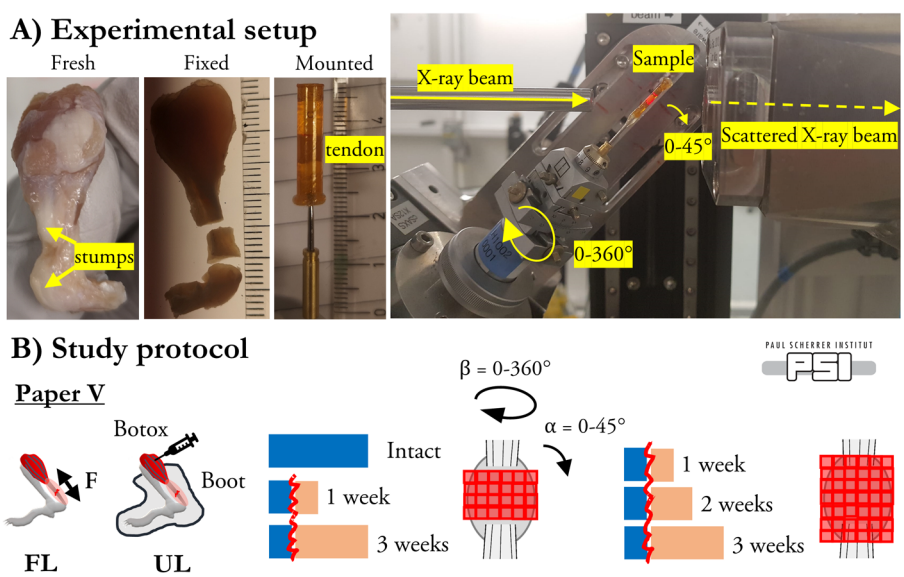

Figure 4.3. Overview of SASTT study on healing tendons (Paper V). A) Thawed healing tendons subjected to either full loading (FL) or unloading (UL) were fixed, their central callus cut out and mounted. SASTT measurements were acquired at the cSAXS beamline, PSI. B) SASTT measurements were performed on a limited sample set and 2D SAXS on an extended sample set.

Additionally, thawed unfixed tendons were scanned with 2D SAXS at the cSAXS beamline (SLS, PSI, Switzerland) (Table 4.8). The 2D maps were obtained with FOVs of 5x10 mm^2 to include most of the callus and the two stumps. From the per point recorded 2D scattering patterns, the predominant orientation and degree of orientation of the collagen fibrils were estimated [210], as well as their d-spacing, amount and delamination.

4.2.4 Phase-contrast microtomography

To characterize microstructural organization of the collagen fibers in Papers IV and V, phase-contrast μCT was performed on intact and healing tendons, respectively. Measurements were carried out at the TOMCAT beamline (SLS, PSI, Switzerland) (Table 4.8). The projections were acquired using a high numerical aperture microscope setup, coupled to a 150 μm LuAG:Ce scintillator screen at equally spaced angles over 180° continuous rotation. 4x magnification was chosen, resulting in FOVs of 4.2x3.5 mm^2, and 2-8 scans were acquired to cover the entire tendons.

The acquired 2D projections were flat-field corrected, and volumes reconstructed using standard Paganin filtered back projection [133] and a Fourier based regridding algorithm [222]. The collagen fibers were segmented by the Otsu's method [223] and their orientation in selected sub-volumes was determined in 3D by performing a structure tensor analysis [224,225].

4.2.5 *Ex situ* mechanical testing

Thawed tendons were mounted in an Instron 8511 load frame (Instron, US) controlled by MTS TestStar II software (MTS Systems, US). Force was recorded using a SMT1-250N load cell (Interface, US). The tendons were pre-loaded to 1N and then exposed to three consecutive loading protocols: 1) cyclic loading followed by a period of rest, 2) stress relaxation and 3) ramp to failure. Tendons were kept hydrated during the experiments by drops of PBS at 2-minute intervals. The tensile loading was displacement controlled and performed at 0.1 mm/s during cyclic loading and 1 mm/s during stress relaxation steps and ramp to failure. Force and displacement data were collected and normalized by sample dimensions into stress and strain.

From cyclic loading stress-strain curves, toe strain, stiffness and hysteresis were extracted. Stiffness, maximum stress, stress relaxation ratio and fast relaxation time were retrieved from the stress relaxation curves. From ramp to failure, stiffness, maximum stress and strain were estimated.

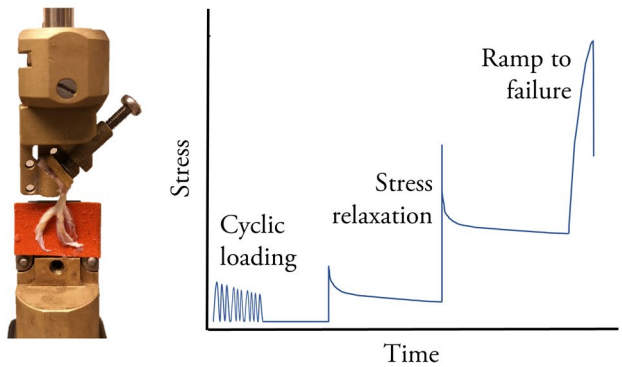

Figure 4.4. Overview of *ex-situ* testing. The tendons were clamped in a lab-based loading device with custom-made clamps and loaded in cyclic loading, followed by rest, then two stress relaxation steps and ultimately ramp to failure.

4.2.6 Statistical analysis

In all studies, mean, SD and 95% CI were computed.

In Paper III, the data was tested for normal distribution by the Shapiro-Wilks test. Since the data was not normally distributed, non-parametric statistical tests were used. The Kruskal-Wallis test was used to estimate the statistical significance between start of loading, maximum d-spacing and maximum force in both the tissue and fibril parameters from the ramp to failure data. The Friedmans test was used to test statistical significance in both tissue and fibril parameters across the cyclic loading.

In Paper IV, the data was tested for normal distribution by the Shapiro-Wilks test. Since the data was not normally distributed, non-parametric statistical tests were used. The Mann-Whitney U-test (unpaired) was used to estimate the statistical significance in all investigated properties between *in vivo* loading scenario (FL vs UL). The Wilcoxon signed rank test (paired) was used to estimate statistical significance between different locations within the same tendon (MG, LG and SOL).

In Paper V, two-way ANOVA was used to test the effect of *in vivo* loading scenario (FL vs UL) and healing time (1, 2, 3 weeks) on the fibril parameters from 2D SAXS. Multiple comparison post-hoc test was conducted when appropriate. The data from phase contrast μCT and SASTT were only evaluated qualitatively due to their low sample numbers.

In Paper VI, further statistical testing was omitted due to the small sample groups.

5 Results

In this chapter, the main results and findings from each individual study are presented. Each section starts with a short summary of the approach in the corresponding studies, followed by a summary of the main results.

5.1 Mechanobiology of long bone mineralization (Objective 1)

Humeri from "muscle-less" embryonic mice and their healthy littermates at development stages from start of mineralization to shortly before birth were investigated using a combination of synchrotron- and lab-based techniques. Phase contrast μCT, SAXS, WAXS, SASTT and PLM were used to study the micro- and nanoscale structure, and FTIR and XRF were used to study the molecular and elemental composition.

During normal development, rapid mineralization of the humeri occurred, with roughly 400% increase in length of the rudiment between TS23 and TS27 (Figure 5.1-A). Similar cortical concentrations of Ca as in the adult reference were reached at TS26. At all stages, Zn was found at the mineralization front of the growth plate, in roughly 200% higher concentrations than further into mineralization (Figure 5.1-C). At the later stages, Zn was also found outlining the cortex and internal structures further into mineralization. The newly mineralized tissue was also characterized by thicker, longer and narrower mineral particles compared to the more mature tissue such as the bone collar (Figure 5.1-D). The mineral particles were aligned along the long axis of the bones already at TS24 and increased in degree of orientation between TS24 and TS27, with the cortical mineral particles of the bone collar generally having a higher degree of orientation compared to those of the internal structures at both stages.

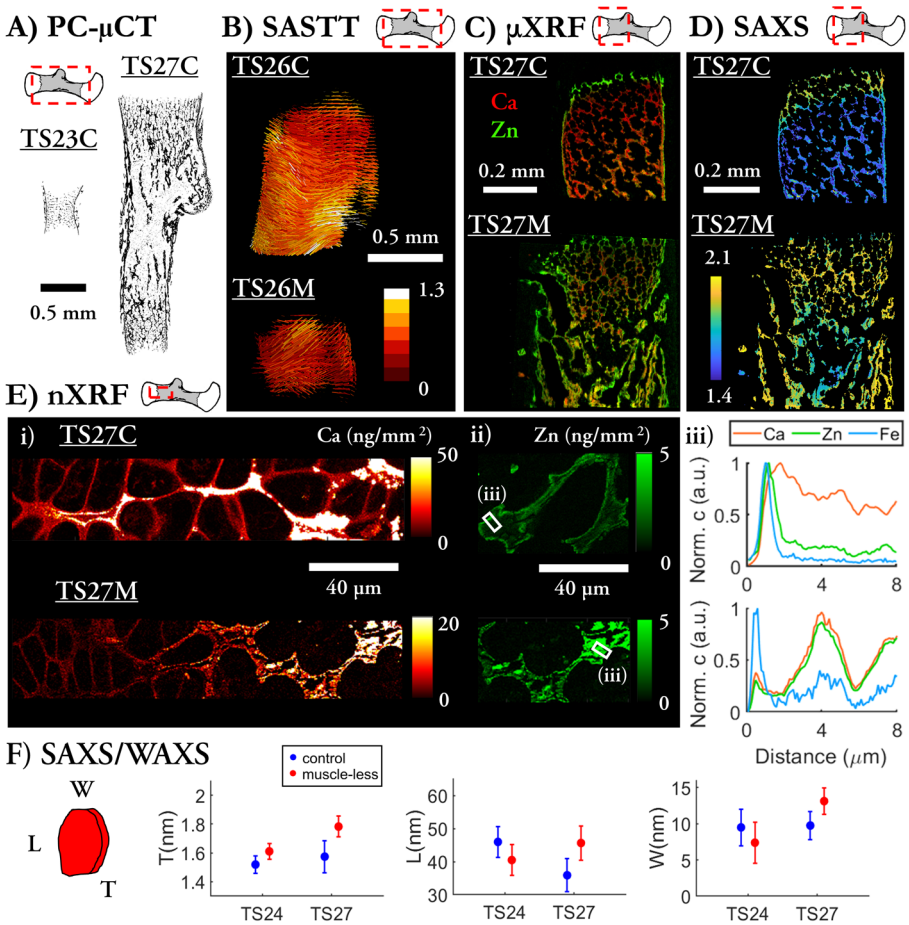

Figure 5.1. Main results from Paper I and II. A) Evolution in size and geometry of the healthy (C) humeri during embryonic development. B) Size, geometry and nanoscale orientation of healthy (C) and muscle-less (M) humeri at TS26. C) Distribution of Ca (red) and Zn (green) at TS27. D) Distribution of mineral particle thickness at TS27. E) Concentration of Ca and Zn at TS27, showing the minerlization front (i), 200 µm into mineralization (ii) and normalized concentration profile across an edge of a mineralized structure ~200 µm into mineralization (iii). F) Evolution of mineral particle dimensions within the bone collar between TS24 and TS27.

When skeletal muscles were absent, the development was delayed, with humeri being smaller and deformed compared to their littermate controls (Figure 5.1-B). A decreased Ca content was also observed (Figure 5.1-E). At TS27 however, the size of the humerus was similar to that of the control. Instead of being localized to

the mineralization front and outlining the internal structures, the muscle-less bone at TS27 had a more widespread, homogenous distribution of high levels of Zn (Figure 5.1-C). The Zn in the muscle-less bones was also co-localized with Ca all across the rudiment instead of being restricted to edges of mineralized structures as in littermate controls (Figure 5.1-C,E). As opposed to normal development, absence of skeletal muscles lead to a continuous increase in mineral particle size, with them at TS27 being larger than those of their littermate controls (Figure 5.1-D,E).

5.2 Mechanobiology of intact tendons (Objective 2)

A combination of synchrotron- and lab-based techniques were used to investigate the effect of 4 weeks of loading or unloading on intact rat Achilles tendons. Phase contrast µCT and SAXS were used to study the micro- and nanoscale structure, *in situ* and *ex situ* mechanical testing were used to study the nanoscale and tissue scale mechanical response, and histology was used to evaluate protein and cell content.

Fibrils exhibited a simultaneous structural response as the tissue, with 94 ± 2% lower fibril than tissue strains at failure (Figure 5.2-A). During cyclic loading, fibrils exhibited a 0.2% decrease in d-spacing following increased number of cycles, but no change in maximum d-spacing (Figure 5.2-B). Simultaneously as tissue stress relaxation, fibrils underwent relaxation in d-spacing (Figure 5.2-C). A radiation damage test revealed that only small structural changes in comparison to the loading-induced changes occurred during the time of the measurements. Additionally, changes in width of the collagen peaks were found to be related to strain heterogeneity.

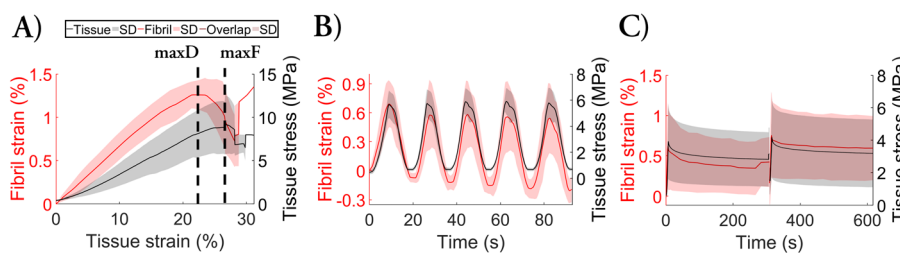

Figure 5.2. Main results from Paper III. Changes in average fibril strain and tissue stress as a function of tissue strain during A) ramp to failure, B) cyclic loading and C) stress relaxation tests.

Unloading of the Achilles tendon led to more crimped and disorganized collagen fibers than in fully loaded tendons, with more local heterogeneities as well as a generally wider range of fibril orientations (Figure 5.3-A). At the fibril level, two distinct populations in orientation were observed primarily in unloaded tendons, potentially belonging to different sub-tendons (Figure 5.3-B). Unloading altered the mechanical response, delaying it at both the fibril and tissue level (Figure 5.3-C). Unloaded tendons exhibited longer toe regions, and as a result reached lower stress during cyclic loading and stress relaxation. Additionally, unloaded tendons had approximately 33% and 47% faster relaxation times during the 1st and 2nd step respectively. Depending on the group and which step, the fibril relaxation was 10-20% slower than tissue relaxation and their ratios of fibril to tissue relaxation times were similar. Unloaded tendons also showed a decrease in cell density and elastin.

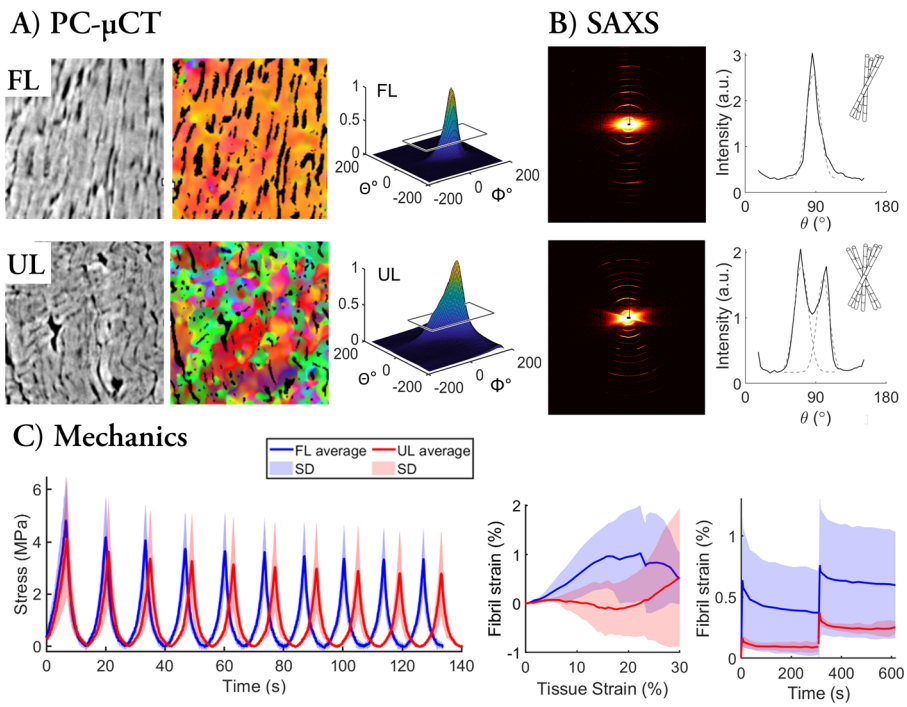

Figure 5.3. Main results from Paper IV. A) Difference in fiber orientation between fully loaded (FL) and unloaded (UL) tendons, obtained by phase contrast μCT (PC- μCT). B) Two types of scattering patterns were identified with SAXS; one population of fibrils oriented parallel to the main axis of the tendon and two populations of fibrils with distinctly separated orientations. The second type was primarily present in unloaded tendons. C) Main changes in tissue and fibril mechanical response due to unloading.

5.3 Mechanobiology of tendon healing (Objective 3)

A combination of synchrotron-based techniques was used to investigate the effect of full loading or unloading during 1-3 weeks of Achilles tendon healing. Phase contrast μCT, SASTT and SAXS were used to study the micro- and nanoscale structure and *in situ* mechanical testing was used to study the nano- and tissue scale mechanical response.

Unloading during the healing process resulted in smaller callus diameters and distance between the stumps, as well as less formation of collagenous material (Figure 5.4-A). Instead of collagen fibers, a large part of the callus in unloaded tendons consisted of adipose tissue. Further, unloading led to a more disorganized collagen network, with both fibers and fibrils being less longitudinally oriented and exhibiting multiple dominant orientations (Figure 5.4-B). The collagen network became more organized with healing time in both groups. Initially, most fibril structural parameters were similar between the two groups, but as healing progressed, the unloaded tendons showed a delay in callus maturation and little to no stump remodeling. This was shown by the lack of merging between callus and stump tissue in for example d-spacing (Figure 5.4-C).

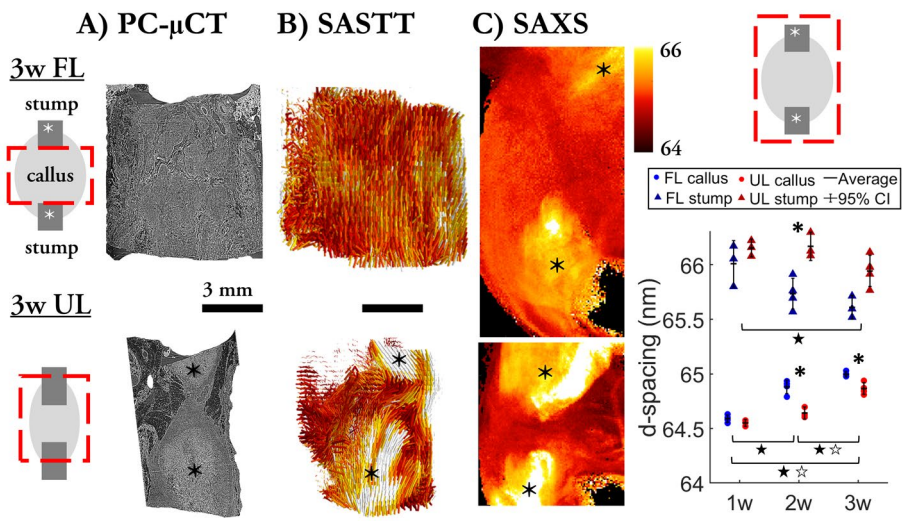

Figure 5.4. Main results from Paper V. A) Micro- and B) nanostructural 3D organization of 3 weeks fully loaded (FL) and unloaded (UL) healing tendons, obtained by phase contrast μCT (PC- μCT) and SASTT respectively. C) Distribution and evolution of d-spacing in healing tendons after 3 weeks, obtained by SAXS. Statistical significance ($p < 0.5$) is indicated for the effect of treatment (*), effect of time in FL (black star) and UL (white star) tendons.

Unloading had no substantial effect on the extrinsic tissue mechanical response of the healing tendons (Figure 5.5-A). Unloading during healing however altered the collagen fibril mechanical response. As opposed to fully loaded tendons, unloaded tendons maintained a relatively constant fibril amount independently of increasing strain steps or healing time (Figure 5.5-B, i). Unloaded tendons had a similar fibril strain response at low tissue strains as fully loaded tendons, but as the strain increased, they exhibited lower fibril strain magnitudes at larger strain steps (Figure 5.5-B, ii). Unloading did not result in any changes in stress relaxation ratio, neither at tissue nor fibril level.

While the effect of reduced loading on the mechanical tissue and fibril responses during early Achilles tendon healing also was evaluated, the results from these experiments are not included in this thesis due to limited time available to untangle some of the experimental difficulties related to these samples.

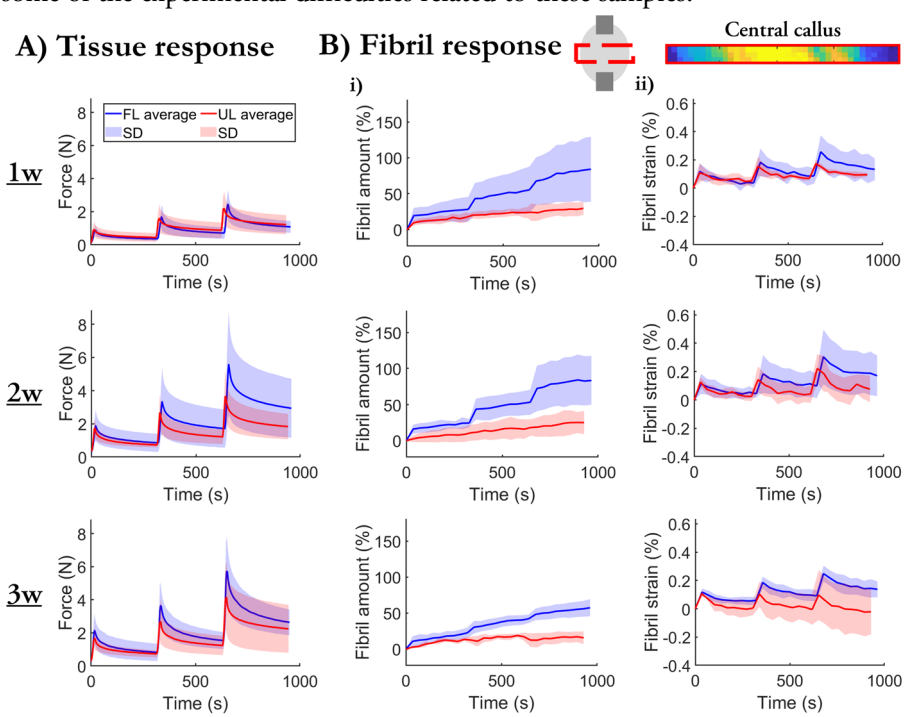

Figure 5.5. Main results from Paper VI. A) Tissue extrinsic mechanical response to loading. B) Fibril mechanical response to loading, showing the average relative changes within the central callus in fibril amount (i) and fibril strain (ii).

6 Discussion

6.1 General

The overall scope of this thesis was to characterize the mechanobiological effects on the micro- and nanoscale in selected musculoskeletal tissues during formation, homeostasis and repair, with focus on the load bearing structural components of mineral and collagen. As such, this thesis highlighted the impact of mechanical loading on developing long bones (Objective 1), elucidated critical effects of immobilization during tendon homeostasis (Objective 2) and assessed the importance of loading for the recovery of structural integrity during early tendon healing (Objective 3). This was achieved through the application of multimodal and multiscale characterization using a range of synchrotron- and lab-based high-resolution techniques, in combination with mechanical testing.

In these studies, a combination of techniques was chosen to extend our current knowledge and to investigate the role of the constituents at different length scales for the structural and mechanical integrity of musculoskeletal tissues. Scattering techniques, PLM and μCT probes the nano- and microscale structural organizations respectively. The orientation, alignment, amount and size of both mineral and collagen structures highly influence the mechanical strength as well as the characteristic viscoelasticity of musculoskeletal tissues. XRF and FTIR are sensitive to the elemental and molecular composition of the tissue. The amount and distribution of elements and proteins provide important insight regarding the dynamic processes through which the tissue composition is changed in response to external stimuli. A better understanding of the relation and interplay between the nano-, micro and the overall tissue scale, may enable the development of improved interventions and rehabilitation to treat pathologies, as well as guidelines to maintain tissue health. Further insights into the processes involved opens up for

development of targeted drugs and other more specialized medical interventions to correct deviations from a healthy state.

The multimodal and multiscale approach of this thesis provided further insight into how the mechanical loading environment affects both the micro- and nanoscale. As has been shown in this thesis, reduced mechanical loading has detrimental effects on both bone and tendon tissues, all the way from the tissue scale down to the nanoscale. The implications of these effects, the challenges of the presented studies, and remaining questions, will be further discussed in the following sections.

6.2 Mechanobiology of long bone mineralization (Objective 1)

Paper I showed that, in only four days of embryonic development, the mineralization was characterized by a rapid transformation of bones from unspecialized shapes, inner structures with low Ca content and unordered mineral crystals, to clearly developed morphology, structure and composition more closely resembling that of the adult. During this time, it was found that the tissue grew extensively in length, organized toward more trabecular- and cortical-like internal structures and that the mineral particles underwent minor reshaping as well as started to orient along the major load axes.

This paper identified that there is a clear spatial distribution of Zn during embryonic long bone formation, with Zn being present in increased levels at regions of new mineral deposition, such as the mineralization front of the growth plate as well as the edges of the bone collar and internal structures. Zn is crucial for fetal bone development and its deficiency is connected to many kinds of skeletal abnormalities [226]. Zn is a co-factor to alkaline phosphatase (ALP) and many matrix metalloproteases (MMPs) crucial to bone mineralization [227–229], such as MMP3, MMP9, MMP13. At the mineralization front of the growth plate, MMP9 is expressed by osteoclasts and MMP13 by chondrocytes as well as osteoblasts. Both enzymes work together to resorb the cartilage template in the hypertrophic zone and coordinate chondrocyte apoptosis, angiogenesis and osteoblastic differentiation [229]. ALP is also present at the mineralization front, mediating the accumulation of the Ca-containing vesicles, and its decline in activity during mineralization has been shown to relate to a loss of Zn [227]. MMP3 as well as MMP13 have also been found in the periosteal cells, outlining the bone collar, as well as in osteocytes and osteoblasts surrounding the lacunae, especially at sites of remodeling [229–231]. Additionally, Zn can substitute Ca in HA, causing a 1-3% volume decrease of the HA unit cell [232,233]. Within osteoblasts, early biomineralization potentially starts through Zn-HA nucleation [232]. While the

exact origin of Zn cannot be conclusively determined by the result of this study, the specific pattern of MMPs observed in other studies points towards the Zn localized at the mineralization front of the growth plate primarily being there as a co-factor to the MMPs. On the other hand, the Zn that was found to outline the bone collar and internal trabecular-like structures, where new bone is being deposited to enlarge as well as remodel the mineralized islands into optimized trabeculae, could be aiding both MMPs and HA nucleation.

Paper II showed that lack of muscles during embryonic long bone development leads to an abnormal mineral particle deposition and growth, characterized by initially less mineralized tissue to later on catch up with the controls just before birth. Muscle-less humeri also exhibited continuous growth of mineral particles in all dimensions which ultimately leads to larger particles than their controls towards the end of embryonic development. Between TS24 and TS27, the muscle-less mice seem to deposit and form mineral faster than their controls. They also exhibited a more homogenous pattern of mineralization, reflected by a more widespread distribution of high levels of Zn.

Long bones are formed in a well-organized and coordinate manner during normal development. During normal conditions, long bones grow isometrically, which requires a specific balance between proximal and distal growth rates in order to maintain the relative position of superstructures (such as the condyles and deltoid tuberosity) [234]. Additionally, a study by Eyal et al. [235] indicates the structural and muscular patterning to be well-regulated and coordinated. The lack of a synchronized reduction in amide content found in Paper II within the hypertrophic zone of the muscle-less limb adds to the notion of muscle contractions playing a fundamental role for coordinated and correct bone growth, as this indicates that the collagen type II in the cartilage template is not broken down and mineralized in the same organized manner as during normal development [229]. Additionally, the molecular content of the growth plate and mineralization front in the muscle-less forelimbs did not exhibit any clear transition with development as in their littermate controls, but instead remained similar throughout the gestational period assessed, further suggesting the loss of coordinated growth due to lack of muscles. The increasingly abnormal localization and levels of Zn in the muscle-less limbs also adds to this notion, as this indicates that the bone formation is not solely restricted to the mineralization front and remodeling zones, and most likely have an altered presence of MMPs. Additionally, the generally larger, continuously growing mineral particles and their more homogenously widespread spatial distribution in muscle-less forelimbs further suggests that new bone formation is taking place across the whole rudiment.

As the embryos grow and the space within the uterus is reduced, passive mechanical stimuli may be exerted on the bones from movements of their mother and normal littermates [236]. These forces could result in spatially unspecific and more uniform stimuli on the bones in muscle-less limbs and could thus be an explanation for the increased and more homogenous mineralization at later development stages.

6.3 Mechanobiology of intact tendons (Objective 2)

Paper III showed that the viscoelastic properties of the Achilles tendon are translated down to the nanoscale fibrils, which exhibited a simultaneous and non-uniform deformation with substantially lower fibril strains compared to overall tissue strains. In the elastic region of tissue deformation, the fibrils simultaneously exhibited a linear behaviour, to then fail close to tissue failure. This paper also identified viscoelastic responses of the fibrils; simultaneously as tissue stress relaxation, fibril strain relaxation occurred and as the tissue strain increased with cyclic loading, fibril strain recovery and stretchability increased.

This study identified substantially lower fibril strains in the rat Achilles tendon than tissue strains. While the Achilles tendon is an energy storing tendon, similar behaviour has been found in positional tendons from rat tails, in which 40-80% lower fibril than tissue strains have been observed [152–156]. The lower fibril than tissue strains indicate that deformation is not only occurring within the fibrils, but also in the matrix between fibrils and at other hierarchical length scales. Similar observations have been made on both smaller and larger length scales as well, with collagen molecules straining less than fibrils [152], fibers straining more than fibrils, but still less than fascicles or full tissue [151,201,237,238], as well as fascicles straining less than the full tissue [201,204]. Gupta et al. [151] identified the dominating contributor to stress relaxation of rat tail fascicles to be inter-fiber sliding. On the larger length scales, Thorpe et al. [204,205,238] have demonstrated that the interfascicular matrix can reach forces up to 30% of the tendon failure force [204] and exhibit alterations in its mechanical properties depending on the tendon type, as well as age.

Whether fibrils and fibers are continuous or not within the tendon is currently under debate. The indication of strain partitioning observed in this study due to the substantially lower fibril than tissue strains points towards discontinuity of these structures. For strain to be partitioned throughout the tissue through sliding between sub-structures such as fibrils, fibers and fascicles, fibrils must be functionally discontinuous. This is further supported by the substantially higher strains observed during mechanical testing of single fibrils, which have been shown to fail around 11-27% strain [239–242]. Additionally, single fibril studies have

identified a two- or three-phase behaviour, depending on the type of tendon [239,242]. Up until 7-10% applied strain, single fibrils show a linear behaviour, but then a decrease in stiffness occurs. When a strain above 15-20% is applied, the fibrils exhibiting three phases also exhibit strain stiffening before failure [242]. As the fibrils in Paper III did not reach as high strains nor seemed to exhibit any of the later phases as observed in the studies on single fibrils, the isolated fibrils seem to have the capacity to deform more than when interconnected and assembled into larger and more complex functional units such as the whole tendon. Additionally, this points towards tissue failure occurring through accumulated damage in the non-collagenous material and connection in-between fibrils, fibers, fasciscles or sub-tendons, rather than within the fibrils themselves. Characterizing true failure of tendons is however very difficult, as it is hard to avoid stress concentrations at the clamps without inducing slipping. Early failure due to stress concentration at the clamps would result in an underestimation of the failure force and slipping would induce an overestimation of tissue strain levels.

Paper IV showed that immobilization of the Achilles tendon leads to a more disorganized tissue, characterized by more crimped fibers and an increased orientational heterogeneity, as well as an impaired mechanical response at both the tissue and fibril level. Unloaded tendons exhibited longer toe regions, which resulted in a delayed and prolonged mechanical response at both levels, ultimately elongating more than fully loaded tendons. The longer toe region was most likely induced by the increased crimp and disorganization at the fiber level and could explain the lower tissue stress as well as fibril strain reached during stress relaxation steps.

This paper identified that fibrils within unloaded tendons, albeit delayed, ultimately reached similar maximum d-spacing as in fully loaded tendons, and tendons from both groups reached maximum fibril strain close to tissue yield. Additionally, no difference in initial d-spacing nor intrafibrillar order was found. While unloaded tendons exhibited faster relaxation times, the ratio of tissue to fibril level relaxation time also remained unchanged compared to fully loaded tendons. Taken together, these results indicate that four weeks of unloading does not directly affect the fibril structure, their mechanical capabilities nor response. Instead, the impaired mechanical response is most likely due to changes on other length scales, such as the increased crimping and disorganization of fibers at the microscale, which in turn indirectly cause an effect on the fibril response as well. It takes larger deformation to straighten and reorient an increased number of crimped and disorganized fibers than for more organized and well aligned fibers. Disorganization of the tissue structure results in less efficiently packed fibers, which in unloaded tendons was identified as lower fiber density. The delayed capacity of the unloaded tendons to carry load as well as the increased risk for

microstructural buckling associated to highly heterotrophic fiber orientations [243], could explain why these tendons have impaired function. The structural and mechanical changes occurring in unloaded tendons could more easily result in local microdamage and could eventually lead to an earlier tissue failure. In turn, this could be one reason to why unloaded tendons failed at lower stresses, had lower elastic moduli as well as often ruptured already in the second strain step during the *ex situ* loading tests.

These severe changes in both microstructural organization and fiber density occurred after four weeks of unloading, despite the reportedly slow turnover of the collagen matrix in tendons [244]. Energy storing tendons, such as the Achilles tendon, has also been found to have substantially slower turnover rate, with the half-life of the collagen matrix in the equine digital flexor tendon being 198 years as compared to the 34 years of the positional common digital extensor tendon [244]. In line with the potentially low collagen turnover, no changes in neither collagen type I nor III were observed following the period of unloading. In fact, there were less cells present in unloaded tendons, which could be an indication of even less activity in both formation and degradation. This points towards the tissue at these length scales simply undergo re-organization of the pre-existing matrix when immobilized. However, less collagen content has been reported in other studies as a result of longer periods of reduced loading (5 to 6 weeks) of the rat Achilles tendon [19,31], as well as signs of an increased collagen turnover during reduced loading (9 weeks) of the rabbit patellar tendon [245]. These changes in collagen content and turnover indicate that the turnover could be faster in smaller animals, which have higher metabolic rates than larger animals such as horses and humans. Additionally, the outcome of these studies most likely also vary due to the different techniques used to measure collagen content and turnover rate. As no changes were observed on the fibril and molecular level in this study, it could also be that the timing of collagen turnover and structural changes might differ between length scales and that more than 4 weeks of unloading is required for quantifiable changes to occur on the smaller length scales compared to the fiber scale.

6.4 Mechanobiology of tendon healing (Objective 3)

Paper V showed that early Achilles tendon healing is a highly complex and heterogenous process, strongly impacted by the loading environment. Immobilization led to a more disorganized matrix at both the micro- and nanoscale, less collagen being formed and an increased presence of adipose tissue. Even though both fully loaded and unloaded tendons became increasingly more

aligned and increased their collagen content from 1 to 3 weeks, unloaded tendons did not reach the same levels as fully loaded tendons.

This paper identified that the healing process is highly heterogeneous, with new collagen formation starting on the sides of the stumps to later progress into the callus region and bridge the tissue. A higher collagen content was observed on the posterior side of the tendon as well as closer to the distal stump, indicating that the collagen formation starts or is more active on the distal side of the tendon, as well as the bridging to be preferential to the posterior side. It has been shown that tenocytes exhibit highly distinct localization during tendon healing. Studies have found that extrinsic cells from the paratenon migrates into the callus and become positive for the Scleraxis marker (Scx^+), which is a characteristic transcription factor for tenogenesis expressed by tenocytes, to then bridge the gap between them [110,111,246]. The paratenon is a sheath which covers the intact tendon, normally consistent of non-Scx expressing cells and circumferential collagen fibrils [246]. Dyment et al. [246] found a preferential localization of these Scx^+ cells during patellar tendon healing on the anterior side. The anterior side of the patellar tendon and the posterior side of the Achilles tendon are both facing away from the body, thus comprising the longest region of the tendon, and most likely under slightly different loading compared to the tendon core and its innermost side. Collagen formation is considered to be strain dependent, typically in response to strain levels up to ~10% [247,248]. Above 10% strain, it is still debated whether collagen formation remains constant, increases or declines [247–250]. The results of this paper could point toward the healing tendon experiencing an internal heterogeneous spatial distribution of loads which translates into different levels of tissue formation and reorientation, or that the tissue formation is primarily guided by other factors than mechanics.

Additionally, it was revealed that immobilization during the early healing time either restricts or delays the formation and maturation of the healing callus, as well as remodeling of the stumps. The newly formed fibrils observed in this study were both less organized and had shorter d-spacing than their intact equivalent. As the initial randomly organized collagen network mainly consists of collagen type III [28,104], the shorter fibrils observed in the callus could be coming from structural differences between the newly formed collagen type III and the typical type I of the intact tendon. Indirectly in line with our findings, other studies have identified the newly formed fibers within the callus to be thinner and more disorganized than those of the stumps [105,251]. Despite both fibril d-spacing and delamination increasing with time independently of the *in vivo* loading environment, unloaded tendons exhibited lower values compared to fully loaded tendons as healing progressed. This difference was most pronounced after two weeks of healing, well in line with similar SAXS and histological observations from reduced loading by

Botox [30]. Additionally, as fibrils within the callus increased in d-spacing, fibrils within the stumps of fully loaded tendons decreased their d-spacing and became less distinct from the surrounding callus tissue, indicating that remodeling of the stump occurred, with their fibrils potentially being broken down or reorganized. This merging of callus and stump tissue was not observed in the unloaded tendons within the investigated time frame, indicating that their stump remodeling is delayed.

Paper VI showed that during early healing of the Achilles tendon, the in vivo loading environment influences the structural response to in situ loading of the newly formed collagen fibrils. Immobilization led to decreased fibril recruitment and fibril extension. In addition to this, unloaded tendons exhibited more heterogenous fibril strain responses to increasing tissue strain compared to fully loaded tendons, despite their absolute fibril strain distributions being more homogenous. However, immobilization did not result in any substantial alteration of the response at the tissue scale, indicating that the nanoscale of the newly formed tissue is more susceptible to changes in the load environment or that the tissue overall geometry and composition of the tendon compensates for this effect.

Fully loaded tendons exhibited a 60-115% average increase in amount of recruited collagen fibrils in response to tissue strain at all healing time points. Thus, full loading during early healing seemingly aids in re-building an effective strain response, even as early as 1 week after injury. Unloaded tendons, however, only exhibited a 2-45% increase in fibril amount and the response remained low across all healing time points. This indicates that immobilization during this early healing period impairs the tissues' ability to recruit fibril in response to the applied loading. One reason behind this impaired ability could be the increased disorganization of unloaded tendons as observed in Paper V. If the matrix is very disorganized and many fibrils are oriented away from the main load direction (and possibly in some cases even perpendicularly to it), the ability of the fibrils to re-orient and organize along the loading direction may be severely restricted.

This paper further supports that immobilization during early healing restricts or delays the formation and maturation of the healing callus, as found in Paper V. This was indicated by both fibril amount and average d-spacing remaining low after three weeks of healing, as opposed to fully loaded tendons which across healing time increased towards intact values. Additionally, while the fibrils independently of *in vivo* loading scenario elongated in response to tissue strains, fibrils in unloaded tendons seemed to reach a limit at higher strains after which they were unable to continue to elongate as much as the fibrils in fully loaded tendons. This weaker fibril strain response in unloaded tendons is most likely a

direct result of their delayed formation and maturation, as well as their less homogenous orientation along the main axis of the tendon.

6.5 Limitations

There is an inherent biological variability both within and between animals. In addition to this, the experimental setup, type of sample preparation, effect of treatments and accuracy of measurement techniques also contribute to data variability. When studying engineered materials, they can often be manufactured to fit the desired measurements and experimental stations to be used. This is typically not an option for non-synthesized biological samples and as a result, large sample groups are needed to be able to detect significant differences when studying biological processes.

The main limitations of the work presented in this thesis are thus related to the use of synchrotron imaging techniques. Synchrotrons have a high demand and relatively low availability compared to lab-based sources. This limited allocated time per experiment strongly restricts the extent of what can be measured with these techniques. Thus, there is a trade-off between number of samples per group, number of groups or stages, number of data points, resolution and size of measurement regions. Depending on the objective, different prioritizations were made to provide the most valuable information. In some cases, this resulted in only one sample per group but several time points and large areas, or several samples per group but comparing few groups and small areas. Another limitation comes with the use of synchrotron radiation; the high photon flux and energy induces radiation damage. Collagen is more sensitive to radiation damage than the HA mineral particles and radiation doses above 35 kGy has been shown to critically impair the mechanical properties of bone, such as plasticity, maximum ending strength and fibril strain [252]. For that reason, in all studies probing the collagen structure or involving mechanical testing, a radiation damage test was conducted prior to the experiments in order to assess their feasibility and tune the experimental parameters to minimize the effect of radiation on the results. Additionally, to conduct some of the synchrotron- and lab-based experiments performed in this thesis, different sample preparations were needed. Fixing of the samples causes dehydration and potential structural and compositional changes to the tissue, such as loss of Ca or other trace elements [103,253]. In Paper I and II, the majority of the measurements had to be conducted on thin 2D slices and the samples were thus sectioned. Sectioning is destructive and can cause defects to the sample, as well as cannot be fully representative of the 3D complexity of the tissue. However, care was taken to minimize inter-sample variations due to sample preparation by using the same protocols for all related samples. Finally, the limited

view of 2D was, when possible, supported by 3D measurements such as μCT and SASTT.

The magnitude, duration or frequency of *in vivo* forces exerted on both intact and healing Achilles tendons is largely unknown. Further, how the unloading model used in this study as well as others (Botox, tail suspension, treadmill running) translates to alterations in forces on the Achilles tendon is still unclear. Studies on rats and mice have identified peak ground reaction forces to be 2N during gait [254] and approximately 0.6% of the body mass [255]. Additionally, Botox injections have been shown to decrease the ground reaction forces with 10-15% up until 21 days post injection, and to still remain slightly inferior up until 42 days post injection [255]. Musculoskeletal models have also been used to estimate strains in healing rat Achilles tendons [256,257], which together with experimental studies could provide further insight into the loading environment of the tendon.

Whether the unloading animal models correspond well to physiological loading scenarios in humans is still unclear. Recent studies have been able to measure *in vivo* strain and force of human Achilles tendons during different types of exercises [258,259]. Despite the extent of the unloading effect being unknown, the animal model used in this thesis was developed to correspond as well as possible to patient situations where the tendon is intact and immobilized due to an unrelated injury, such as broken foot or ankle. When it comes to the rehabilitation period during tendon healing, however, it is most likely not fully representative of the patient scenario. The injured tendon of patients has commonly been immobilized by a brace for several weeks [260,261], but many clinical rehabilitation protocols now also involve minor loading of the tendon, through e.g. weight bearing on the foot or different rehabilitation exercises [260,262–265]. In the animal model used in this thesis, neither the fully loaded nor unloaded protocol corresponds to this kind of mild and intermittent loading. In the fully loaded scenario, the rats will walk normally on their injured leg already from day one and thus load their tendon more heavily than a patient would do at this stage. The unloading on the other hand, removes most mechanical stimuli. Other unloading models which do not completely unload the tendon, such as only Botox injections or tail suspension, might therefore be more accurately resembling the current rehabilitation situation for patients.

While providing highly valuable information and insight on Achilles tendon fibril mechanics, the *in situ* mechanical testing performed in this thesis has several drawbacks. The fastest achievable displacement rate with the loading device at the time was much slower than what would be expected under physiological conditions. As tendons are highly viscoelastic, they will relax their structure with time and the possibility of distinguishing the elastic response from the sliding or relaxation behaviour is limited when the strain rate is too low. This most likely

contributed to the unusually large tissue failure strains. The clamp design of this loading device was also not ideal, as it had flat grips. The flat grips limited the possibility of mounting the tendons in their physiological angle in relation to the heel and most likely induced damage as well as stress concentration at the clamp interface. As the mechanical properties of tendons are highly dependent on their large water content, we focused on making sure the tendons were kept hydrated throughout all the tests. In the *in situ* experiments, this was done by minimizing the time the tendons were mounted and by placing Kapton tape around the exposed tendon between the clamps. Visual inspection confirmed that the tissue under the Kapton film remained hydrated after the tests. Either way, it would have been more ideal to perform these tests in a hydrated chamber or bath.

6.6 Future perspectives

The thorough multiscale characterization presented in this thesis provides new insights into the basis of vital processes as well as their mechanobiological respoonse, which may aid in improved diagnostics, treatment and rehabilitation of abnormal or pathological biomechanics of musculoskeletal tissues. The specific focus on the nanoscale provided increased knowledge which hopefully will aid in the future design of more targeted drugs and interventions. However, there are still many aspects that need further research.

Short term perspectives: continuation of this thesis

The ideal continuation of this thesis would address the limitations mentioned above, as well as expand the work to fill the gaps in knowledge not covered by this thesis.

This thesis highlighted the clear role of mechanobiology on long bone mineralization, especially at the mineralization front. However, as most of the nanoscale investigation was conducted on fixed 2D sections, further investigation is needed to consider the 3D anisotropic structure and composition, as well as samples closer to native conditions. While the μCT and SASTT measurements in this thesis provided a global picture of the changes in micro- and nanoscale structural organization, detailed 3D information and a complete understanding of the mechanisms involved at the mineralization front is still missing. To this end, higher resolution tomography as well as recent advances within 3D imaging should be applied. For example, simultaneous diffraction and XRF tomography has been utilized to study the 3D structure and mineralization of human lamellar bone [168,171,266,267], down to both micron and submicron spatial resolution.

The findings presented in this thesis provides further insight into and clearly highlights the heterogeneity of Achilles tendons at several length scales. The here presented results, taken together with studies indicating how strain is partitioned between length scales [151,199,201,203,204,237,238,268] and how deformation is higher in the core of human Achilles tendons [269,270], clearly indicates that there is a need to elucidate the mechanical deformation mechanisms in 3D, such as the spatial strain distribution within the entire volume of the tendon. With the recent advances at synchrotrons, this could be achieved by combining 3D imaging techniques such as phase contrast μCT and SASTT with *in situ* loading. While the advances of μCT measurements have recently enabled sufficiently fast measurements for this, the current measurement times of SASTT are still too slow. However, with the upcoming advances of fourth generation synchrotron sources [271–273] and their upgrades to improved detectors, faster experimental stages and program updates, this will hopefully be possible within the coming years.

This thesis provided further insights into the importance of the *in vivo* loading environment on the tendon structure and mechanical response across multiple length scales. For intact tendons, only physiological loading magnitude was evaluated compared to immobilization. Thus, an understanding of how increased or prolonged levels of inflammation due to either excessive loading or microtrauma affect the structure and multiscale mechanical response of the tendon is still lacking. This could be studied by either subjecting the rats to high levels of exercise (e.g. treadmill running) or by inducing microtrauma trough needling [274]. For healing tendons on the other hand, only the extreme levels of loading were considered, which as discussed above most likely do not fully mimic the patient scenario. Thus, there is still a need for further investigation into more complex and clinically relevant loading environments following rupture. To this end, animal models with intermittent periods of loading as well a combined model starting with unloading to later gradually re-introduce loading would be closer to the patient scenario. Re-introduction of loading is however not compatible with the animal model used in this thesis, as the effect of Botox cannot be removed, and it tends to cause severe muscle atrophy [31]. By applying a different unloading animal model however, such as tail suspension, this would be possible. Additionally, the work of this thesis focused on short term healing during which the tendon does not completely heal. Thus, to fully elucidate the effect of loading environment on the healed tendon as well as risk for re-ruptures, longer experiments needs to be conducted. For this, however, one would need to use a different animal, as rats tend to form an excessive number of heterotopic ossifications within their Achilles tendon both in native state as well as during healing [136,275].

Long term perspectives: the road to the clinics

The work of this thesis, as well as most other studies on the mechanobiological effects in musculoskeletal tissues, has been conducted using controlled animal models. In most animal models, a pathology or injury is induced, and animals are sacrificed at specific time points for *ex vivo* evaluation. However, *ex vivo* investigations are highly limited as it completely excludes e.g. cell functions, systemic effects, neuromuscular control and other physiological aspects which are intricately connected with tissue properties. Small animal *in vivo* μCT instruments provide a step further towards this goal, by enabling studies to follow the course of e.g. healing or treatments within the same animal, and thus providing more comprehensive information regarding the kinetics and mechanisms involved. Lab-based *in vivo* μCT has for example been used to study the repair process during bone fracture healing [276–278] and to track bone morphological effects of mechanical stimulation [279,280]. While these *in vivo* scanners currently have high sensitivity and resolution, they are still not on the level of *ex vivo* instruments and synchrotrons. Furthermore, the low contrast for soft tissues limits their possibilities for imaging other non-mineralized musculoskeletal tissues. However, emerging capabilities at beamlines and recent synchrotron upgrades have now also enabled *in vivo* synchrotron imaging of small animals, such as dynamic phase contrast imaging of lungs in mice undergoing respiratory treatment [281,282]. With this possibility for future studies conducting synchrotron enhanced *in vivo* imaging, tracking development, pathologies, regeneration and treatments in physiological conditions, crucial information can be obtained to improve our understanding of the mechanobiological interplay in musculoskeletal tissues, and bring us one step closer towards optimal care of musculoskeletal abnormalities.

Ultrasound and magnetic resonance imaging (MRI) are commonly used in the clinics to investigate structural changes and to diagnose ruptures [283,284]. Ultrasound coupled to elastography or Doppler are often used to measure elasticity or stiffness of the tendons *in vivo*, for example during different activities [285,286] and as a result of post-rupture rehabilitation [284]. With recent developments into kinematic MRI, *in vivo* strains in the human Achilles tendon have also been investigated, for example to evaluate the outcome of surgical or non-surgical post-rupture treatment [287]. To bring the field forward, these techniques should be used to temporally study the healing process in patients. Studies utilizing recurring and methodological *in vivo* evaluation of the mechanical properties, structural organization and composition during different rehabilitation protocols or interventions would provide the means to fully optimize clinical treatment.

While quantitative MRI based on ultra-short time echo imaging has been shown to provide information which is indicative of the collagen structure and water content in tendons [288,289], currently both clinical ultrasound and MRI primarily

enables quantifications only at the tissue scale (mesoscale). However, as it has been further highlighted by the work in this thesis, the tendon has a multiscale mechanical response and all hierarchical levels should be investigated to improve our understanding of *in vivo* tendon mechanobiology in humans. Recent advances over the last decade within the field of X-ray tomography have led to the development of differential phase contrast (DPC) imaging [290–292]. DPC utilizes a series of gratings, which induces absorption, differential phase and small-angle scattering contrast simultaneously, thereby significantly improving a variety of diagnostics. Due to the need for better clinical diagnostics of soft tissues, while still remaining sufficiently fast and at low radiation doses, extensive research is being conducted to bring DPC towards this goal. For example, DPC has successfully been combined with mammography to improve the diagnostics of breast cancer [292], for which it has shown to provide better classification of microcalcifications as well as improved soft tissue contrast compared to conventional mammography. While most studies using DPC have been performed in a pre-clinical setting, a recent study set up a grating interferometer compatible with the standard clinical mammography system and could be performed at radiation doses within clinical regulations [293]. With future developments of this clinically promising imaging technique, highly resolved *in vivo* measurements of other soft tissues such as tendons will also be feasible. The combined phase and scattering contrast provided by DPC would provide detailed information about the micro- and nanostructure, and by combining this imaging technique with different exercises, details regarding patient specific *in vivo* micro- and nanostructural mechanical responses could be elucidated. With such knowledge, we would not only gain a better understanding of optimal clinical treatments and protocols, but also be able to specifically tailor these to the individual patient.

7 Summary and conclusions

The overall aim of the presented thesis work was to characterize how mechanical loading, or lack thereof, affects the smaller length scales in developing bones as well as both intact and healing Achilles tendons. The multimodal and multiscale approach of combining several synchrotron-enhanced and lab-based techniques enabled complementary information on several length scales simultaneously and could thus provide additional insight regarding the relationship between them.

Below, the main conclusions of each Paper (I-VI) are summarized.

I. *Zinc is specifically localized to regions of new mineral deposition in embryonic long bones and the newly formed mineral particles undergo reorganization during development.* Humeri from mice at different embryonic development stages were investigated to document the evolution of structure and composition at the nanoscale. XRF revealed a localized presence of Zn, and SAXS and WAXS that the mineral particles at sites of new mineralization are thicker, longer and narrower compared to more mature regions.

II. *Absence of skeletal muscles during embryonic long bone development leads to a delayed and abnormal mineral deposition and growth.* Humeri from mice at different embryonic development stages were investigated to obtain evolution of nanostructure and composition. XRF revealed a more widespread and homogenous distribution of Zn in muscle-less bones, indicating a more homogenous mineral formation, and SASTT, SAXS and WAXS that their mineral particles continuously grew in size to ultimately become larger than those of their healthy littermates.

III. *Nanoscale fibrils in Achilles tendons respond simultaneously as the tissue, and the viscoelasticity is transferred down to the nanoscale.* Achilles tendons from rats were investigated to obtain both nanostructural fibril and tissue mechanical response. The simultaneous SAXS and *in situ* loading revealed that fibrils strain simultaneously but substantially less than the applied tissue strain and that they exhibit increased stretchability and recovery during cyclic loading, as well as strain relaxation during tissue stress relaxation.

IV. *Unloading of the Achilles tendon leads to a disorganized collagen structure and an altered mechanical response.* Achilles tendons from rats subjected to either full loading or unloading were investigated to obtain micro- and nanostructural information, as well as mechanical and cellular properties in relation to *in vivo* loading environment. Phase-contrast μCT revealed that unloaded tendons had more crimped and disorganized fibers, and SAXS and mechanical data revealed a delayed fibril and tissue response.

V. *Unloading of the Achilles tendon during healing leads to less collagen formation and a more disorganized collagen organization.* Healing Achilles tendons from rats subjected to either full loading or unloading during the early healing process were investigated to obtain 3D micro- and nanostructural information of the newly formed tissue. Phase-contrast μCT and SASTT revealed that unloaded tendons had less amount of and more disorganized collagenous material, as well as a larger presence of adipose tissue. SASTT and SAXS revealed a delay in maturation of collagen structural parameters, as well as stump remodeling.

VI. *Unloading of the Achilles tendon during healing leads to an impaired collagen fibril response to loading.* Healing Achilles tendons from rats subjected to either full loading or unloading during the early healing process were investigated to obtain both nanostructural fibril and tissue mechanical response of the newly formed tissue. The simultaneous SAXS and *in situ* loading revealed that unloading during early healing severely impairs the fibril mechanical response, resulting in decreased fibril recruitment and ability for fibril extension.

References

1. Fratzl P. Collagen: Structure and Mechanics, an Introduction. In: Collagen. Boston, MA: Springer US; 2008. p. 1–13.
2. Fratzl P, Weinkamer R. Nature's hierarchical materials. Prog Mater Sci. 2007;52(8):1263–334.
3. Frost HM. From Wolff's law to the Utah paradigm: Insights about bone physiology and its clinical applications. Anat Rec. 2001;262(4):398–419.
4. Nowlan NC, Murphy P, Prendergast PJ. Mechanobiology of embryonic limb development. Ann N Y Acad Sci. 2007;1101:389–411.
5. Sharir A, Stern T, Rot C, Shahar R, Zelzer E. Muscle force regulates bone shaping for optimal load-bearing capacity during embryogenesis. Development. 2011;138:3247–59.
6. Rodriguez JI, Garcia-Alix A, Palacios J, Paniagua R. Changes in the Long Bones Due to Fetal Immobility Caused by Neuromuscular Disease. J bone Jt Surg. 1988;1052–60.
7. Rodríguez JI, Palacios J, García-Alix A, Pastor I, Paniagua R. Effects of immobilization on fetal bone development. A morphometric study in newborns with congenital neuromuscular diseases with intrauterine onset. Calcif Tissue Int. 1988;43(6):335–9.
8. Ward KA, Caulton JM, Adams JE, Mughal MZ. Perspective: Cerebral palsy as a model of bone development in the absence of postnatal mechanical factors. J Musculoskelet Neuronal Interact. 2006;
9. Shapiro F. Bone development and its relation to fracture repair. The role of mesenchymal osteoblasts and surface osteoblasts. Eur Cells Mater. 2008;15:53–76.
10. Olsen BR, Reginato AM, Wang W. Bone development. Annu Rev Cell

Dev Biol. 2000;16:191–220.
11. Nowlan NC, Murphy P, Prendergast PJ. Mechanobiology of embryonic limb development. Ann N Y Acad Sci. 2007;1101:389–411.
12. Pierantoni M, Le Cann S, Sotiriou V, Ahmed S, Bodey AJ, Jerjen I, Nowlan NC, Isaksson H. Muscular loading affects the 3D structure of both the mineralized rudiment and growth plate at early stages of bone formation. Bone. 2021;145(January):115849.
13. Gomez C, David V, Peet NM, Vico L, Chenu C, Malaval L, Skerry TM. Absence of mechanical loading in utero influences bone mass and architecture but not innervation in Myod-Myf5-deficient mice. J Anat. 2007;210(3):259–71.
14. Killion CH, Mitchell EH, Duke CG, Serra R. Mechanical loading regulates organization of the actin cytoskeleton and column formation in postnatal growth plate. Mol Biol Cell. 2017;28(14):1862–70.
15. Shwartz Y, Farkas Z, Stern T, Aszó Di B A, Zelzer E. Muscle contraction controls skeletal morphogenesis through regulation of chondrocyte convergent extension. Dev Biol. 2012;370:154–63.
16. Heinemeier KM, Kjaer M. In vivo investigation of tendon responses to mechanical loading. Muscoluoskelet Nueronal Interact. 2011;11(January):115–23.
17. Wang JHC, Guo Q, Li B. Tendon biomechanics and mechanobiology - A minireview of basic concepts and recent advancements. J Hand Ther. 2012;25(2):133–41.
18. Wang JHC. Mechanobiology of tendon. J Biomech. 2006;39(9):1563–82.
19. Khayyeri H, Blomgran P, Hammerman M, Turunen MJ, Löwgren A, Guizar-Sicairos M, Aspenberg P, Isaksson H. Achilles tendon compositional and structural properties are altered after unloading by botox. Sci Rep. 2017 Dec 12;7(1):13067.
20. Finni T, Bernabei M, Baan GC, Noort W, Tijs C, Maas H. Non-uniform displacement and strain between the soleus and gastrocnemius subtendons of rat Achilles tendon. Scand J Med Sci Sport. 2018;28(3):1009–17.
21. Maas H, Noort W, Baan GC, Finni T. Non-uniformity of displacement and strain within the Achilles tendon is affected by joint angle configuration and differential muscle loading. J Biomech. 2020;101:109634.
22. Khayyeri H, Blomgran P, Hammerman M, Turunen MJ, Löwgren A, Guizar-Sicairos M, Aspenberg P, Isaksson H. Achilles tendon compositional and structural properties are altered after unloading by

botox. Sci Rep. 2017;7(1).
23. Shwartz Y, Blitz E, Zelzer E. One load to rule them all: Mechanical control of the musculoskeletal system in development and aging. Differentiation. 2013;86(3):104–11.
24. Huttunen TT, Kannus P, Rolf C, Felländer-Tsai L, Mattila VM. Acute achilles tendon ruptures: Incidence of injury and surgery in Sweden between 2001 and 2012. Am J Sports Med. 2014;42(10):2419–23.
25. Lantto I, Heikkinen J, Flinkkilä T, Ohtonen P, Leppilahti J. Epidemiology of Achilles tendon ruptures: Increasing incidence over a 33-year period. Scand J Med Sci Sports. 2015;25(1):e133–8.
26. Lemme NJ, Li NY, DeFroda SF, Kleiner J, Owens BD. Epidemiology of Achilles Tendon Ruptures in the United States: Athletic and Nonathletic Injuries From 2012 to 2016. Orthop J Sport Med. 2018;6(11).
27. Snedeker JG, Foolen J. Tendon injury and repair – A perspective on the basic mechanisms of tendon disease and future clinical therapy. Acta Biomater. 2017 Nov 1;63:18–36.
28. Notermans T, Hammerman M, Eliasson P, Isaksson H. Tendon mechanobiology in small animal experiments during post-transection healing. Eur Cells Mater. 2021;42:375–91.
29. Maempel JF, White TO, Mackenzie SP, McCann C, Clement ND. The epidemiology of Achilles tendon re-rupture and associated risk factors: male gender, younger age and traditional immobilising rehabilitation are risk factors. Knee Surgery, Sport Traumatol Arthrosc. 2022;30(7):2457–69.
30. Khayyeri H, Hammerman M, Turunen MJ, Blomgran P, Notermans T, Guizar-Sicairos M, Eliasson P, Aspenberg P, Isaksson H. Diminishing effects of mechanical loading over time during rat Achilles tendon healing. Wang JH-C, editor. PLoS One. 2020 Dec 14;15(12):e0236681.
31. Eliasson P, Fahlgren A, Pasternak B, Aspenberg P. Unloaded rat Achilles tendons continue to grow, but lose viscoelasticity. J Appl Physiol. 2007;103(2):459–63.
32. Hammerman M, Dietrich-Zagonel F, Blomgran P, Eliasson P, Aspenberg P. Different mechanisms activated by mild versus strong loading in rat Achilles tendon healing. PLoS One. 2018;13(7).
33. Eliasson P, Andersson T, Aspenberg P. Influence of a single loading episode on gene expression in healing rat Achilles tendons. J Appl Physiol. 2012;112(2):279–88.
34. Andersson T, Eliasson P, Aspenberg P. Tissue memory in healing tendons:

Short loading episodes stimulate healing. J Appl Physiol. 2009;107(2):417–21.
35. Killian ML, Cavinatto L, Galatz LM, Thomopoulos S. The role of mechanobiology in tendon healing. J Shoulder Elb Surg. 2012 Feb;21(2):228–37.
36. Blomgran P, Blomgran R, Ernerudh J, Aspenberg P. A possible link between loading, inflammation and healing: Immune cell populations during tendon healing in the rat. Sci Rep. 2016;6.
37. Als-Nielsen J, McMorrow D. Elements of Modern X-ray Physics. Second Edi. Wiley; 2011.
38. Buckwalter JA, Glimcher MJ, Cooper RR, Recker R. Bone biology. I: Structure, blood supply, cells, matrix, and mineralization. Vol. 45, Instructional course lectures. 1996. p. 371–86.
39. Reznikov N, Shahar R, Weiner S. Bone hierarchical structure in three dimensions. Acta Biomater. 2014;10:3815–26.
40. Reznikov N, Bilton M, Lari L, Stevens MM, Kröger R. Fractal-like hierarchical organization of bone begins at the nanoscale. Science (80-). 2018;360:1–10.
41. Kronenberg HM. Developmental regulation of the growth plate. Nature. 2003.
42. Nowlan NC, Sharpe J, Roddy KA, Prendergast PJ, Murphy P. Mechanobiology of embryonic skeletal development: Insights from animal models. Birth Defects Res Part C - Embryo Today Rev. 2010;90(3):203–13.
43. Kilborn SH, Trudel G, Uhthoff H. Review of Growth Plate Closure Compared with Age at Sexual Maturity and Lifespan in Laboratory Animals. Contemp Top Lab Anim Sci. 2002;41(5):21–6.
44. Mahamid J, Sharir A, Gur D, Zelzer E, Addadi L, Weiner S. Bone mineralization proceeds through intracellular calcium phosphate loaded vesicles: A cryo-electron microscopy study. J Struct Biol. 2011;174(3):527–35.
45. Kerschnitzki M, Akiva A, Ben Shoham A, Asscher Y, Wagermaier W, Fratzl P, Addadi L, Weiner S. Bone mineralization pathways during the rapid growth of embryonic chicken long bones. J Struct Biol. 2016;
46. Cui L, Houston DA, Farquharson C, MacRae VE. Characterisation of matrix vesicles in skeletal and soft tissue mineralisation. Vol. 87, Bone. Elsevier Inc.; 2016. p. 147–58.
47. Reznikov N, Hoac B, Buss DJ, Addison WN, Barros NMT, McKee MD.

Biological stenciling of mineralization in the skeleton: Local enzymatic removal of inhibitors in the extracellular matrix. Bone. 2020;138(May):115447.

48. Hasegawa T, Yamamoto T, Tsuchiya E, Hongo H, Tsuboi K, Kudo A, Abe M, Yoshida T, Nagai T, Khadiza N, et al. Ultrastructural and biochemical aspects of matrix vesicle-mediated mineralization. Vol. 53, Japanese Dental Science Review. Elsevier Ltd; 2017. p. 34–45.
49. Wuthier RE. Matrix vesicles: structure, composition, formation and function in calcification. Front Biosci. 2011;16(8):2812–902.
50. Boyde A, Shapiro IM. Histochemistry Energy Dispersive X-Ray Elemental Analysis of Isolated Epiphyseal Growth Plate Chondrocyte Fragments. Vol. 69, Histochemistry. 1980.
51. Shapiro IM, Boyde A. Microdissection-elemental analysis of the mineralizing growth cartilage of the normal and rachitic chick. Metab Bone Dis Relat Res. 1984;5(6):317–26.
52. Haimov H, Shimoni E, Brumfeld V, Shemesh M, Varsano N, Addadi L, Weiner S. Mineralization pathways in the active murine epiphyseal growth plate. Bone. 2020 Jan 1;130.
53. Landis WJ, Glimcher MJ. Electron optical and analytical observations of rat growth plate cartilage prepared by ultracryomicrotomy: The failure to detect a mineral phase in matrix vesicles and the identification of heterodispersed particles as the initial solid phase of calcium p. J Ultrasructure Res. 1982;78(3):227–68.
54. Akiva A, Nelkenbaum O, Schertel A, Yaniv K, Weiner S, Addadi L. Intercellular pathways from the vasculature to the forming bone in the zebrafish larval caudal fin: Possible role in bone formation. J Struct Biol. 2019;206(2):139–48.
55. Nicole S, Diaz CC, Frugier T, Melki J. SPINAL MUSCULAR ATROPHY : RECENT ADVANCES AND FUTURE PROSPECTS. 2002;(July):4–13.
56. Wesström G, Bensch J, Schollin J. Congenital myotonic dystrophy. Acta Paediatr Scand. 1986;75(849–854):92–4.
57. Roberts CD, Vogtle L, Stevenson RD. Effect of hemiplegia on skeletal maturation. J Pediatr. 1994;125(5 PART 1):824–8.
58. Giorgi M, Carriero A, Shefelbine SJ, Nowlan NC. Effects of normal and abnormal loading conditions on morphogenesis of the prenatal hip joint: Application to hip dysplasia. J Biomech. 2015;48:3390–7.
59. Homer CJ, Baltz RD, Hickson GB, Miles P V., Newman TB, Shook JE,

Zurhellen WM, Goldberg MJ, Harcke TH, Hirsch A, et al. Clinical practice guideline: Early detection of developmental dysplasia of the hip. Pediatrics. 2000;105(4 I):896–905.

60. Miller ME, Hangartner TN. Temporary brittle bone disease: Association with decreased fetal movement and osteopenia. Calcif Tissue Int. 1999;64(2):137–43.
61. Dabezies EJ, Warren PD. Fractures in very low birth weight infants with rickets. Clin Orthop Relat Res. 1997;335:233–9.
62. Hall BK, Herring SW. Paralysis and growth of the musculoskeletal system in the embryonic chick. J mMorphology. 1990;206(1):45–56.
63. Hosseini A, Hogg DA. The effects of paralysis on skeletal development in the chick embryo. I. General effects. J Anat. 1991;177:159–68.
64. Germiller JA, Goldstein SA. Structure and Function of Embryonic Growth Plate in the Absence of Functioning Skeletal Muscle. 1997;
65. Nowlan NC, Prendergast PJ, Murphy P. Identification of mechanosensitive genes during embryonic bone formation. PLoS Comput Biol. 2008;4(12).
66. Hogg DA. A re-investigation of the centres of ossification in the avian skeleton at and after hatching. 1980;
67. Domenech-Ratto G, Fernandez-Villacanas MM, Ballester-Moreno A, Domenech-Asensi P. Development and segments of cartilage canals in the chick embryo. A light microscope study. Eur J Anat. 1999;3(3):121–6.
68. Blumer MJF, Longato S, Richter E, Pérez MT, Konakci KZ, Fritsch H. The role of cartilage canals in endochondral and perichondral bone formation : are there similarities between these two processes ? 2005;359–72.
69. Rudnicki MA, Schnegelsberg PNJ, Stead RH, Braun T, Arnold HH, Jaenisch R. MyoD or Myf-5 is required for the formation of skeletal muscle. Cell. 1993;75(7):1351–9.
70. Nowlan NC, Bourdon C, Dumas G, Tajbakhsh S, Prendergast PJ, Murphy P. Developing bones are differentially affected by compromised skeletal muscle formation. Bone. 2010;46:1275–85.
71. Rodríguez JI, Palacios J, Ruiz A, Sanchez M, Alvarez I, Demiguel E. Morphological changes in long bone development in fetal akinesia deformation sequence: An experimental study in curarized rat fetuses. Teratology. 1992;45(2):213–21.
72. Shwartz Y, Farkas Z, Stern T, Aszódi A, Zelzer E. Muscle contraction controls skeletal morphogenesis through regulation of chondrocyte

convergent extension. Dev Biol. 2012;370(1):154–63.
73. Franz T, Kothary R, Surani MAH, Halata Z, Grim M. Anatomy and Embryology The Splotch mutation interferes with muscle development in the limbs. Vol. 187, Anat Embryol. 1993.
74. Kablar B, Krastel K, Tajbakhsh S, Rudnicki MA. Myf5 and MyoD activation define independent myogenic compartments during embryonic development. 2003;258:307–18.
75. Powell JA, Petherbridge L, Flucher BE. Formation of triads without the dihydropyridine receptor subunits in cell lines from dysgenic skeletal muscle. J Cell Biol. 1996;134(2):375–87.
76. Taye N, Karoulias SZ, Hubmacher D. The "other" 15–40%: The Role of Non-Collagenous Extracellular Matrix Proteins and Minor Collagens in Tendon. Vol. 38, Journal of Orthopaedic Research. John Wiley and Sons Inc.; 2020. p. 23–35.
77. Eyre DR, Paz MA, Gallop PM. Cross-linking in collagen and elastin. Vol. VOL. 53, Annual Review of Biochemistry. 1983. p. 717–48.
78. Wess TJ, Hammersley AP, Wess L, Miller A. Molecular Packing of Type I Collagen in Tendon. 1998;
79. Vitro IN, Abrahams M. MECHANICAL BEHAVIOUR OF TENDON A PRELIMINARY REPORT. Med biol Engng. 1967;5:433–43.
80. Diamant J, Keller A, Baer E, Litt M, Arridge RG. Collagen; ultrastructure and its relation to mechanical properties as a function of ageing. Proc R Soc London Ser B Biol Sci. 1972;180(60):293–315.
81. Buchanan CI, Marsh RL. Effects of exercise on the biomechanical, biochemical and structural properties of tendons. Comp Biochem Physiol - A Mol Integr Physiol. 2002;133(4):1101–7.
82. Freedman BR, Bade ND, Riggin CN, Zhang S, Haines PG, Ong KL, Janmey PA. The (dys)functional extracellular matrix. Biochim Biophys Acta - Mol Cell Res. 2015;1853(11):3153–64.
83. Kjær M. Role of Extracellular Matrix in Adaptation of Tendon and Skeletal Muscle to Mechanical Loading. Physiol Rev. 2004;84(2):649–98.
84. Langberg H, Rosendal L, Kjær M. Training-induced changes in peritendinous type I collagen turnover determined by microdialysis in humans. J Physiol. 2001;534(1):297–302.
85. de Boer MD, Selby A, Atherton P, Smith K, Seynnes OR, Maganaris CN, Maffulli N, Movin T, Narici M V., Rennie MJ. The temporal responses of protein synthesis, gene expression and cell signalling in human quadriceps muscle and patellar tendon to disuse. J Physiol. 2007

Nov;585(1):241–51.
86. Dideriksen K, Boesen AP, Reitelseder S, Couppé C, Svensson R, Schjerling P, Magnusson SP, Holm L, Kjaer M. Tendon collagen synthesis declines with immobilization in elderly humans: No effect of anti-inflammatory medication. J Appl Physiol. 2017;122(2):273–82.
87. Maganaris CN, Reeves ND, Rittweger J, Sargeant AJ, Jones DA, Gerrits K, De Haan A. Adaptive response of human tendon to paralysis. Muscle and Nerve. 2006;33(1):85–92.
88. Kubo K, Akima H, Ushiyama J, Tabata I, Fukuoka H, Kanehisa H, Fukunaga T. Effects of 20 days of bed rest on the viscoelastic properties of tendon structures in lower limb muscles. Br J Sports Med. 2004;38(3):324–30.
89. Hess G. Achilles tendon ruptures. Foot ankle Spec. 2009;3(1):29–32.
90. Leppilahti J, Orava S. Total achilles tendon rupture. A review. Sport Med. 1998;25(2):79–100.
91. Millar NL, Silbernagel KG, Thorborg K, Kirwan PD, Galatz LM, Abrams GD, Murrell GAC, McInnes IB, Rodeo SA. Tendinopathy. Nat Rev Dis Prim. 2021;7(1).
92. Hopkins C, Fu SC, Chua E, Hu X, Rolf C, Mattila VM, Qin L, Yung PSH, Chan KM. Critical review on the socio-economic impact of tendinopathy. Asia-Pacific J Sport Med Arthrosc Rehabil Technol. 2016;4:9–20.
93. Kujala U, Sarna S, Kaprio J. Cumulative Incidence of Achilles Tendon rupture and Tendinopathy in Male Former Elite Athletes. Clin J Sport Med. 2005;15(3):133.135.
94. Riel H, Lindstrøm CF, Rathleff MS, Jensen MB, Olesen JL. Prevalence and incidence rate of lower-extremity tendinopathies in a Danish general practice: A registry-based study. BMC Musculoskelet Disord. 2019;20(1):4–9.
95. Langberg H, Ellingsgaard H, Madsen T, Jansson J, Magnusson SP, Aagaard P, Kjær M. Eccentric rehabilitation exercise increases peritendinous type I collagen synthesis in humans with Achilles tendinosis. Scand J Med Sci Sport. 2007;17(1):61–6.
96. Almeida-Silveira MI, Lambertz D, Pérot C, Goubel F. Changes in stiffness induced by hindlimb suspension in rat Achilles tendon. Eur J Appl Physiol Occup Physiol. 2000;81(3):252–7.
97. Nakagawa Y, Totsuka M, Sato T, Fukuda Y, Hirota K. Effects of odisuse on the ultrastructure of the achilles tendon in rats. Eur J Appl Physiol.

1989;59:239–42.
98. Ikoma K, Kido M, Nagae M, Ikeda T, Shirai T, Ueshima K, Arai Y, Oda R, Fujiwara H, Kubo T. Effects of stress-shielding on the dynamic viscoelasticity and ordering of the collagen fibers in rabbit Achilles tendon. J Orthop Res. 2013;31(11):1708–12.
99. Matsumoto F, Trudel G, Uhthoff HK, Backman DS. Mechanical effects of immobilization on the Achilles' tendon. Arch Phys Med Rehabil. 2003;84(5):662–7.
100. Heinemeier KM, Skovgaard D, Bayer ML, Qvortrup K, Kjaer A, Kjaer M, Magnusson SP, Kongsgaard M. Uphill running improves rat Achilles tendon tissue mechanical properties and alters gene expression without inducing pathological changes. J Appl Physiol. 2012;113(5):827–36.
101. Glazebrook MA, Wright JR, Langman M, Stanish WD, Lee JM. Histological analysis of Achilles tendons in an overuse rat model. J Orthop Res. 2008;26(6):840–6.
102. Ng GYF, Chung PYM, Wang JS, Cheung RTH. Enforced bipedal downhill running induces Achilles tendinosis in rats. Connect Tissue Res. 2011;52(6):466–71.
103. Turunen MJ, Khayyeri H, Guizar-Sicairos M, Isaksson H. Effects of tissue fixation and dehydration on tendon collagen nanostructure. J Struct Biol. 2017 Sep;199(3):209–15.
104. Keane TJ, Horejs CM, Stevens MM. Scarring vs. functional healing: Matrix-based strategies to regulate tissue repair. Adv Drug Deliv Rev. 2018;129:407–19.
105. Sasaki K, Yamamoto N, Kiyosawa T, Sekido M. The role of collagen arrangement change during tendon healing demonstrated by scanning electron microscopy. J Electron Microsc (Tokyo). 2012;61(5):327–34.
106. Oshima J, Sasaki K, Yamamoto N, Kiyosawa T, Sekido M. Visualization of microstructural change affected by mechanical stimulation in tendon healing with a novel tensionless model. Microscopy. 2021;70(2):186–91.
107. da Silva FS, Abreu BJ, Eriksson BI, Ackermann PW. Complete mid-portion rupture of the rat achilles tendon leads to remote and time-mismatched changes in uninjured regions. Knee Surgery, Sport Traumatol Arthrosc. 2021;29(6):1990–9.
108. Hsieh CF, Alberton P, Loffredo-Verde E, Volkmer E, Pietschmann M, Müller P, Schieker M, Docheva D. Scaffold-free Scleraxis-programmed tendon progenitors aid in significantly enhanced repair of full-size Achilles tendon rupture. Nanomedicine. 2016;11(9):1153–67.

109. Voleti PB, Buckley MR, Soslowsky LJ. Tendon healing: Repair and regeneration. Annu Rev Biomed Eng. 2012;14:47–71.
110. Best KT, Loiselle AE. Scleraxis lineage cells contribute to organized bridging tissue during tendon healing and identify a subpopulation of resident tendon cells. FASEB J. 2019;33(7):8578–87.
111. Ackerman JE, Best KT, Muscat SN, Pritchett EM, Nichols AEC, Wu CL, Loiselle AE. Defining the spatial-molecular map of fibrotic tendon healing and the drivers of Scleraxis-lineage cell fate and function. Cell Rep. 2022 Nov 22;41(8).
112. Parsons BO, Gruson KI, Chen DD, Harrison AK, Gladstone J, Flatow EL. Does slower rehabilitation after arthroscopic rotator cuff repair lead to long-term stiffness? J Shoulder Elb Surg. 2010;19(7):1034–9.
113. De Aguiar G, Chait LA, Schultz D, Bleloch S, Theron A, Snijman CN, Ching V. Chemoprotection of flexor tendon repairs using botulinum toxin. Plast Reconstr Surg. 2009;124(1):201–9.
114. Strom AC, Casillas MM. Achilles Tendon Rehabilitation. Foot Ankle Clin. 2009;14(4):773–82.
115. Plessis M Du, Eksteen E, Jenneker A, Kriel E, Mentoor C, Stucky T, Van Staden D, Morris LD. The effectiveness of continuous passive motion on range of motion, pain and muscle strength following rotator cuff repair: A systematic review. Clin Rehabil. 2011;25(4):291–302.
116. Düzgün I, Baltaci G, Ahmet Atay Ö. Comparison of slow and accelerated rehabilitation protocol after arthroscopic rotator cuff repair: Pain and functional activity. Acta Orthop Traumatol Turc. 2011;45(1):23–33.
117. Schizas N, Li J, Andersson T, Fahlgren A, Aspenberg P, Ahmed M, Ackermann PW. Compression therapy promotes proliferative repair during rat achilles tendon immobilization. J Orthop Res. 2010;28(7):852–8.
118. Eliasson P, Andersson T, Aspenberg P. Rat Achilles tendon healing: Mechanical loading and gene expression. J Appl Physiol. 2009;107(2):399–407.
119. Freedman BR, Gordon JA, Bhatt PR, Pardes AM, Thomas SJ, Sarver JJ, Riggin CN, Tucker JJ, Williams AW, Zanes RC, et al. Nonsurgical treatment and early return to activity leads to improved Achilles tendon fatigue mechanics and functional outcomes during early healing in an animal model. J Orthop Res. 2016;34(12):2172–80.
120. Freedman BR, Fryhofer GW, Salka NS, Raja HA, Hillin CD, Nuss CA, Farber DC, Soslowsky LJ. Mechanical, histological, and functional

properties remain inferior in conservatively treated Achilles tendons in rodents: Long term evaluation. J Biomech. 2017;56:55–60.
121. Freedman BR, Salka NS, Morris TR, Bhatt PR, Pardes AM, Gordon JA, Nuss CA, Riggin CN, Fryhofer GW, Farber DC, et al. Temporal Healing of Achilles Tendons after Injury in Rodents Depends on Surgical Treatment and Activity. J Am Acad Orthop Surg. 2017;25(9):635–47.
122. Huber AK, Patel N, Pagani CA, Marini S, Padmanabhan KR, Matera DL, Said M, Hwang C, Hsu GCY, Poli AA, et al. Immobilization after injury alters extracellular matrix and stem cell fate. J Clin Invest. 2020;130(10):5444–60.
123. Palmes D, Spiegel HU, Schneider TO, Langer M, Stratmann U, Budny T, Probst A. Achilles tendon healing: Long-term biomechanical effects of postoperative mobilization and immobilization in a new mouse model. J Orthop Res. 2002;20(5):939–46.
124. Hsieh J. Computed tomography: Principles, Design, Artifacts and Recent Advances. SPIE Press; 2002.
125. Feldkamp L a, Davis LC, Kress J. Practical cone-beam algorithm. J Opt Soc Am. 1984;1(6):612–9.
126. Descamps E, Sochacka A, de Kegel B, Loo D Van, Hoorebeke L, Adriaens D. Soft tissue discrimination with contrast agents using micro-ct scanning. Belgian J Zool. 2014;144(1):20–40.
127. Müller R. Hierarchical microimaging of bone structure and function. Nat Rev Rheumatol. 2009;5(7):373–81.
128. Lespessailles E, Chappard C, Bonnet N, Benhamou CL. Imaging techniques for evaluating bone microarchitecture. Jt Bone Spine. 2006;73(3):254–61.
129. Neldam CA, Pinholt EM. Synchrotron μcT imaging of bone, titanium implants and bone substitutes - A systematic review of the literature. J Cranio-Maxillofacial Surg. 2014;42(6):801–5.
130. Palle J, Wittig NK, Østergaard M, Jensen AB, Birkedal H. The osteocyte lacuno-canalicular network in bone investigated by synchrotron radiation-based techniques. 2019;1111316(October 2019):39.
131. Davis TJ, Gao D, Gureyev TE, Stevenson AW, Wilkins SW. Phase-contrast imaging of weakly absorbing materials using hard X-rays. Nature. 1995;373(6515):595–8.
132. Morgan KS, Siu KKW, Paganin DM. The projection approximation and edge contrast for x-ray propagation-based phase contrast imaging of a cylindrical edge. Opt Express. 2010;18(10):9865.

133. Paganin D, Mayo SC, Gureyev TE, Miller PR, Wilkins SW. Simultaneous phase and amplitude extraction from a single defocused image of a homogeneous object. J Microsc. 2002;206(1):33–40.
134. Einarsson E, Pierantoni M, Novak V, Svensson J, Isaksson H, Englund M. Phase-contrast enhanced synchrotron micro-tomography of human meniscus tissue. Osteoarthr Cartil. 2022 Sep 1;30(9):1222–33.
135. Pierantoni M, Silva Barreto I, Hammerman M, Verhoeven L, Törnquist E, Novak V, Mokso R, Eliasson P, Isaksson H. A quality optimization approach to image Achilles tendon microstructure by phase-contrast enhanced synchrotron micro-tomography. Sci Rep. 2021;11(1):17313.
136. Pierantoni M, Hammerman M, Silva Barreto I, Andersson L, Novak V, Isaksson H, Eliasson P. Heterotopic mineral deposits in intact rat Achilles tendons are characterized by a unique fiber-like structure. J Struct Biol X. 2023;7(February):100087.
137. Fratzl P, Fratzl-Zelman N, Klaushofer K, Vogl G, Koller K. Nucleation and growth of mineral crystals in bone studied by small-angle X-ray scattering. Calcif Tissue Int. 1991;48(6):407–13.
138. Fratzl P, Groschner M, Vogl G, Plenk H, Eschberger J, Fratzl-Zelman N, Koller K, Klaushofer K. Mineral crystals in calcified tissues: A comparative study by SAXS. J Bone Miner Res. 1992;7(3):329–34.
139. Bünger MH, Oxlund H, Hansen TK, Sørensen S, Bibby BM, Jesper •, Thomsen S, Bente •, Langdahl L, Besenbacher F, et al. Strontium and Bone Nanostructure in Normal and Ovariectomized Rats Investigated by Scanning Small-Angle X-Ray Scattering. Calcif Tissue Int. 2010;86:294–306.
140. Døvling Kaspersen J, Turunen MJ, Mathavan N, Lages S, Jan •, Pedersen S, Olsson U, Isaksson H. Small-Angle X-ray Scattering Demonstrates Similar Nanostructure in Cortical Bone from Young Adult Animals of Different Species. Calcif Tissue Int. 2016;99:76–87.
141. Turunen MJ, Kaspersen JD, Olsson U, Guizar-Sicairos M, Bech M, Schaff F, Tägil M, Jurvelin JS, Isaksson H. Bone mineral crystal size and organization vary across mature rat bone cortex. J Struct Biol. 2016;195:337–44.
142. Bünger MH, Oxlund H, Hansen TK, Sørensen S, Bibby BM, Thomsen JS, Langdahl BL, Besenbacher F, Pedersen JS, Birkedal H. Strontium and bone nanostructure in normal and ovariectomized rats investigated by scanning small-angle X-ray scattering. Calcif Tissue Int. 2010;86(4):294–306.

143. Londoño-Restrepo SM, Jeronimo-Cruz R, Millán-Malo BM, Rivera-Muñoz EM, Rodriguez-García ME. Effect of the Nano Crystal Size on the X-ray Diffraction Patterns of Biogenic Hydroxyapatite from Human, Bovine, and Porcine Bones. Sci Rep. 2019;9(1):1–12.
144. Reznikov N, Bilton M, Lari L, Stevens MM, Kröger R. Fractal-like hierarchical organization of bone begins at the nanoscale. Science (80-). 2018;360(6388).
145. Törnquist E, Isaksson H, Turunen MJ. Mineralization of cortical bone during maturation and growth in rabbits. J Bone Miner Metab. 2019;
146. Turunen MJ, Lages S, Labrador A, Olsson U, Tägil M, Jurvelin JS, Isaksson H. Evaluation of composition and mineral structure of callus tissue in rat femoral fracture. J Biomed Opt. 2014;
147. Dejea H, Raina DB, Silva Barreto I, Sharma K, Liu Y, Ferreira Sanchez D, Johansson U, Isaksson H. Multi-scale characterization of the spatio-temporal interplay between elemental composition, mineral deposition and remodelling in bone fracture healing. Acta Biomater. 2023;167:135–46.
148. Le Cann S, Törnquist E, Silva Barreto I, Fraulob M, Albini Lomami H, Verezhak M, Guizar-Sicairos M, Isaksson H, Haïat G. Spatio-temporal evolution of hydroxyapatite crystal thickness at the bone-implant interface. Acta Biomater. 2020;116:391–9.
149. Mathavan N, Turunen MJ, Guizar-Sicairos M, Bech M, Schaff F, Tägil M, Isaksson H. The compositional and nano-structural basis of fracture healing in healthy and osteoporotic bone. Sci Rep. 2018;8(1):1–12.
150. Gupta HS. Chapter 7: Nanoscale Deformation Mechanisms in Collagen. In: Fratzl P, editor. Collagen: Structure and Mechanics, an introduction. Boston: Springer US; 2008.
151. Gupta HS, Seto J, Krauss S, Boesecke P, Screen HRC. In situ multi-level analysis of viscoelastic deformation mechanisms in tendon collagen. J Struct Biol. 2010;169(2):183–91.
152. Bianchi F, Hofmann F, Smith AJ, Thompson MS. Probing multi-scale mechanical damage in connective tissues using X-ray diffraction. Acta Biomater. 2016 Nov 1;45:321–7.
153. Gautieri A, Passini FS, Silván U, Guizar-Sicairos M, Carimati G, Volpi P, Moretti M, Schoenhuber H, Redaelli A, Berli M, et al. Advanced glycation end-products: Mechanics of aged collagen from molecule to tissue. Matrix Biol. 2017;59:95–108.
154. Fessel G, Li Y, Diederich V, Guizar-Sicairos M, Schneider P, Sell DR,

Monnier VM, Snedeker JG. Advanced glycation end-products reduce collagen molecular sliding to affect collagen fibril damage mechanisms but not stiffness. PLoS One. 2014;9(11).

155. Knörzer E, Folkhard W, Geercken W, Boschert C, Koch MHJ, Hilbert B, Krahl H, Mosler E, Nemetschek-Gansler H, Nemetschek T. New aspects of the etiology of tendon rupture - An analysis of time-resolved dynamic-mechanical measurements using synchrotron radiation. Arch Orthop Trauma Surg. 1986;105(2):113–20.
156. Puxkandl R, Zizak I, Paris O, Keckes J, Tesch W, Bernstorff S, Purslow P, Fratzl P. Viscoelastic properties of collagen: Synchrotron radiation investigations and structural model. Philos Trans R Soc B Biol Sci. 2002;357(1418):191–7.
157. Misof K, Rapp G, Fratzl P. A new molecular model for collagen elasticity based on synchrotron x- ray scattering evidence. Biophys J. 1997;72(3):1376–81.
158. Fratzl P, Misof K, Zizak I, Rapp G, Amenitsch H, Bernstorff S. Fibrillar Structure and Mechanical Properties of Collagen. J Struct Biol. 1997;122:119–22.
159. Bigi A, Fichera AM, Roveri N, Koch MHJ. Structural modifications of air-dried tendon collagen on heating. Int J Biol Macromol. 1987;9(3):176–80.
160. Masic A, Bertinetti L, Schuetz R, Chang SW, Metzger TH, Buehler MJ, Fratzl P. Osmotic pressure induced tensile forces in tendon collagen. Nat Commun. 2015 Jan 22;6.
161. Wess TJ, Orgel JP. Changes in collagen structure: Drying, dehydrothermal treatment and relation to long term deterioration. Thermochim Acta. 2000;365(1–2):119–28.
162. Liebi marianne, Georgiadis M, Menzel A, Schneider P, Kohlbrecher J, Bunk O, Guizar-Sicairos M. Nanostructure surveys of macroscopic specimens by small-angle scattering tensor tomography. Nature. 2015 Nov 19;527(7578):349–52.
163. Malecki A, Potdevin G, Biernath T, Eggl E, Willer K, Lasser T, Maisenbacher J, Gibmeier J, Wanner A, Pfeiffer F. X-ray tensor tomography. Epl. 2014;105(3).
164. Georgiadis M, Guizar-Sicairos M, Zwahlen A, Trüssel AJ, Bunk O, Müller R, Schneider P. 3D scanning SAXS: A novel method for the assessment of bone ultrastructure orientation. Bone. 2015;71:42–52.
165. Gao Z, Guizar-Sicairos M, Lutz-Bueno V, Schröter A, Liebi M, Rudin M,

Georgiadis M. High-speed tensor tomography: Iterative reconstruction tensor tomography (IRTT) algorithm. Acta Crystallogr Sect A Found Adv. 2019;75:223–38.

166. Schaff F, Bech M, Zaslansky P, Jud C, Liebi M, Guizar-Sicairos M, Pfeiffer F. Six-dimensional real and reciprocal space small-angle X-ray scattering tomography. Nature. 2015;527:353–8.
167. Nielsen LC, Erhart P, Guizar-Sicairos M, Liebi M. Small-angle scattering tensor tomography algorithm for robust reconstruction of complex textures. 2023; Available from: http://arxiv.org/abs/2305.07750
168. Grünewald TA, Liebi M, Wittig NK, Johannes A, Sikjaer T, Rejnmark L, Gao Z, Rosenthal M, Guizar-Sicairos M, Birkedal H, et al. Mapping the 3D orientation of nanocrystals and nanostructures in human bone: Indications of novel structural features. Sci Adv. 2020;6(24):4171–83.
169. Liebi M, Lutz-Bueno V, Guizar-Sicairos M, Schönbauer BM, Eichler J, Martinelli E, Löffler JF, Weinberg A, Lichtenegger H, Grünewald TA. 3D nanoscale analysis of bone healing around degrading Mg implants evaluated by X-ray scattering tensor tomography. Acta Biomater. 2021;
170. Casanova EA, Rodriguez-Palomo A, Stähli L, Arnke K, Gröninger O, Generali M, Neldner Y, Tiziani S, Dominguez AP, Guizar-Sicairos M, et al. SAXS imaging reveals optimized osseointegration properties of bioengineered oriented 3D-PLGA/aCaP scaffolds in a critical size bone defect model. Biomaterials. 2023;294(April 2022).
171. Grünewald TA, Johannes A, Wittig NK, Palle J, Rack A, Burghammer M, Birkedal H. Bone mineral properties and 3D orientation of human lamellar bone around cement lines and the Haversian system. IUCrJ. 2023;10(2):189–98.
172. Rajasekharan AK, Lotsari A, Lutz-Bueno V, Liebi M, Andersson M. Bioinspired Structural Hierarchy within Macroscopic Volumes of Synthetic Composites. Adv Healthc Mater. 2018;7(18):1–7.
173. Georgiadis M, Schroeter A, Gao Z, Guizar-Sicairos M, Liebi M, Leuze C, McNab JA, Balolia A, Veraart J, Ades-Aron B, et al. Nanostructure-specific X-ray tomography reveals myelin levels, integrity and axon orientations in mouse and human nervous tissue. Nat Commun. 2021;12(1):1–13.
174. EDWARDS RA. Fundamentals of Atomic and Radiation Physics. In: Physics for ONC Courses. 1970. p. 507–28.
175. Percival M. Bone health & osteoporosis. Appl Nutr Sci Reports. 1999;5(4):1–6.
176. Maciejewska K, Drzazga Z, Kaszuba M. Role of trace elements (Zn, Sr, Fe)

in bone development: Energy dispersive X-ray fluorescence study of rat bone and tooth tissue. BioFactors. 2014;40:425–35.
177. Bradley DA, Moger CJ, Winlove CP. Zn deposition at the bone-cartilage interface in equine articular cartilage. Nucl Instruments Methods Phys Res Sect A Accel Spectrometers, Detect Assoc Equip. 2007;580(1 SPEC. ISS.):473–6.
178. Kaabar W, Gundogdu O, Laklouk A, Bunk O, Pfeiffer F, Farquharson MJ, Bradley DA. μ-PIXE and SAXS studies at the bone-cartilage interface. Appl Radiat Isot. 2010;68(4–5):730–4.
179. Brister E, Vasi Z, Antipova O, Robinson A, Tan X, Agarwal A, Stock SR, Carriero A, Richter C-P. X-ray fluorescence microscopy: A method of measuring ion concentrations in the ear. Hear Res. 2020 Mar;107948.
180. Stuart B. Infrared Spectroscopy: Fundamentals and Applications Analytical Techniques in the Sciences. Chichester; England: John Wiley & Sons Ltd.; 2004. 242 p.
181. Boskey A, Camacho NP. FT-IR imaging of native and tissue-engineered bone and cartilage. Biomaterials. 2007;28:2465–78.
182. Turunen MJ, Prantner V, Jurvelin JS, Kröger H, Isaksson H. Composition and microarchitecture of human trabecular bone change with age and differ between anatomical locations. Bone. 2013;54(1):118–25.
183. Kobrina Y, Isaksson H, Sinisaari M, Rieppo L, Brama PA, van Weeren R, Helminen HJ, Jurvelin JS, Saarakkala S. Infrared spectroscopy reveals both qualitative and quantitative differences in equine subchondral bone during maturation. J Biomed Opt. 2010;15(6):067003.
184. Turunen MJ, Saarakkala S, Helminen HJ, Jurvelin JS, Isaksson H. Age-related changes in organization and content of the collagen matrix in rabbit cortical bone. J Orthop Res. 2012;30(3):435–42.
185. Henmi A, Okata H, Anada T, Yoshinari M, Mikami Y, Suzuki O, Sasano Y. Bone matrix calcification during embryonic and postembryonic rat calvarial development assessed by SEM–EDX spectroscopy, XRD, and FTIR spectroscopy. J Bone Miner Metab. 2016;34:41–50.
186. Goldstein DH. Polarized Light. 3rd editio. CRC Press; 2011.
187. Collett E. Field Guide to Polarization. SPIE Press; 2005.
188. Bromage TG, Goldman HM, McFarlin SC, Warshaw J, Boyde A, Riggs CM. Circularly polarized light standards for investigations of collagen fiber orientation in bone. Anat Rec - Part B New Anat. 2003 Sep 1;274(1):157–68.
189. Holopainen JT, Brama PAJ, Halmesmäki E, Harjula T, Tuukkanen J, van

Weeren PR, Helminen HJ, Hyttinen MM. Changes in subchondral bone mineral density and collagen matrix organization in growing horses. Bone. 2008;43(6):1108–14.
190. Ramasamy JG, Akkus O. Local variations in the micromechanical properties of mouse femur: The involvement of collagen fiber orientation and mineralization. J Biomech. 2007;40(4):910–8.
191. Kalmey JK, Lovejoy CO. Collagen fiber orientation in the femoral necks of apes and humans: do their histological structures reflect differences in locomotor loading? Bone. 2002;31(2):327–32.
192. Korhonen K. R, Saarakkal S. Theoretical Biomechanics. In IntechOpen; 2011.
193. Turner CH, Burr DB. Basic biomechanical measurements of bone: A tutorial. Bone. 1993;14(4):595–608.
194. Sharir A, Barak MM, Shahar R. Whole bone mechanics and mechanical testing. Vet J. 2008;177(1):8–17.
195. Gustafsson A, Mathavan N, Turunen MJ, Engqvist J, Khayyeri H, Hall SA, Isaksson H. Linking multiscale deformation to microstructure in cortical bone using in situ loading, digital image correlation and synchrotron X-ray scattering. Acta Biomater. 2018 Mar;69:323–31.
196. Screen HRC, Seto J, Krauss S, Boesecke P, Gupta HS. Extrafibrillar diffusion and intrafibrillar swelling at the nanoscale are associated with stress relaxation in the soft collagenous matrix tissue of tendons. Soft Matter. 2011;7(23):11243–51.
197. Folkhard W, Mosler E, Geercken W, Knörzer E, Nemetschek-Gansler H, Nemetschek T, Koch MHJ. Quantitative analysis of the molecular sliding mechanisms in native tendon collagen - time-resolved dynamic studies using synchrotron radiation. Int J Biol Macromol. 1987;9(3):169–75.
198. Mosler E, Folkhard W, Knörzer E, Nemetschek-Gansler H, Nemetschek T, Koch MHJ. Stress-induced molecular rearrangement in tendon collagen. J Mol Biol. 1985 Apr 20;182(4):589–96.
199. Szczesny SE, Caplan JL, Pedersen P, Elliott DM. Quantification of interfibrillar shear stress in aligned soft collagenous tissues via notch tension testing. Sci Rep. 2015;5:14649.
200. Lee AH, Szczesny SE, Santare MH, Elliott DM. Investigating mechanisms of tendon damage by measuring multi-scale recovery following tensile loading. Acta Biomater. 2017;57:363–72.
201. Thorpe CT, Birch HL, Clegg PD, Screen HRC. Tendon Physiology and Mechanical Behavior: Structure-Function Relationships. Tendon

Regeneration: Understanding Tissue Physiology and Development to Engineer Functional Substitutes. Elsevier Inc.; 2015. 3–39 p.
202. Cheng VWT, Screen HRC. The micro-structural strain response of tendon. J Mater Sci. 2007;42(21):8957–65.
203. Szczesny SE, Elliott DM. Interfibrillar shear stress is the loading mechanism of collagen fibrils in tendon. Acta Biomater. 2014;10(6):2582–90.
204. Thorpe CT, Udeze CP, Birch HL, Clegg PD, Screen HRC. Specialization of tendon mechanical properties results from interfascicular differences. J R Soc Interface. 2012;9(76):3108–17.
205. Thorpe CT, Godinho MSC, Riley GP, Birch HL, Clegg PD, Screen HRC. The interfascicular matrix enables fascicle sliding and recovery in tendon, and behaves more elastically in energy storing tendons. J Mech Behav Biomed Mater. 2015;52:85–94.
206. Lee AH, Szczesny SE, Santare MH, Elliott DM. Investigating mechanisms of tendon damage by measuring multi-scale recovery following tensile loading. Acta Biomater. 2017;57:363–72.
207. Fang F, Lake SP. Experimental evaluation of multiscale tendon mechanics. Vol. 35, Journal of Orthopaedic Research. 2017. p. 1353–65.
208. Theiler K. The House Mouse: Atlas of Embryonic Development. 2nd ed. New York: Springer-Verlag; 1989.
209. Titarenko V. Analytical formula for two-dimensional ring artefact suppression. J Synchrotron Radiat. 2016;23(6):1447–61.
210. Bunk O, Bech M, Jensen TH, Feidenhans'L R, Binderup T, Menzel A, Pfeiffer F. Multimodal x-ray scatter imaging. New J Phys. 2009;11:1–8.
211. Kraft P, Bergamaschi A, Broennimann C, Dinapoli R, Eikenberry EF, Henrich B, Johnson I, Mozzanica A, Schlepütz CM, Willmott PR, et al. Performance of single-photon-counting PILATUS detector modules. J Synchrotron Radiat. 2009;16(3):368–75.
212. Liebi M, Georgiadis M, Kohlbrecher J, Holler M, Raabe J, Usov I, Menzel A, Schneider P, Bunk O, Guizar-Sicairos M. Small-angle X-ray scattering tensor tomography: Model of the three-dimensional reciprocal-space map, reconstruction algorithm and angular sampling requirements. Acta Crystallogr Sect A Found Adv. 2018;
213. Guizar-Sicairos M, Georgiadis M, Liebi M. Validation study of small-angle X-ray scattering tensor tomography. J Synchrotron Radiat. 2020;27:779–87.
214. Solé VA, Papillon E, Cotte M, Walter P, Susini J. A multiplatform code

for the analysis of energy-dispersive X-ray fluorescence spectra. Spectrochim Acta - Part B At Spectrosc. 2007;62:63–8.
215. Isaksson H, Turunen MJ, Rieppo L, Saarakkala S, Tamminen IS, Rieppo J, Kröger H, Jurvelin JS. Infrared spectroscopy indicates altered bone turnover and remodeling activity in renal osteodystrophy. J Bone Miner Res. 2010;25(6):1360–6.
216. Turunen MJ, Saarakkala S, Rieppo L, Helminen HJ, Jurvelin JS, Isaksson H. Comparison between infrared and raman spectroscopic analysis of maturing rabbit cortical bone. Appl Spectrosc. 2011;65:595–603.
217. Han CY, Chao YF. Photoelastic modulated imaging ellipsometry by stroboscopic illumination technique. Rev Sci Instrum. 2006;77(2).
218. Nichols S, Freudenthal J, Arteaga O, Kahr B. Imaging with photoelastic modulators. Polariz Meas Anal Remote Sens XI. 2014;9099(May 2014):909912.
219. Engqvist J, Hall SA, Wallin M, Ristinmaa M, Plivelic TS. Multi-scale Measurement of (Amorphous) Polymer Deformation: Simultaneous X-ray Scattering, Digital Image Correlation and In-situ Loading. Exp Mech. 2014;
220. Sasaki N, Odajima S. Elongation mechanism of collagen fibrils and force-strain relations of tendon at each level of structural hierarchy. J Biomech. 1996;29(9):1131–6.
221. Inamdar SR, Knight DP, Terrill NJ, Karunaratne A, Cacho-Nerin F, Knight MM, Gupta HS. The Secret Life of Collagen: Temporal Changes in Nanoscale Fibrillar Pre-Strain and Molecular Organization during Physiological Loading of Cartilage. ACS Nano. 2017;11(10):9728–37.
222. Marone F, Stampanoni M. Synchrotron Radiation Regridding reconstruction algorithm for real-time tomographic imaging. 2012;19:1029–37.
223. Otsu N. A Threshold Selection Method from Gray-Level Histograms. IEEE Trans Syst Man Cybern. 1979 Jan;9(1):62–6.
224. Krause M, Hausherr JM, Burgeth B, Herrmann C, Krenkel W. Determination of the fibre orientation in composites using the structure tensor and local X-ray transform. J Mater Sci. 2010;45(4):888–96.
225. Jeppesen N, Dahl VA, Christensen AN, Dahl AB, Mikkelsen LP, Andersen V, Himmelstrup C, Bjorholm A, Saxena P, Bissacco G, et al. Process characterization for molding of paper bottles using computed tomography and structure tensor analysis. E-Journal Nondestruct Test Ultrason. 2020;942(1):24.

226. Beattie JH, Avenell A. Trace Element Nutrition and Bone Metabolism. Nutr Res Rev. 1992;5(1):167–88.
227. Genge BR, Sauer GR, Wu LNY, McLean FM, Wuthier RE. Correlation between loss of alkaline phosphatase activity and accumulation of calcium during matrix vesicle-mediated mineralization. J Biol Chem. 1988;263(34):18513–9.
228. Litchfield TM, Ishikawa Y, Wu LNY, Wuthier RE, Sauer GR. Effect of metal ions on calcifying growth plate cartilage chondrocytes. Calcif Tissue Int. 1998;62(4):341–9.
229. Ortega N, Behonick DJ, Werb Z. Matrix remodeling during endochondral ossification. Trends Cell Biol. 2004;14(2):86–93.
230. Bord S, Horner A, Beeton CA, Hembry RM, Compston JE. Tissue inhibitor of matrix metalloproteinase-1 (TIMP-1) distribution in normal and pathological human bone. Bone. 1999;24(3):229–35.
231. Johansson N, Saarialho-Kere U, Airola K, Herva R, Nissinen L, Westermarck J, Vuorio E, Heino J, Kähäri VM. Collagenase-3 (MMP-13) is expressed by hypertrophic chondrocytes, periosteal cells, and osteoblasts during human fetal bone development. Dev Dyn. 1997;208(3):387–97.
232. Procopio A, Malucelli E, Pacureanu A, Cappadone C, Farruggia G, Sargenti A, Castiglioni S, Altamura D, Sorrentino A, Giannini C, et al. Chemical Fingerprint of Zn–Hydroxyapatite in the Early Stages of Osteogenic Differentiation. ACS Cent Sci. 2019;
233. Friederichs RJ, Chappell HF, Shepherd D V., Best SM. Synthesis, characterization and modelling of zinc and silicate co-substituted hydroxyapatite. J R Soc Interface. 2015;12(108).
234. Stern T, Aviram R, Rot C, Galili T, Sharir A, Achrai NK, Keller Y, Shahar R, Zelzer E. Isometric scaling in developing long bones is achieved by an optimal epiphyseal growth balance. PLoS Biol. 2015;13(8):1–28.
235. Eyal S, Kult S, Rubin S, Krief S, Felsenthal N, Pineault KM, Leshkowitz D, Salame TM, Addadi Y, Wellik DM, et al. Bone morphology is regulated modularly by global and regional genetic programs. Dev. 2019;146(14):1–15.
236. Nowlan NC, Dumas G, Tajbakhsh S, Prendergast PJ, Murphy P. Biophysical stimuli induced by passive movements compensate for lack of skeletal muscle during embryonic skeletogenesis. Biomech Model Mechanobiol. 2012;
237. Fang F, Lake SP. Multiscale strain analysis of tendon subjected to shear and compression demonstrates strain attenuation, fiber sliding, and

reorganization. J Orthop Res. 2015 Nov 1;33(11):1704–12.
238. Thorpe CT, Riley GP, Birch HL, Clegg PD, Screen HRC. Fascicles from energy-storing tendons show an age-specific response to cyclic fatigue loading. J R Soc Interface. 2014;11(92).
239. Svensson RB, Mulder H, Kovanen V, Magnusson SP. Fracture mechanics of collagen fibrils: Influence of natural cross-links. Biophys J. 2013;104(11):2476–84.
240. Svensson RB, Smith ST, Moyer PJ, Magnusson SP. Effects of maturation and advanced glycation on tensile mechanics of collagen fibrils from rat tail and Achilles tendons. Acta Biomater. 2018;70:270–80.
241. Svensson RB, Eriksen CS, Tran PHT, Kjaer M, Magnusson SP. Mechanical properties of human patellar tendon collagen fibrils. An exploratory study of aging and sex. J Mech Behav Biomed Mater. 2021;124(April):104864.
242. Quigley AS, Bancelin S, Deska-Gauthier D, Légaré F, Kreplak L, Veres SP. In tendons, differing physiological requirements lead to functionally distinct nanostructures. Sci Rep. 2018;8(1).
243. Roeder BA, Kokini K, Voytik-Harbin SL. Fibril microstructure affects strain transmission within collagen extracellular matrices. J Biomech Eng. 2009;131(3):1–11.
244. Thorpe CT, Streeter I, Pinchbeck GL, Goodship AE, Clegg PD, Birch HL. Aspartic acid racemization and collagen degradation markers reveal an accumulation of damage in tendon collagen that is enhanced with aging. J Biol Chem. 2010;285(21):15674–81.
245. Amiel D, Woo SLY, Harwood FL, Akeson WH. the effect of immobilization on collagen turnover in connective tissue: A biochemical-biomechanical correlation. Acta Orthop. 1982;53(3):325–32.
246. Dyment NA, Liu CF, Kazemi N, Aschbacher-Smith LE, Kenter K, Breidenbach AP, Shearn JT, Wylie C, Rowe DW, Butler DL. The Paratenon Contributes to Scleraxis-Expressing Cells during Patellar Tendon Healing. PLoS One. 2013;8(3).
247. Morita Y, Watanabe S, Ju Y, Xu B. Determination of optimal cyclic Uniaxial stretches for stem cell-to-tenocyte differentiation under a wide range of mechanical stretch conditions by evaluating gene expression and protein synthesis levels. Acta Bioeng Biomech. 2013;15(3):71–9.
248. Sun L, Qu L, Zhu R, Li H, Xue Y, Liu X, Fan J, Fan H. Effects of Mechanical Stretch on Cell Proliferation and Matrix Formation of Mesenchymal Stem Cell and Anterior Cruciate Ligament Fibroblast. Stem

Cells Int. 2016;2016.
249. Manuyakorn W, Smart DE, Noto A, Bucchieri F, Haitchi HM, Holgate ST, Howarth PH, Davies DE. Mechanical strain causes adaptive change in bronchial fibroblasts enhancing profibrotic and inflammatory responses. PLoS One. 2016;11(4):1–16.
250. Liu J, Yu W, Liu Y, Chen S, Huang Y, Li X, Liu C, Zhang Y, Li Z, Du J, et al. Mechanical stretching stimulates collagen synthesis via down-regulating so 2/AAT1 pathway. Sci Rep. 2016;6(September 2015):1–9.
251. Freedman BR, Rodriguez AB, Hillin CD, Weiss SN, Han B, Han L, Soslowsky LJ. Tendon healing affects the multiscale mechanical, structural and compositional response of tendon to quasi-static tensile loading. J R Soc Interface. 2018;15(139).
252. Barth HD, Launey ME, MacDowell AA, Ager JW, Ritchie RO. On the effect of X-ray irradiation on the deformation and fracture behavior of human cortical bone. Bone. 2010;46(6):1475–85.
253. Hackett MJ, McQuillan JA, El-Assaad F, Aitken JB, Levina A, Cohen DD, Siegele R, Carter EA, Grau GE, Hunt NH, et al. Chemical alterations to murine brain tissue induced by formalin fixation: Implications for biospectroscopic imaging and mapping studies of disease pathogenesis. Analyst. 2011;136(14):2941–52.
254. Song H, Polk JD, Kersh ME. Rat bone properties and their relationship to gait during growth. J Exp Biol. 2019;222(18).
255. Manske SL, Boyd SK, Zernicke RF. Vertical ground reaction forces diminish in mice after botulinum toxin injection. J Biomech. 2011;44(4):637–43.
256. Chen K, Hu X, Blemker SS, Holmes JW. Multiscale computational model of Achilles tendon wound healing: Untangling the effects of repair and loading. PLoS Comput Biol. 2018;14(12):1–20.
257. Johnson WL, Jindrich DL, Roy RR, Reggie Edgerton V. A three-dimensional model of the rat hindlimb: Musculoskeletal geometry and muscle moment arms. J Biomech. 2008;41(3):610–9.
258. Kharazi M, Bohm S, Theodorakis C, Mersmann F, Arampatzis A. Quantifying mechanical loading and elastic strain energy of the human Achilles tendon during walking and running. Sci Rep. 2021;11(1):1–13.
259. Baxter JR, Corrigan P, Hullfish TJ, O'Rourke P, Silbernagel KG. Exercise Progression to Incrementally Load the Achilles Tendon. Med Sci Sports Exerc. 2021;53(1):124–30.
260. Huang J, Wang C, Ma X, Wang X, Zhang C, Chen L. Rehabilitation

regimen after surgical treatment of acute Achilles tendon ruptures: A systematic review with meta-analysis. Am J Sports Med. 2015;43(4):1008–16.
261. Sandberg OH. Influence of a lower leg brace on traction force in. 2015;63–7.
262. Freedman BR, Gordon JA, Soslowsky LJ. The Achilles tendon: Fundamental properties and mechanisms governing healing. Muscles Ligaments Tendons J. 2014;4(2):245–55.
263. Galloway MT, Lalley AL, Shearn JT. The role of mechanical loading in tendon development, maintenance, injury, and repair. J Bone Jt Surg. 2013;95(17):1620–8.
264. Schepull T, Aspenberg P. Healing of human Achilles tendon ruptures: radiodensity reflects mechanical properties. Knee Surgery, Sport Traumatol Arthrosc. 2015;23(3):884–9.
265. El-Akkawi AI, Joanroy R, Barfod KW, Kallemose T, Kristensen SS, Viberg B. Effect of Early Versus Late Weightbearing in Conservatively Treated Acute Achilles Tendon Rupture: A Meta-Analysis. Vol. 57, Journal of Foot and Ankle Surgery. 2018. p. 346–52.
266. Wittig NK, Palle J, Østergaard M, Frølich S, Birkbak ME, Spiers KM, Garrevoet J, Birkedal H. Bone Biomineral Properties Vary across Human Osteonal Bone Article. ACS Nano. 2019;13:12949–56.
267. Palle J, Wittig NK, Kubec A, Niese S, Rosenthal M, Burghammer M, Grünewald TA, Birkedal H. Nanobeam X-ray fluorescence and diffraction computed tomography on human bone with a resolution better than 120 nm. J Struct Biol. 2020;212(3).
268. Szczesny SE, Fetchko KL, Dodge GR, Elliott DM. Evidence that interfibrillar load transfer in tendon is supported by small diameter fibrils and not extrafibrillar tissue components. J Orthop Res. 2017;35(10):2127–34.
269. Arndt A, Bengtsson AS, Peolsson M, Thorstensson A, Movin T. Non-uniform displacement within the Achilles tendon during passive ankle joint motion. Knee Surgery, Sport Traumatol Arthrosc. 2012;20(9):1868–74.
270. M. Khair R, Stenroth L, Péter A, Cronin NJ, Reito A, Paloneva J, Finni T. Non-uniform displacement within ruptured Achilles tendon during isometric contraction. Scand J Med Sci Sport. 2021;31(5):1069–77.
271. Raimondi P. ESRF-EBS: The Extremely Brilliant Source Project. Synchrotron Radiat News. 2016;29(6):8–15.
272. Tavares PF, Al-Dmour E, Andersson Å, Cullinan F, Jensen BN, Olsson D,

Olsson DK, Sjöström M, Tarawneh H, Thorin S, et al. Commissioning and first-year operational results of the MAX IV 3 GeV ring. J Synchrotron Radiat. 2018;25(5):1291–316.

273. Streun A, Garvey T, Rivkin L, Schlott V, Schmidt T, Willmott P, Wrulich A. SLS-2 – the upgrade of the Swiss Light Source. J Synchrotron Radiat. 2018;25(3):631–41.
274. Hammerman M, Aspenberg P, Eliasson P. Microtrauma stimulates rat Achilles tendon healing via an early gene expression pattern similar to mechanical loading. J Appl Physiol. 2014;116(1):54–60.
275. Pierantoni M, Hammerman M, Silva Barreto I, Larsson D, Notermans T, Bodey AJ, Eliasson P, Isaksson H. Spatiotemporal and microstructural characterization of heterotopic ossification in healing rat Achilles tendons. FASEB J. 2023;37(6):1–11.
276. Mathavan N, Koopman J, Raina DB, Turkiewicz A, Tägil M, Isaksson H. 18F-fluoride as a prognostic indicator of bone regeneration. Acta Biomater. 2019;90:403–11.
277. Mathavan N, Raina DB, Tägil M, Isaksson H. Longitudinal in vivo monitoring of callus remodeling in BMP-7- and Zoledronate-treated fractures. J Orthop Res. 2020;38(9):1905–13.
278. Mehta M, Checa S, Lienau J, Hutmacher D, Duda GN. In vivo tracking of segmental bone defect healing reveals that callus patterning is related to early mechanical stimuli. Eur Cells Mater. 2012;24(0):358–71.
279. Birkhold AI, Razi H, Duda GN, Weinkamer R, Checa S, Willie BM. The influence of age on adaptive bone formation and bone resorption. Biomaterials. 2014;35(34):9290–301.
280. Birkhold AI, Razi H, Duda GN, Weinkamer R, Checa S, Willie BM. Mineralizing surface is the main target of mechanical stimulation independent of age: 3D dynamic in vivo morphometry. Bone. 2014;66:15–25.
281. Dubsky S. Synchrotron-Based Dynamic Lung Imaging. Molecular Imaging: Principles and Practice. Brian D. Ross and Sanjiv Sam Gambhir; 2021. 359–371 p.
282. Gradl R, Dierolf M, Günther B, Hehn L, Möller W, Kutschke D, Yang L, Donnelley M, Murrie R, Erl A, et al. In vivo Dynamic Phase-Contrast X-ray Imaging using a Compact Light Source. Sci Rep. 2018;8(1):1–8.
283. Fleming BC, Beynnon BD. In vivo measurement of ligament/tendon strains and forces: A review. Ann Biomed Eng. 2004;32(3):318–28.
284. Dams OC, Reininga IHF, Gielen JL, van den Akker-Scheek I, Zwerver J.

Imaging modalities in the diagnosis and monitoring of Achilles tendon ruptures: A systematic review. Injury. 2017;48(11):2383–99.
285. Monte A, Skypala J, Vilimek D, Juras V, Jandacka D. Correlations between Achilles tendon material and structural properties and quantitative magnetic resonance imagining in different athletic populations. J Biomech. 2023;159(September):111796.
286. Adam NC, Smith CR, Herzog W, Amis AA, Arampatzis A, Taylor WR. In Vivo Strain Patterns in the Achilles Tendon During Dynamic Activities: A Comprehensive Survey of the Literature. Sport Med - Open. 2023;9(1).
287. Kosiol J, Keiler A, Loizides A, Gruber H, Henninger B, Bölderl A, Gruber L. Operative versus conservative treatment of acute Achilles tendon ruptures: preliminary results of clinical outcome, kinematic MRI and contrast-enhanced ultrasound. Arch Orthop Trauma Surg. 2023;143(5):2455–65.
288. Juras V, Zbyn S, Pressl C, Valkovic L, Szomolanyi P, Frollo I, Trattnig S. Regional variations of T2* in healthy and pathologic achilles tendon in vivo at 7 Tesla: Preliminary results. Magn Reson Med. 2012;68(5):1607–13.
289. Juras V, Apprich S, Szomolanyi P, Bieri O, Deligianni X, Trattnig S. Bi-exponential T2*analysis of healthy and diseased Achilles tendons: An in vivo preliminary magnetic resonance study and correlation with clinical score. Eur Radiol. 2013;23(10):2814–22.
290. McDonald SA, Marone F, Hintermüller C, Mikuljan G, David C, Pfeiffer F, Stampanoni M. Advanced phase-contrast imaging using a grating interferometer. J Synchrotron Radiat. 2009;16(4):562–72.
291. Wang Z, Stampanoni M. Quantitative x-ray radiography using grating interferometry: A feasibility study. Phys Med Biol. 2013;58(19):6815–26.
292. Heck L, Eggl E, Grandl S, Dierolf M, Jud C, Günther B, Achterhold K, Mayr D, Gleich B, Hellerhoff K, et al. Dose and spatial resolution analysis of grating-based phase-contrast mammography using an inverse Compton x-ray source. 2019;(September 2019):20.
293. Arboleda C, Wang Z, Jefimovs K, Koehler T, Stevendaal U Van, Kuhn N, David B, Prevrhal S, Lång K, Forte S, et al. Towards clinical grating-interferometry mammography. 2020;1419–25.

Appended papers

I. Multiscale characterization of embryonic long bone mineralization in mice. *Published*

II. Lack of embryonic skeletal muscle in mice leads to abnormal mineral deposition and growth. *Manuscript under preparation (to be submitted October 2023)*

III. Nanoscale characterization of collagen structural response to *in situ* loading in rat Achilles tendons. *Published*

IV. Multimodal and multiscale characterization reveals how tendon structure and mechanical response are altered by reduced loading. *Published*

V. Micro- and nanostructure specific X-ray tomography reveals less matrix formation and altered collagen organization following reduced loading during Achilles tendon healing. *Under review*

VI. *In situ* characterization reveals an impaired fibril response to loading following unloading during early Achilles tendon healing. *Data analysis ongoing, preliminary draft (to be submitted fall 2023)*